Spring 2000

# Pulsed Optoacoustics in Solids

Zibiao Wei
*Old Dominion University*

# PULSED OPTOACOUSTICS IN SOLIDS

by

Zibiao Wei
B.S. June 1991, Fudan University
M.S. March 1994, Tsinghua University

A Dissertation submitted to the Faculty of
Old Dominion University in Partial Fulfillment of the
Requirement for the Degree of

DOCTOR OF PHILOSOPHY

ELECTRICAL ENGINEERING

OLD DOMINION UNIVERSITY
May 2000

Approved by:

Amin Dharamsi (Director)

Ravindra Joshi (Member)

Linda Vahala (Member)

Barbara Hargrave (Member)

# ABSTRACT

## PULSED OPTOACOUSTICS IN SOLIDS

Zibiao Wei
Old Dominion University, 2000
Director: Dr. Amin N. Dharamsi

Optoacoustic techniques are widely used to probe and characterize target materials including solids, liquids and gases. Included in such applications are diagnoses of thin films and semiconductor materials. The need to obtain greater spatial resolution requires the generation of shorter optoacoustic pulses. For such pulses, non-thermal effects may be quite important. On the other hand, even when an optoacoustic pulse is generated by an initially non-thermal technique, the thermal aspects become important in its evolution and propagation. The research undertaken in this Ph.D. dissertation included the generation and detection of optoacoustic signals through the thermal elastic mechanism. Several applications in material property diagnostics were investigated using several pulsed lasers. Both contact and non-contact detection techniques were used. A compact, lightweight, inexpensive system using a semiconductor laser, with potentially wide applicability, was developed.

We developed the methods of analysis required to compare and explain the experimental results obtained. Included in such development was the incorporation of the responsivity of a piezoelectric transducer, whose necessarily non-ideal characteristics need to be accounted for in any analysis. We extended the Rosencwaig-Gersho model, which is used to treat the thermal diffusion problem with a sinusoidal heat source, to a

general pulsed laser source. This problem was also solved by a numerical method we developed in this work.

Two powerful tools were introduced to process experimental data. The Fourier transform was used to resolve the time interval between two acoustic echoes. The wavelet transform was used to identify optoacoustic pulses in different wave modes or those generated by different mechanisms. The wavelet shrinkage technique was used to remove white noise from the signal.

We also developed a spectral ratio method, which eliminates the need for the knowledge of several material parameters, to obtain the optical absorption coefficient. Finally, we extended the optoacoustic measurement to biological samples and applied techniques that we developed in this work to process and analyze signals obtained from such samples.

## ACKNOWLEDGMENTS

First of all, I am very grateful for all the advice, inspiration, and encouragement that I received from my advisor, Dr. Amin Dharamsi. I would also like to extend much appreciation to Dr. Ravindra Joshi, Dr. Linda Vahala, and Dr. Barbara Hargrave for serving on my committee.

I would like to express appreciation to Dr. Mool Gupta and Dr. Kang Seo for allowing and helping me to use their Nd:YAG laser, and to Dr. Barbara Hargrave for providing the tissue samples. Thanks are also due to Mr. Tom Galloway and the staff of the machine shop for their help with instruments and devices. Much appreciation to fellow students, especially Audra Bullock and Shujun Yang, for all their help in the lab.

Finally, I would like to thank my wife and my family for all their support and encouragement.

# TABLE OF CONTENTS

# LIST OF FIGURES

Page

Page

Page

Page

Page

# CHAPTER I

# INTRODUCTION

## 1.1. AN OVERVIEW OF OPTOACOUSTICS

### 1.1.1. Generation mechanisms of acoustic signals by light

The photoacoustic (PA) or optoacoustic (OA) effect is the phenomenon in which acoustic waves are generated when a sample is irradiated with light. A common mechanism, which leads to energy conversion from light to acoustic energy, is the thermoelastic effect. When a pulsed or modulated laser beam strikes the surface of a sample, the local temperature will rise due to the absorption of the laser energy. This temperature gradient produces, as a result of thermal expansion, a strain in the body. The surrounding medium is compressed by the reaction force from the expanded volume. The expansion-compression action generates an acoustic wave. The transient heating and thermal expansion process is so brief that the detected acoustic wave usually is ultrasonic. For small incident optical powers, this acoustic generation process is an elastic one and does not induce any phase changes in the medium. The conversion efficiency of this elastic process is rather low (typically about $10^{-4}$ for condensed matter [1, 2]), but it often provides a useful tool for non-intrusive diagnostics.

This dissertation will concentrate on the generation of ultrasound by the thermoelastic

---

Journal model used for this dissertation is *Journal of Applied Physics*.

effect. However, it has to be noted that there are other mechanisms that also lead to acoustic generation from incident laser radiation. Such mechanisms include the initially cold photostrictive process, dielectric breakdown, vaporization, ablation, electrostriction and radiation pressure.

The photostrictive mechanism for OA generation is a non-thermal effect [3]. When the sample is excited by ultrashort laser pulses, the lattice constant can change via a non-thermal photostrictive mechanism. Such non-thermal optoacoustic generation occurs in semiconductor materials irradiated by a subpicosecond laser of proper wavelength. There are three stages that occur during this generation [4], namely: the electron-hole pair dephasing, which results in a temperature rise only for carriers but not the lattice; optical phonon emission through which the carriers lose their excess energy; and acoustic phonon generation, which is an efficient way for carrier cooling after the second stage. After the carrier and lattice temperatures are equalized, the material has "heated up". The thermal elastic acoustic signal is generated after such heating. Therefore, a non-thermal optoacoustic signal is always accompanied with a thermal optoacoustic signal, but they occur at different stages after the laser irradiation. The non-thermal OA generation has many potential applications [5].

The dielectric breakdown mechanism occurs at ultra high laser intensity ($\sim 10^{10}$ $Wcm^{-2}$) [6, 7]. It can be distinguished from the thermoelastic effect in transparent media where sound generation by absorption and thermal expansion does not easily occur. The plasma due to the dielectric breakdown can produce shocks. This highly nonlinear process often has a high conversion efficiency, which can be as high as 30% in liquid [2], but requires a relatively high threshold intensity.

Both vaporization and material ablation correspond to matter phase change because of over heating by laser radiation [2, 8, 9]. Vaporization occurs on a liquid surface while ablation occurs on a solid surface. The ejection of material from the surface generates a recoil momentum in the sample and results in an acoustic signal. This mechanism also requires that the laser energy density be above a threshold, which is determined by the properties of the medium. The conversion efficiency can reach 1% [2].

Electrostriction is due to the electric polarization of molecules in the sample [10-12]. The high light intensity causes these polarized molecules to move backward or forward according to positive or negative polarization. These motions produce a density gradient which corresponds to the generation of sound in the medium. Electrostriction often occurs in transparent media when electric field intensity exceeds approximately $10^7$ $Vcm^{-1}$ [10].

The acoustic signal can also be generated directly by radiation pressure. The amplitude of the radiation pressure is given by $p_{rad} = I/c$, where $I$ is the intensity and $c$ is the light velocity in medium. A laser intensity of $10^6$ $Wcm^{-2}$, which is typical for our experiment, only corresponds to 0.3mbar pressure, thus this mechanism is the weakest one among all mechanisms discussed in this section.

In this dissertation, the term optoacoustic or OA implies acoustic generation via thermoelastic mechanism.

### 1.1.2. Relation of this work to previous research in optoacoustics with solids

Since the optoacoustic phenomenon was first discovered by Alexander Graham Bell in 1880 [13], it has been successfully used to perform many investigations on gases,

liquids and solids. Two factors that play an important role in the study of optoacoustics are the characteristics of the incident light source and detection techniques. Note that this work mainly focuses on the generation and detection of pulsed OA signals with solid samples.

**A. Light sources and methods to generate OA signals**

Both incoherent and coherent light sources have been used to conduct OA experiments. To generate an acoustic signal, the light intensity must be varying with time. This has been achieved either by chopping the beam from a continuous light source or by using a pulsed light source. The first OA experiment performed by Bell more than 100 years ago utilized chopped sunlight. In some of our experiments, we also used incoherent light pulses from passivation mixtures of an excimer laser. However, the signal to noise ratio increases greatly when coherent light pulses, which produce high fluencies, are used. Presently most optoacoustic work is performed with lasers.

Early OA experiments were done on gaseous samples with chopped light beams. This was because the OA generation efficiency in gases is higher than in condensed matter (the gas has a higher thermal expansion coefficient), and acoustic signals in gases are easily detected by sensitive microphones. In 1963, White first investigated OA generation with solid samples using chopped light beams [14]. These signals detected by microphones were actually indirect ones, since they were generated by thermal expansion in the surrounding air. The difference of the OA generation in a gaseous sample and the indirect OA generation with a solid sample, is that the former is caused by a direct absorption of laser energy by the gas while the latter is caused by the diffusion, into the

gas, from the optically generated thermal energy in the solid sample. In the early 1970s, this indirect generation of OA by a chopped light beam was investigated thoroughly, as for example by Rosencwaig [15] and Harshbarger [16]. In later years, pulsed lasers were often used to generate OA signals, since the OA generation efficiency by pulsed lasers is higher, as a result of higher incident intensities. Also, piezoelectric transducers became very popular. These transducers can directly detect acoustic signals in solids and are very sensitive to weak signals. After the late 1970s, much work on pulsed direct OA generation in solids has been done [8, 17-19].

However, the generation and detection of pulsed indirect OA signals in the gas in contact with the solid target has not been done by many workers. The work in this dissertation is one of the few such investigations. Except for Tam's work in the mid-1980s [20] and the work described in this dissertation, the author is not aware of other work on indirect pulse optoacoustic work using a totally non-intrusive optical probe beam deflection technique.

## B. OA detection schemes

Most authors used piezoelectric transducers to detect direct OA signals, without analyzing the performance of the transducer, by assuming that the detector's response was linear. It is known that the transfer function of a piezoelectric transducer displays a resonance whose frequency is determined by the thickness of the piezoelectric material and the sound speed in this material. Therefore, the linear approximation is only valid when the spectrum of the acoustic signal is at a region far away from the resonant

frequency. Note, however, that the responsivity in such a region is low compared with that at the resonant frequency.

A further feature of the work described in this dissertation is the additional complexity that had to be accounted for because the optoacoustic signals generated had strong components around the resonant frequency of the piezoelectric transducer used. In order to analyze the experimental results obtained we use Mason's model [21] for a piezoelectric material.

Since the early 1980s, optical detection of OA pulses has been amply investigated. In general, the sensitivity of the optical detection is smaller than that of the piezoelectric transducer. However, it provides a non-contact method to detect the acoustic signal. Therefore, OA diagnostics of material properties can be performed in a completely non-intrusive and non-contact manner. Such a feature makes the OA technique a powerful inspection tool in a hostile or inaccessible environment.

In these optical detection schemes, normally either the motion of the sample's surface or the change of the index of refraction is sensed by a probe beam. Interferometers have been used to detect the displacement of the surface [22, 23]. This method uses a coherent continuous probe beam. Alternatively, the beam deflection method was used to monitor the surface deformation by measuring the deflection angle of the probe beam due to the change of the slope of the surface [24, 25]. The beam refraction method also measures the bending of the probe beam, but this is due to the change of index of refraction along the optical path caused by the acoustic signal [26, 27]. This change of index of refraction has also been detected by the optical reflectivity method, which monitors the change of

the intensity of the reflected probe beam by the sample surface [28, 29]. This method is useful to detect the OA signal generated by picosecond laser pulses.

Most of the optical detection schemes require a smooth sample surface, which is not practical for many experiments. Although the beam refraction method does not require a smooth surface, the sample must be transparent to the wavelength of the probe beam. Recently, Caron and coworkers proposed the gas-coupled laser acoustic detection scheme [30, 31]. This method has the same detection mechanism as that used by the beam refraction method, but the probe beam is located in the gas and detects the acoustic signal transmitted from the solid sample. Therefore, it does not require a smooth surface and can be used for indirect detection of acoustic signals in almost all solid samples. However, since the transmission of an acoustic signal from the solid to the gas is very small due to the large acoustic impedance mismatch, this method is practical only when the acoustic signal in the solid is very strong.

The work in this dissertation uses the same experimental setup as that used by the gas-coupled laser detection scheme, but it detects the indirect OA signal generated in the gas instead of the transmitted OA signal from the solid. Since the efficiency of indirect OA generation is high, the acoustic signal can be detected by a probe beam even when the pump laser is weak.

### C. Theories of OA generation

Many authors have investigated the theory used to predict the profile of the OA signal in solids. For a weak absorption medium, cylindrical symmetry can be assumed [10]. For a highly absorbed sample, if the radius of the pump is small compared to the absorption

length, a spherical model can be used [32]. Otherwise, the acoustic wave can be treated as a plane wave [15].

To predict the OA signal profile, the sound speed in the sample, the optical absorption coefficient and the boundary condition must all be known. White directly derived the sinusoidal solution of the wave equation [14]. Patel and Tam used potential theory that was developed by Landau and Lifshitz [33] to first obtain the potential and then the pressure signal [10]. Burmistrova and coworkers developed the transfer function theory for the OA generation [34]. Our work adopted the transfer function theory, because it reveals clear pictures of the relevant processes, and the required convolution of the impulse response and the laser pulse profile can be easily performed by a computer. Our work also independently developed a numerical method to calculate the pulsed indirect OA generation.

**D. Signal processing of OA signals**

Most OA experimental results have been interpreted in time domain. Rarely has work been done to interpret OA signals in frequency domain [35]. Our work develops a method to obtain the time interval between acoustic echoes in frequency domain by the Fourier transform. We also utilize the wavelet transform theory to analyze the OA signal in the two-dimensional time-frequency space, as well as to remove noise from the experimental results. To the author's knowledge, this work is among the first which introduces these techniques to the processing of OA experimental data.

### 1.1.3. Applications

Many applications of optoacoustic techniques have been developed and demonstrated. These include OA spectroscopy [36], material characterization for parameters such as absorption coefficient [37], sound velocity and sample thickness [38]. There are many other applications in nondestructive evaluation [39], photochemistry [35] and biology [40].

OA spectroscopy has been widely investigated. Compared to other conventional methods for weak absorption media, OA spectroscopy has several advantages. For example, scattering and reflection losses are severe problems for optical spectroscopy but not for OA spectroscopy, because the OA signal only senses the absorbed energy. OA spectroscopy is also suitable for measuring very high absorption coefficients. In this case, the OA generation efficiency increases and it is easier to detect the OA signal. On the other hand, there is little light transmission in an opaque sample, making an absorption spectroscopy very difficult, if not impossible.

Optical absorption coefficients have been measured by using modulated incident light [41-43]. These methods measured the OA signal magnitudes or phases and required the knowledge of parameters such as the thermal expansion coefficient, heat capacity, laser intensity, etc.. Terzic and Sigrist proposed a method to get the optical absorption coefficient by pulsed OA measurement [37]. Their amplitude ratio technique eliminated the need to know the parameters mentioned above by taking measurements at two different boundary conditions. However, it requires one of these conditions to be rigid, which is difficult to achieve for many experiments.

Our work develops a novel method for the measurement of absorption coefficient, and also uses the ratio technique, but in the frequency domain. This method exploits differences due to varying boundary conditions but not necessarily a rigid boundary. In addition, it is inherently independent of the characteristics of the detector and the amplifiers.

Thin-film testing for the verification and quality control of electronic components, protective layers, or optical coating is in great demand. OA testing can be and has been used for this purpose [38]. To achieve enough resolution in thin film applications, picosecond longitudinal acoustic pulses must be excited with picosecond pump lasers. This technique has been used for ultra thin film (50nm ~ 10μm) to determine either the thickness or the sound velocity from the acoustic echo interval. Optical detection of a picosecond optoacoustic signal is usually required since the piezoelectric transducers do not have sufficiently short response times. For an opaque film, the OA signal is directly generated. For a transparent, thin film, the stress generation is not possible by absorption of the incident laser energy. However, stress can be generated in the opaque substrate. Part of the resultant acoustic pulse is transmitted into the film, and this is used for a diagnostic purpose.

The electroacoustic technique is a commonly used method for non-destructive evaluation (NDE), such as flaw detection. Compared with the electroacoustic method, optoacoustic evaluation has several advantages. First, since the pump laser can be well-focused, spatial resolution can therefore be improved. Second, nanosecond and even picosecond optoacoustic pulse can be generated. Therefore, shallow defects as thin as micrometers can be detected. Finally, by using optical detection of the OA signal, the

evaluation can be performed in a fully non-contact, non-intrusive manner. Such a method is useful in applications where the sample surface cannot be contaminated or it is located in an inaccessible environment.

OA evaluation is extremely useful for another category of NDE application to which the conventional electroacoustic method cannot be applied. In this category, the defect has the same acoustic impedance, but different optical properties, as the main body. An incident acoustic probe beam would not have reflection at the defect, thus it cannot detect the location of the defect. However, an internal OA signal can be generated by the defect itself if a properly chosen laser beam can penetrate the main body and reach the defect. A three-dimensional image of the defect can be obtained by scanning the pumping laser beam across the object.

OA technique has also found applications in biological samples such as optical absorption coefficient measurement in tissues [40], depth resolving [44], selective ablation [45] and penetration of sunscreen into skin [46]. This dissertation also worked on measuring properties of tissue samples at different laser wavelengths [47].

## 1.2. STRUCTURE OF THIS DISSERTATION

This dissertation has seven chapters. Following this introduction is Chapter II, which describes the physics of the pulsed optoacoustic phenomenon. Although most of the theory has been done by earlier researches, we put these results together with our own contributions to give readers a thorough picture of this phenomenon from generation to propagation and finally detection.

In Chapter III, methods used to theoretically calculate electrical signals from a piezoelectric detector or a photodiode, based on the theories described in the previous chapter, are given in detail. These calculations were done to compare theory with experiments, which are described in detail in Chapter IV. In this chapter, a comparison between theoretical and experimental results is also presented.

Chapter V presents methods that we developed to analyze and process the OA experimental data by Fourier and wavelet transforms.

Finally, in Chapter VI, two new applications of the OA technique are given. First, we investigated a new way to measure the optical absorption coefficient. Both the theory and its application to the experimental results are presented. Then, the pulsed OA experiment with biological tissue samples were described. Some techniques developed in this work were used to process the experimental results from tissue samples. This chapter is followed by a conclusion chapter that ends this dissertation.

# CHAPTER II

# PHYSICS OF GENERATION, PROPAGATION AND DETECTION OF OPTOACOUSTIC SIGNALS

This chapter deals with the theories of generation of ultrasound by pulsed lasers, and the propagation and detection of acoustic signals. The emphasis here is on the generation and detection.

## 2.1. GENERATION OF ACOUSTIC PULSES BY LASER EXCITATION IN OPTICALLY UNIFORM MEDIA

In this section, the mechanism of optoacoustic generation will be discussed. When the energy of a laser pulse is absorbed by a solid sample in contact with a fluid such as the air, an acoustic pulse is generated within the sample. This is a direct generation of ultrasound due to the laser energy absorption. However, the heat converted from the laser energy that is absorbed by the solid sample will partially diffuse to the adjacent fluid, which will generate another acoustic pulse in the fluid. This mechanism is called indirect generation. Both direct and indirect generation of OA pulses will be discussed here.

### 2.1.1. Direct Generation - Acoustic pulses generated within the absorbing sample

Because the transducer we used in our experiments for direct detection is only sensitive to the longitudinal acoustic waves, we will deal mainly with the longitudinal

pressure or displacement signals in this section. To simplify the discussion and get a clear picture of the physical phenomenon, we will start with a one-dimensional model, which is normally sufficient for the case when the optical absorption coefficient is not too large, i.e., the length of the absorption region cannot be ignored. We will concentrate on this one-dimensional theory and extend the discussion to a more general, three-dimensional model which is necessary when the optical absorption is sufficiently large.

A general formulation of the theory needed to describe the generation of an optoacoustic pulse is given. This involves the solution of two coupled equations, namely the acoustic wave equation with a source term and a thermal diffusion equation. The one-dimensional model will be discussed in detail to approach the solutions, followed by a brief description of the three-dimensional case.

The acoustic wave may be approximated as a plane wave when the conditions $a >> d_0$ and $a^2/\lambda >> d_0$ hold, where $a$ is the radius of the laser beam, $d_0$ is the thickness of the absorption layer and $\lambda$ is a characteristic wavelength of the acoustic signal. The acoustic wave equation can be derived from the continuity equation for mass and Newton's second law, which are written as Eqs. (2.1a) and (2.1b):

$$\rho(1+\frac{\partial u}{\partial z}) = \rho_0, \tag{2.1a}$$

$$\rho_0 \frac{\partial^2 u}{\partial t^2} + \frac{\partial p}{\partial z} = 0. \tag{2.1b}$$

Here $u$ is the displacement, $\rho$ is the mass density and $\rho_0$ is its value at equilibrium. In Eq. (2.1b) $p$ is the pressure, which depends on the displacement gradient and thermoelastic expansion:

$$p = -c_0^2 \rho_0 \frac{\partial u}{\partial z} + c_0^2 \rho_0 \theta T' . \tag{2.2}$$

Here, $\theta$ is the linear thermal expansion coefficient, $c_0$ is the sound speed and $T'$ is the temperature increment. The first term on the right hand side of Eq. (2.2) is the regular relation of the stress (negative pressure) and the strain. The second term is the contribution from thermal expansion. Combining Eqs. (2.1) and (2.2), one gets the wave equation for displacement:

$$\frac{\partial^2 u}{\partial t^2} = c_0^2 \frac{\partial^2 u}{\partial z^2} - c_0^2 \theta \frac{\partial T'}{\partial z} . \tag{2.3}$$

Replacing $u$ by $p$ according to the relation in Eq. (2.2), the wave equation for pressure can be modified from Eq. (2.3) and written as:

$$\frac{\partial^2 p}{\partial z^2} - \frac{1}{c_0^2} \frac{\partial^2 p}{\partial t^2} = -\rho_0 \theta \frac{\partial^2 T'}{\partial t^2} . \tag{2.4}$$

Eq. (2.4) can be extended to the three-dimensional case for a homogeneous and isotropic medium without loss. Then the pressure wave equation can be written as [48]

$$\nabla^2 p - \frac{1}{c_0^2} \frac{\partial^2 p}{\partial t^2} = -\frac{\theta}{C_p} \frac{\partial H}{\partial t} . \tag{2.5}$$

Here $C_p$ [$Jkg^{-1}K^{-1}$] is the specific heat at constant pressure and $H(\mathbf{r},t)$ [$W/m^3$] is the net heat flowing into the observation point per unit time, per unit volume. In the above equation, the source term is written in terms of heat instead of temperature. They are interchangeable by the relation $\partial T'/\partial t = H/(\rho C_p)$.

In Eq. (2.5), the thermal expansion coefficient $\theta$ [1/K] for a bulk medium is defined as

$$\theta = -\frac{1}{\rho_0}\left(\frac{\partial \rho_0}{\partial T}\right)_P, \tag{2.6}$$

where $T$ is the absolute temperature.

When there is no external heat disturbance, i.e. the right hand side of Eq. (2.5), which is the source term, equals zero, then Eq. (2.5) becomes the standard wave equation. The general solution then has the format of $f(c_0 t \pm z)$ for one-dimensional equation, and the signal profile $f(x)$ is determined by appropriate boundary and initial conditions.

When the source term is present, which is always the case for optoacoustic generation, the general solution is usually difficult to obtain. One reason is that it is often difficult to find the exact functional form for $H(\mathbf{r}, t)$.

The heat power flow density, $H(\mathbf{r}, t)$, at time instant $t = t_0$ and position $\mathbf{r} = \mathbf{r}_0$, has two components. The first part, $H_{opt}(\mathbf{r}_0, t_0)$, is the instantaneous heat converted from the laser energy that is absorbed at position $\mathbf{r}_0$ and at time instant $t_0$. $H_{opt}$ is determined by the optical absorption coefficient $\alpha$. The second part, $H_{th}(\mathbf{r}_0, t_0)$, is the heat generated at $t < t_0$ which has reached $\mathbf{r}_0$, by thermal diffusion, from any $\mathbf{r} \neq \mathbf{r}_0$.

The instantaneous heat converted from laser absorption $H_{opt}$ can be expressed by:

$$H_{opt}(\mathbf{r}, t) = -\nabla I(\mathbf{r}, t), \tag{2.7}$$

where $I$ is the laser intensity. If it is assumed that the laser beam is incident from $-z$ direction and obeys Beer's law, $H_{opt}(z)$ is therefore,

$$H_{opt}(z, t) = \alpha I_0(t) e^{-\alpha z}. \tag{2.8}$$

$I_0(t)$ describes the temporal profile of the laser pulse before it is absorbed by the sample.

There are two general limiting conditions that can be described in terms of whether the absorption is strong or weak. If the absorption is weak, i.e. $e^{-\alpha z} \ll 1$, the gradient of

$H_{opt}$ in $z$ direction can be neglected compared with the gradient in transverse ($x$ and $y$) directions which is determined by the geometries by the laser beam. Then the thermal expansion occurs in transverse directions. The wave equation can be solved in a cylindrical coordinate system [10]. If the absorption is strong, the laser energy is absorbed within a thin top layer (about $1/\alpha$). The initial temperature decays exponentially in the $z$ direction. Here, it is convenient to proceed by discussing two limiting geometries, namely: (a) when the diameter of the laser beam is large enough, and satisfies the conditions stated in the beginning of this section, then the optoacoustic signal can be taken to be one dimensional in the $z$ direction. As discussed in Chapter IV, in most of our experiments, this assumption is justified; (b) when the absorption length is comparable to the diameter of the laser beam, then the solution can be written in the spherical coordinate [32].

Thermal diffusion is caused by the non-uniform temperature distribution that exists within the material. In an optoacoustic experiment, the thermal diffusion equation for temperature can be written as [49]:

$$\nabla^2 T = \frac{1}{D}\frac{\partial T}{\partial t} - \frac{H_{opt}}{\kappa}, \tag{2.9}$$

where $\kappa$ [$Wm^{-1}K^{-1}$] is the thermal conductivity and $D$ [$m^2/s$] is the thermal diffusivity. $D$ is related to $\kappa$ by the following formula:

$$D = \kappa / \rho C, \tag{2.10}$$

where $\rho$ is the density and $C$ is the specific heat. Since $H_{th}$ is directly related to the temperature, $H_{opt}$ and $H_{th}$ are coupled via Eq. (2.9).

In summary, the formulation of the appropriate optoacoustic pulse profile requires a solution to the two coupled equations, Eqs. (2.5) and (2.9).

## A. One-dimensional model

To solve the pressure wave equation Eq. (2.5) (or Eq. (2.4) for one dimension), one needs to know the temperature distribution and the initial and boundary conditions. When the laser pulse is short, one can assume that the temperature rises and the thermal expansion occurs on a time scale short enough that the medium has not yet reformed its density, i.e., $\partial u / \partial z = 0$. Therefore, the first term at the right hand side of Eq. (2.2) can be ignored. Then the pressure changes are merely due to the thermal expansion [50] (second term in Eq. (2.2)). To treat the acoustic generation problem, one can take a two-step approach: first a pressure pulse is initiated at time zero within the absorption region by thermal expansion; then the pressure pulse travels, obeying the wave equation for a homogenous medium.

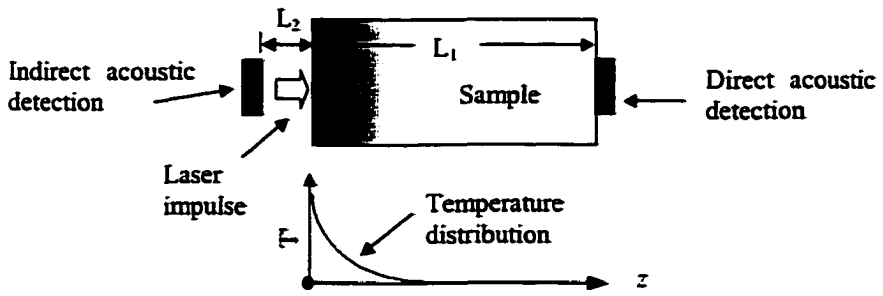


Fig. 2.1. Optoacoustic generation by a laser impulse and the detection.

Let us assume the ideal experiment illustrated in Fig. 2.1. A laser impulse with intensity $I_0\delta(t)$ (and the flux is $E_0$Joules/m$^2$) irradiates the sample surface. An acoustic detector can be placed either on the back of the sample, to directly measure the pressure signal, or in front of the surface at distance $L_2$, to detect the signal transmitted into the adjacent medium (which normally is air, and such detection is referred to as an indirect measurement). Note that an ideal indirect measurement should record not only the transmitted acoustic pulse but also an acoustic signal generated in the fluid due to heat diffused from the sample's surface. The profile of the latter signal will be discussed in section 2.1.2. In this section, the indirect signal refers only to the transmitted acoustic pulse from the solid.

The time it takes for the light to travel across the absorption region can be neglected. Also, the time for the temperature rise can be ignored, because such a rise occurs on a time scale of picoseconds while this work treats laser pulses in nanoseconds. The initial distribution of the temperature increment (at time zero) according to Beer's law can therefore be written as:

$$T'(t=0,z)=\frac{\alpha E_0 e^{-\alpha z}}{\rho C_p}, \tag{2.11}$$

where $\alpha$ is the optical absorption coefficient of the sample at the incident laser wavelength. Therefore, from Eq. (2.2) the pressure signal initiated at time zero can be written as:

$$p(t=0,z)=\frac{c_0^2\theta\alpha E_0 e^{-\alpha z}}{C_p}, (z\geq 0). \tag{2.12}$$

After time zero, the initial pressure signal will split into two counter-propagating pulses. The indirect detector located at $z = -L_2$ will see the transmitted portion of the

signal propagating in the $-z$ direction after a time delay $\tau_2 = L_2/c_2$, where $c_2$ is the sound speed in the fluid. This pressure signal can be written as:

$$p(t, z = -L_2) = \frac{k_t}{2} \frac{c_0^2 \theta \alpha E_0 e^{-\alpha c_0 (t-\tau_2)}}{C_p}, (t \geq \tau_2 = L_2 / c_2). \tag{2.13}$$

In the above equation, $k_t$ is the transmission coefficient. The normalized pressure signal is shown in Fig. 2.2(a).

On the other hand, the direct detector located at $z = L_1$ will first see the pulse propagating in the positive direction whose peak arrives at $\tau_1 = L_1 / c_0$. Then it records the reflected portion of the pulse that originally travels toward the negative direction but is reflected at the irradiated surface. The time delay for the detector to see the reflected signal is also $\tau_1$. Therefore, the signal that the direct detector measures can be written as:

$$\begin{aligned} p(t, z = L_1) &= \frac{1}{2} \frac{c_0^2 \theta \alpha E_0 e^{\alpha c_0 (t-\tau_1)}}{C_p}, (0 \leq t \leq \tau_1), \\ p(t, z = L_1) &= \frac{k_r}{2} \frac{c_0^2 \theta \alpha E_0 e^{-\alpha c_0 (t-\tau_1)}}{C_p}, (t \geq \tau_1). \end{aligned} \tag{2.14}$$

In Eq. (2.14), $k_r$ is the reflection coefficient. The combined pressure signal is illustrated in Fig. 2.2(b).

Note that the indirect signal in Fig. 2.2(a) is always positive, since the transmission coefficient $k_t = 2Z_2/(Z_1 + Z_2)$, where $Z_1$ and $Z_2$ are the acoustic impedance of the sample and the adjacent fluid respectively, is always a positive number. However, the second wing of Fig. 2.2(b) has the same polarization as the reflection coefficient $k_r$, where $k_r = (Z_2 - Z_1)/(Z_2 + Z_1)$. Therefore, $k_r$ can be either positive or negative, and is

determined by the impedances of the sample and the adjacent medium. For the rigid boundary, $Z_2 = \infty$ and $k_r = 1$, in which case the directly detected signal has even symmetry centered at $t = L_1/c_0$. For the free boundary, $Z_2 = 0$ and $k_r = -1$, in which case the symmetry is odd for the direct signal.

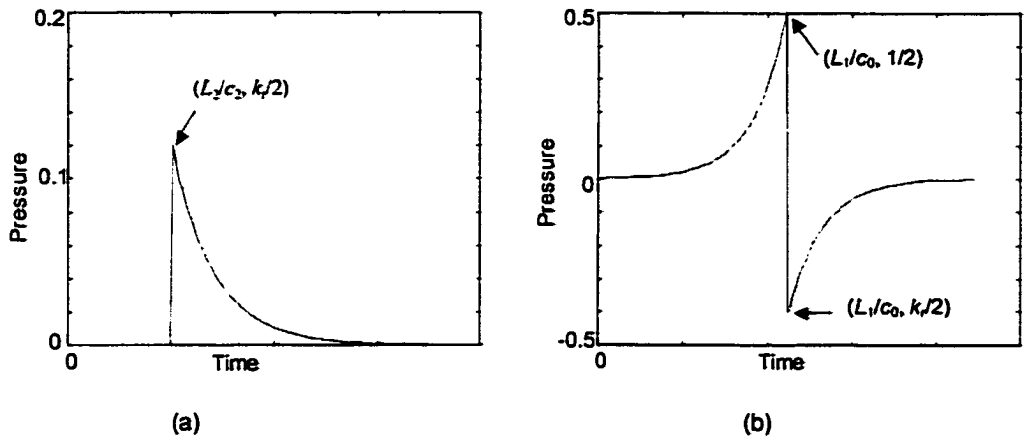


Fig. 2.2. Pressure signals generated by a laser impulse and measured by detectors located at (a) $x = -L_2$ and (b) $x = L_1$. The signals have been normalized to $p(x = 0, t = 0)$. The reflection coefficient $k_r = -0.8$. The transmission coefficient $k_t = 0.24$. Note these coefficients are for pressure amplitude. Therefore, $k_r + k_t \neq 1$.

Another interesting thing one may notice is that the pressure signal is a positive pulse. (The negative part in Fig. 2.2(b) is due to the negative reflection coefficient at the boundary.) Although an all-positive signal satisfies the wave equation, such a pressure pulse does not physically exist in a sample. This is because an all-positive pressure pulse forces a particle to move toward one direction without turning back to its equilibrium position, which is not true for an elastic wave. However, for an optoacoustic experiment, such an all-positive pressure signal is a good approximation as long as the thermal

diffusion occurs more slowly than the sound speed, which means the particle will move quickly away from, but return slowly to, its equilibrium position.

By taking the Fourier transform of Eqs. (2.13) and (2.14), the signal in the frequency domain is obtained as follows.

The spectrum of the normalized indirect signal shown in Fig. 2.2 is:

$$P(\omega, z=-L_2)=\frac{e^{-j\omega\tau_2}}{2}\frac{k_t}{\alpha c_0+j\omega}. \tag{2.15}$$

For the direct measurement:

$$P(\omega, z=L_1)=\frac{e^{-j\omega\tau_1}}{2}\frac{\alpha c_0(1+k_r)+j\omega(1-k_r)}{(\alpha c_0)^2+\omega^2}. \tag{2.16}$$

In Fig. 2.3, where the signals are plotted in the frequency domain, one sees that the impulse response of a direct measurement of a free ($k_r$ = -1) or free-like ($k_r$ < 0) boundary is a bandpass filter; while for a rigid ($k_r$ = 1) or rigid-like ($k_r$ > 0) boundary, the impulse response is a lowpass filter. If the detection is indirect, the impulse response is always a lowpass filter.

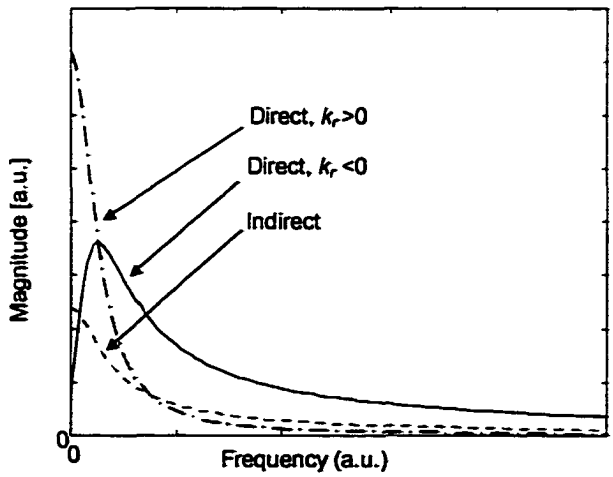


Fig. 2.3. Spectrum of pressure signals generated by laser impulse at different boundaries and measured either directly or indirectly.

In general, the laser pulse width cannot be neglected. Then the optoacoustic signal is obtained by the convolution of the temporal profile of the laser pulse and the impulse response. This impulse response is given by either Eq.(2.13) or (2.14), depending on the detection scheme. Equivalently, the signal spectrum is the multiplication of the spectrum of the laser pulse and the system transfer function, either Eq. (2.15) or (2.16).

There are two limits that are of special interest because they allow one to have a quick qualitative estimate of the OA signal profile. These are the absorption length limit and the laser pulse width limit. For the absorption length limit, either the absorption is weak or the laser pulse width is narrow, i.e., $\alpha c \tau_L << 1$. For this case, the laser pulse can be treated as an impulse and the pressure signal follows Fig. 2.2. For the laser pulse width limit, $\alpha c \tau_L >> 1$. For indirect detection or direct detection under the rigid boundary condition, the pressure signal follows the laser pulse profile. For direct detection under the free boundary condition, the pressure profile is approximately the first time derivative of the laser pulse profile, i.e., the displacement signal follows the laser pulse profile. Therefore, from the detected OA signal profile, one is able to roughly estimate the order of the absorption coefficient if the laser pulse width and the sound speed are known.

Eq. (2.5) states the relation of heat and pressure in the solid. For convenience, we identify two contributions to the heat term, namely the direct heat deposited by the laser pulse and the heat that has diffused from other locations. Consequently, the acoustic signal can be considered as the combination of an optoacoustic portion (from the laser energy deposition) and a portion that we call thermo-acoustic wave (from thermal diffusion). Here we describe an analytical method to solve the thermal diffusion equation and obtain the temperature distribution in the sample. This is the first step in obtaining

the thermo-acoustic signal. Then, the conditions that allow one to neglect the thermal diffusion effect will be analyzed.

To simplify the problem, assume that the initial temperature increment distribution is formed by the absorption of a laser impulse. At time $t = 0$, the distribution can be described by Eq. (2.9). At anytime thereafter, the distribution of $T'$ can be obtained by the convolution of its initial condition (Eq. (2.9)) and the impulse response of the diffusion equation without the source term. Here the impulse response refers to the temperature distribution at any time by assuming that the initial distribution is a delta impulse. The source-free one-dimensional thermal diffusion equation can be written as (modified from Eq. (2.7)):

$$\frac{\partial^2 T'}{\partial z^2} = \frac{1}{D}\frac{\partial T'}{\partial t}. \tag{2.17}$$

Since the thermal conductivity of air is much smaller than that of the solid sample used in our experiments, as an approximation we assume that no thermal energy diffuses into the air surrounding the surface. The solution of Eq. (2.17) for a half-infinite medium with a delta temperature impulse initiated at the boundary $z = 0$ can be written as:

$$T'_p(z,t) = Ct^{-1/2}\exp(-\frac{z^2}{4Dt}), (z>0), \tag{2.18}$$

where $C$ is a constant and can be obtained by realizing that the integration of $T'$ over $z$ at any time should be conservative (which is required by energy conservation). The subscript $p$ denotes the impulse response.

Therefore, the temperature distribution can be calculated as:

$$T'(x,t) = C'\int_0^\infty t^{-1/2}\exp(-\frac{(z-z')^2}{4Dt})\exp(-\alpha z')dz', \tag{2.19}$$

where $C'$ is a new constant which is a product of $C$ in Eq. (2.19) and constant $\alpha E_0 / \rho C_p$ in Eq. (2.11). In practice, $C'$ can be obtained by the same method used for getting $C$.

If the laser pulse width cannot be neglected, at each instant a certain amount of laser energy is absorbed and causes an additional temperature increment with a distribution over the space. This additional temperature increment, plus the previous distribution, forms a new initial condition and then starts to diffuse, as described by Eq. (2.19). This process (i.e., heat absorption and simultaneous diffusion) repeats until all the energy of the laser pulse has been deposited into the sample. Thereafter, the process of thermal diffusion continues until all heat spreads out evenly in the whole sample.

Note that Eq. (2.19) is valid only when no energy diffuses out of the sample. In Chapter III, we develop a numerical method that solves the diffusion equation with arbitrary boundary conditions and with external heat sources. This is especially useful for the case of indirect OA generation where the energy diffused to air must be considered. The thermal diffusion equation with general boundary conditions can also be solved by a method combining the Rosencwaig-Gersho model introduced in 2.1.2.A and the Fourier transform technique. This really is an analytical method. We will show that both the numerical and the analytical methods yield identical results in Chapter III.

After obtaining the temperature spatial distribution at all time, one is able to calculate the thermo-acoustic signal. Note that thermal diffusion is a continuous process. At each instant, the newly generated acoustic signal that is proportional to the temperature changes is added to a shifted version of the previous acoustic signal because the acoustic signal keeps on moving at the sound velocity. If one is only interested in the signal profile, the thermo-acoustic signal can be calculated from the following equations [28]:

$$p_{ta}(z-ct)=\int_{-\infty}^{\infty}dt'\int_{0}^{\infty}dz'\frac{\partial T(z',t')}{\partial t'}\delta(z'-z+c(t-t'))\ (z>ct),$$
$$p_{ta}(z-ct)=\int_{-\infty}^{\infty}dt'\int_{0}^{\infty}dz'\frac{\partial T(z',t')}{\partial t'}[\delta(z'-z+c(t-t'))+k_r\delta(z'+z-c(t-t'))]\ (z<ct). \tag{2.20}$$

Here, the effect of reflection at the boundary has been included.

In general, the treatment of the coupling of optoacoustic and thermo-acoustic effects is computationally intensive. However, this is not necessary for many applications where the optoacoustic and thermo-acoustic signals are effectively decoupled. This usually happens, for instance, in experiments where non-metal samples are used.

Thermal diffusion can be neglected if all the following conditions apply [51]:

$$d >> D/c_0, \tag{2.21}$$

$$d >> \sqrt{D\tau_L}, \tag{2.22}$$

and

$$c_0^2\tau_L >> D. \tag{2.23}$$

Here $d$ is the thickness of the optical absorption region, $\tau_L$ is the width of the laser pulse and $c_0$ is the sound velocity. Condition (2.21) shows that the acoustic signal initiated at the surface has moved out of the heating region when its corresponding heat source spreads out of the same length $d$. Condition (2.22) shows that the laser pulse width should not be so long that the resultant thermal energy has diffused out to a dimension greater than $d$ before the laser source term ends. On the other hand, Condition (2.23) shows that the laser pulse should be long enough so that the acoustic signal travels the dimension $c_0\tau_L$ before the heat spreads out to this length, during the duration of the laser pulse.

The above conditions can be derived from the comparison of the propagation of an acoustic wave and the diffusion of the temperature with the format $t^{-1/2}\exp(-\frac{z^2}{Dt})$.

In fact, condition (2.21) can be derived from conditions (2.22) and (2.23). From (2.23) one gets

$$\tau_L >> D/c_0^2. \tag{2.24}$$

Substituting (2.24) into (2.22), one gets (2.21).

Conditions (2.22) and (2.23) can also be derived from the concept of thermal wave. We will show in section 2.1.2.A, the thermal wave has a diffusion length $\mu = \sqrt{\frac{2D}{\omega}}$ and a speed of $\sqrt{2\omega D}$, where $\omega$ is the frequency of the thermal wave. In order for thermal and optoacoustic waves to decouple, the diffusion length should be much smaller than the optical absorption length and the speed of the thermal wave should be much smaller than that of the acoustic wave, i.e.,

$$\sqrt{\frac{2D}{\omega}} << d, \tag{2.25}$$

and

$$\sqrt{2\omega D} << c_0. \tag{2.26}$$

Substituting $\omega = 2\pi/\tau_L$ into (2.25) leads to (2.22) and into (2.26) leads to (2.23).

Note, however, that (2.22) and (2.23) together are sufficient conditions for (2.21) but not necessary conditions. Our simulation in Chapter III shows that actually (2.21) is the most important condition. As long as (2.21) is met, the rest of the conditions can be

broken without causing a dramatic coupling of optoacoustic and thermo-acoustic signals for pulsed experiments.

**B. Three-dimensional model**

The above one-dimensional model deals with the longitudinal pressure signal due to the longitudinal thermal expansion at the absorption region. It is a good approximation when such a pressure is much larger than the pressure caused by the longitudinal displacement induced by the transverse thermal expansion. When the absorption coefficient is extremely large and the surface is exposed to air, the latter is dominant. The transverse-expansion-induced longitudinal displacement can be described by a three-dimensional model. These three-dimensional equations had been solved by the Green function method using a double Laplace-Hankel transform technique [52-54]. Shujun Yang, another Ph.D. student in our research group, is currently investigating this three-dimensional model. Although the details of the theoretical treatment will not be given in this dissertation, here we interpret the typical displacement profile from a physical aspect without introducing any equations. This description is rarely seen in the literature.

When the light pulse irradiates an extremely highly absorptive surface, the absorption depth is very thin. For instance, this depth is about 10nm for metals [28]. (As a comparison, the absorption depths of the non-metallic materials that we used in our experiment are in the order of micrometers, and the one-dimensional model works well). For such a highly absorptive material, the light energy is deposited on the surface. If this surface is exposed to air, which is the case for most OA experiments, the air-solid interface is effectively a free boundary. Therefore, no longitudinal pressure can be

initiated from the absorption region because of the free boundary. The transverse expansion exists and forms a transverse wave propagating to the detector. A transverse expansion results in a longitudinal compression, which is similar to the mechanism of a radial compression induced by mechanically pulling a rod in the axial direction.

Fig. 2.4 shows a typical longitudinal displacement profile of the OA signal generated by a spatially wide and uniform surface impulse heat source. It is a theoretical result produced by Shujun Yang. Note that this discussion assumes an ideal displacement detector located at the epicenter at the other side of the sample. The transverse expansion at the surface generates a longitudinal compression. This displacement is defined to be negative and starts to propagate toward the detector at the longitudinal sound speed $c_L$. If the distance from the surface to the detector is $L$, then the longitudinal displacement wave will arrive at the detector after a delay of $L/c_L$. In the meantime, a shear wave driven by the transverse expansion at the surface propagates toward the detector at the shear wave sound speed $c_s$. During the propagation of the shear wave, new longitudinal displacements are formed and ultimately accumulate at the detector until the shear wave reaches the detector after a delay of $L/c_s$. The arrival of the shear wave causes a surface deformation of the contact displacement detector, which has an upward longitudinal component.

The above discussion neglects the thermal diffusion effect. Therefore, the displacement stays at certain level after the arrival of the shear wave. If the thermal diffusion is included, this displacement will ultimately change back to zero (i.e., its equilibrium position). The rate of this change is determined by the thermal diffusion constant.

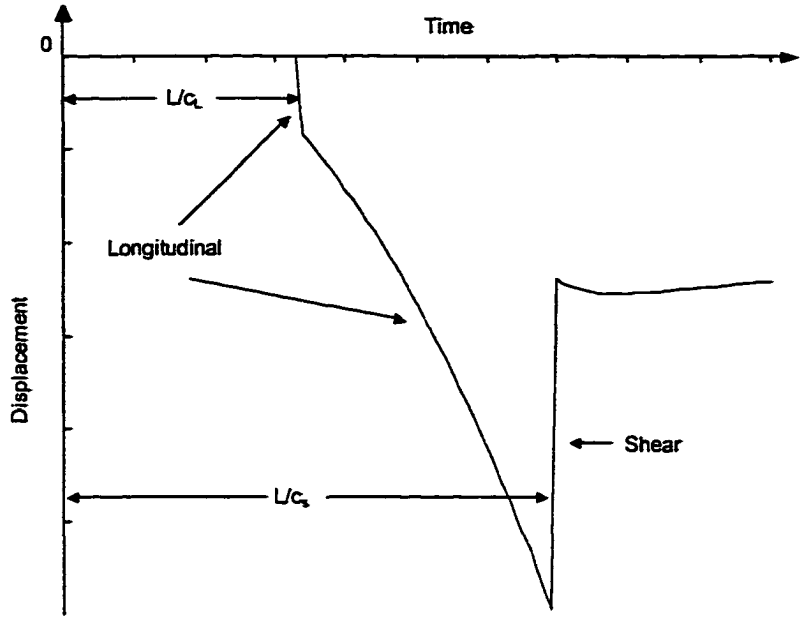


Fig. 2.4. A typical longitudinal displacement profile of the OA signal generated by a spatially wide and uniform surface impulse heat source.

### 2.1.2. Indirect Generation - Acoustic pulses generated in the fluid surrounding the solid surface

The indirect OA generation discussed here refers to the case where the fluid that surrounds the solid sample does not absorb the laser energy. While an OA signal is generated in the solid sample due to thermal expansion occurring within the sample, the heat generated in the sample will also diffuse across the solid-fluid boundary into the fluid. Therefore, another OA signal will be generated due to thermal expansion in the fluid. This is the so-called indirect OA generation.

In this section, a brief description of the theory of indirect OA generation by a sinusoid light source is given, followed by a discussion of our extension to pulsed OA generation.

The method used to calculate the indirect OA signal is to first calculate the temperature field in the fluid, and to then apply Eq. (2.5) to get the pressure signal. The temperature field excited by a sinusoid heat source in the solid was first solved by Rosencwaig and Gersho [55]. This is often referred to as the RG model.

## A. The Rosencwaig-Gersho model for calculation of the temperature field

The one-dimensional RG model is shown schematically in Fig. 2.5. The incident light is assumed to be a uniform plane wave, as is the generated thermal wave. This model solves the heat diffusion equation for each layer in $z$ direction. The solutions show that the temperature varies as a highly attenuated wave in each layer.

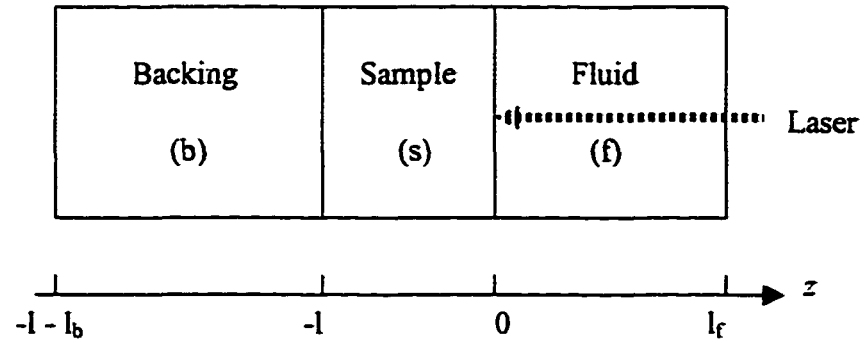


Fig. 2.5. Geometry of the RG model. The laser is incident at $z = 0$ from the right side and is only absorbed by the sample, but not the coupling gas or liquid.

The light flux comes from the right side and reaches the surface of the sample at $z$=0. The fluid that surrounds the sample could be a coupling gas, liquid, or simply the atmosphere. In general, the sample can have a backing. It is assumed that neither the fluid

nor the backing absorbs the light energy. The existence of the fluid and the backing in this one-dimensional model is to provide a temperature reference. The temperature $T(z, t)$ used in the following formulation is actually the temperature rise at location $z$ and time $t$ referring to the far ends of the fluid and the backing. Therefore, the lengths of these two layers $l_f$ and $l_b$ should be infinity or at least long enough to ensure that the "thermal wave" initiated at $z$=0 has already died off to zero when it reaches these two ends. (See the boundary conditions of Eq. (2.28)).

Let subscripts $f$ denote the layer of fluid, $s$ the sample, and $b$ the backing. The heat diffusion equations for the three layers are then:

$$\frac{\partial^2 T_f}{\partial z^2} = \frac{1}{D_f}\frac{\partial T_f}{\partial t} \qquad \text{(within the fluid),} \qquad (2.27a)$$

$$\frac{\partial^2 T_s}{\partial z^2} = \frac{1}{D_s}\frac{\partial T_s}{\partial t} - A\exp(\alpha z)(1+\exp(j\omega t)) \qquad \text{(within the sample),} \qquad (2.27b)$$

$$\frac{\partial^2 T_b}{\partial z^2} = \frac{1}{D_b}\frac{\partial T_b}{\partial t} \qquad \text{(within the backing).} \qquad (2.27c)$$

The boundary conditions for the three layers are:

$$T_f(z=0) = T_s(z=0), \qquad k_f\frac{dT_f}{dz}(z=0) = k_s\frac{dT_s}{dz}(z=0), \qquad (2.28a)$$

$$T_s(z=-l) = T_b(z=-l), \qquad k_s\frac{dT_s}{dz}(z=-l) = k_b\frac{dT_b}{dz}(z=-l), \qquad (2.28b)$$

$$T_f(z=l_f) = T_b(z=-l-l_b). \qquad (2.28c)$$

The above equations assume that the light flux is modulated sinusoidally at a frequency $\omega$ and the absorption of the light obeys Beer's law. The steady-state solutions of Eq. (2.27) are given by:

$$T_f(z,t) = B\exp(-\sigma_f z + j\omega t), \tag{2.29a}$$

$$T_s(z,t) = [U\exp(\sigma_s z) + V\exp(-\sigma_s z) - E\exp(\alpha z)]\exp(j\omega t), \tag{2.29b}$$

$$T_b(z,t) = W\exp[\sigma_b(z+l) + j\omega t]. \tag{2.29c}$$

Here constants $B$, $U$, $V$, $E$, and $W$ are complex and related to parameters $\alpha$, $k_i$, $D_i$, and geometry $l_i$ etc. The expressions for these constants can be found in references [55] or [56].

In solutions Eq. (2.29), $\sigma_i$ is given by:

$$\sigma_i = \sqrt{\frac{j\omega}{D_i}} = \frac{1+j}{\mu_i}, \tag{2.30}$$

where $\mu_i$ is the thermal diffusion length. It is a characteristic parameter and is defined as:

$$\mu_i = \sqrt{\frac{2D_i}{\omega}}. \tag{2.31}$$

The solutions given by Eq. (2.29) show that the heat diffusion is a thermal wave with a wavelength $2\pi\mu_i$, and a speed $\sqrt{2\omega D_i}$. The amplitude quickly decreases with an attenuation constant $1/\mu_i$, which means the thermal wave is important only within a range less than one wavelength. Like other waves, the thermal wave can reflect, diffract and interfere. For example, because of the possibility of the reflection at each interface, there may exist waves propagating in both directions within the sample layer. The first term of solution (2.29) represents a wave in the $+z$ direction, and the second term is a wave in the $-z$ direction. The third term represents the temperature rise from the absorption of light energy. However, because the thermal wave is highly attenuated, both the fluid and the backing are equivalent to semi-infinite layers. Therefore, only a unidirectional wave exists in both of these two layers. This is shown in expressions Eqs. (2.29a) and (2.29c).

**B. Indirect pulsed OA signal in the fluid**

The mechanism of indirect optoacoustic generation in the fluid is the same as the electro-acoustic generation in the sample. Both are due to the thermal diffusion, while one occurs in the fluid and the other in the sample. To theoretically obtain the profile of this indirect OA signal in the fluid, one needs to know the temperature distribution in the fluid for all time.

The RG model introduced above solves the temperature distribution at each layer including the fluid with a sinusoidal heat source. Therefore, it cannot be directly used to calculate the indirect OA signal pumped by a pulsed laser. However, we can decompose the heat pulse into sinusoidal components by the Fourier transform, then apply RG's solution at each frequency and finally assemble thermal waves at all frequencies into a temperature pulse by the inverse Fourier transform. The process of this method is straightforward except for the treatment of the zero frequency. At zero frequency, $\sigma$ is zero and constants $B$, $U$, $V$, $E$, and $W$ turn to infinity according to the RG theory. However, the coefficient of the zero frequency component can be set to any value without affecting the shape of the profile because this coefficient is the DC average of the inversed signal. Practically this coefficient is determined by the initial condition, i.e., all temperatures at time zero are zero.

We have independently developed a numerical method to solve the diffusion equation with external heat sources and with general boundary conditions. This method will be presented in Chapter III. There we will show that the results from our numerical method and from the RG model combined with the decomposition-recombination technique are in good agreement.

After obtaining the temperature anywhere and at anytime, one can calculate the indirect pulse OA signal using the same method as that for calculating the thermo-acoustic signal in the sample, which is described by Eq. (2.20).

## 2.2. PROPAGATION OF OA SIGNAL IN SOLIDS

Since the acoustic detector is often located beyond the absorption region, the OA signal must travel over a finite distance to reach the detector. If one desires to use the echoes of the original acoustic pulse, this pulse must travel within the sample over a distance of at least twice the thickness. While propagating, the acoustic wave always suffers losses and distortions caused by various mechanisms. While detailed investigations of these mechanisms are beyond the scope of this work, these factors still need to be considered when we analyze the signal detected at the remote site.

Some samples have multiple layers, and all piezoelectric transducers have multi-layer structures. Multi-reflection occurs at each interface between two different layers. These reflections may make the detected signal very complex. However, the acoustic wave propagation at multiple layers can be theoretically treated in a systematic manner as shown below.

### 2.2.1. Attenuation and distortion

Acoustic attenuation in a medium includes transmission losses at impedance mismatched boundaries, absorption, scattering and diffraction. Distortion often accompanies attenuation, because most acoustic loss mechanisms are frequency dependent.

For acoustic absorption, the classical theory reveals that the absorption coefficient is proportional to $\omega^2$ [48]. Therefore, high frequency components die off more quickly than the lower ones in a pulse. For most experiments, the absorption losses are smaller than other losses.

Scattering losses are dependent on the acoustic wavelength and the grain size of the material. A typical wavelength of our OA signals is about 0.3mm. Therefore the scattering can be neglected for many materials. The PVC sample that we used in our experiment has long molecular chains, whose lengths range from 50 to 500 microns [57]. Therefore, the scattering contributes to the total acoustic loss.

For many experiments, the main contribution of the loss and distortion comes from diffraction. The acoustic field can be divided into a near field and a far field. The border of these two fields is located at [48, 58]

$$z_f = d^2 / 4\lambda, \tag{2.32}$$

where $d$ is the size of the laser beam. $\lambda$ is the effective wavelength of the acoustic pulse, and it can be calculated from the sound speed and the center frequency. Before the acoustic signal travels a distance $z_f$, i.e., within the near field, it can be treated as a plane wave. Within this region, the wave shows no attenuation and distortion. When it enters the far field region, it can be considered as a spherical wave confined within a cone with apex angle $2\varepsilon$ given by

$$\varepsilon = \arcsin(d / 2z_f). \tag{2.33}$$

If the detector is located within the far field, it may only sense a portion of the signal if the signal diverges into a region larger than the detection area. The detected signal suffers distortion too, because both the border $z_f$ and the divergent angle $\varepsilon$ are frequency

dependent. The low frequency components attenuate faster than the higher ones, which can be seen from the definitions of $z_f$ and $\varepsilon$ shown in the above equations. For our experiments, the dimension of the light beam is about 1~2mm, and the effective wavelength is typically 0.3mm corresponding a near field limit of 3~10mm. The typical thickness of the sample used in our experiment is 1.5mm. Therefore, at least the first acoustic echo is within the near field, and both the attenuation and the distortion can be neglected.

In this work, the transmission losses are separately treated, since they can be calculated from the impedances of the adjacent media. All other losses are incorporated in an effective attenuation coefficient $\beta$. Since all our acoustic signals have limit bandwidths, as an approximation, $\beta$ is assumed to be a constant, independent of frequency within the signal bandwidth. In addition, the signal travels a distance at millimeter scale before it reaches the detector in most of our experiments. Therefore, the distortion is not obvious. In Chapter III, our theoretical calculation treats the acoustic pulse attenuation without distortion, although in some experiments, we did observe the distortion after the pulse had been reflected several times and traveled a long distance. However, the first echo with least distortion can be used if one needs to analyze the signal profile.

### 2.2.2. Propagation in multiple layers

When a wave propagating in a medium reaches the boundary, reflection and transmission occur if the impedances of the two adjacent mediums are mismatched. The reflected wave now travels in the opposite direction and finally will reach the other end.

Reflection and transmission occur again at the other end due to the same reason. The reflected wave is still within the medium and thus multiple reflections occur at each boundary until the magnitude of the wave dies out. The acoustic signal at any position is the summation of the original and all the reflected waves with proper time delay. It can be formulated as follows.

As illustrated in Fig. 2.6, in general, the impedances of the adjacent mediums are mismatched, i.e., $Z_1 \neq Z_0$ and $Z_1 \neq Z_2$, and all are characteristic impedance of materials. The reflection coefficients for waves traveling within layer 1 at the two boundaries are denoted as $\Gamma_{01}$ and $\Gamma_{21}$. Assume the initial wave is in $+z$ direction in a form of $Ae^{-jk_1 z}$. The wave at any position within layer 1 after sufficient long time (steady state) will be:

$$u(x) = \frac{Ae^{-jk_1 z} + A\Gamma_{21}e^{-jk_1(2L_1 - z)}}{1 - \Gamma_{01}\Gamma_{21}e^{-j2k_1 L_1}} \tag{2.34}$$

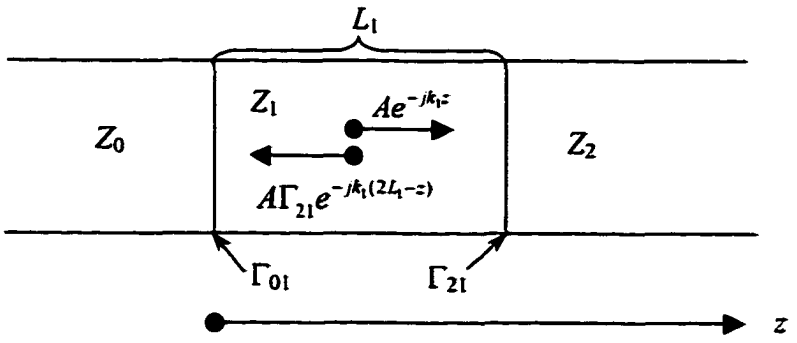


Fig. 2.6. Multi-reflected waves in the middle layer.

Eq. (2.34) can be derived by several methods [59]. It can be interpreted as the summation of a geometry series. The numerator is the original forward wave $Ae^{-jk_1 z}$ plus

the first reflected wave $A\Gamma_{21}e^{-jk_1(2L_1-z)}$ which includes the phase delay. The second term of the denominator is the roundtrip gain that also includes the roundtrip phase delay. Eq. (2.34) holds for a sinusoidal signal with frequency $\omega$.

One can extend the use of Eq. (2.34) to the case where the initial signal is a pulse described as $u(z=0,t)$ by Fourier transform analysis. In that case, one can interpret $A$ as the coefficient of the Fourier transform of the signal, and $k_1=\omega/v_1$, where $v_1$ is wave velocity in layer 1. Both $A$ and $k_1$ are frequency-dependent. The reflection coefficients $\Gamma_{01}$ and $\Gamma_{21}$ could also be frequency-dependent. At any position $z$, all frequency components can be reassembled into a pulse in the time domain using the inverse Fourier transform. In this way, one obtains the time dependent signal at any point in layer 1.

When considering the propagation of an acoustic pulse in a multi-layered structure, it is convenient to formulate the problem in terms of complex impedances and complex reflection coefficients. This allows one to use Eq. (2.34) and Fourier transform methods as mentioned above.

Fig. 2.7 shows an initial wave propagating in the positive $z$ direction from medium 0. A part of the energy will be transmitted into layer 1. At the interfaces between layers 1 and 2, and between layers 1 and 0, multiple reflections occur. Part of each such reflection will be transmitted back into layer 0. The total reflection observed at the interface between layer 0 and layer 1 will be:

$$u_{ref10} = A\Gamma_{10}e^{jk_0z}, \tag{2.35}$$

where $\Gamma_{10}$ is the reflection coefficient for the wave incident to layer 1. Note that $\Gamma_{10}$ contains information about the whole structure to the right of the interface between media 0 and 1, including the thickness of layer 1.

In general, this reflection coefficient is a complex number, which can be obtained from:

$$\Gamma_{10} = \frac{Z_0 - Z_{01}}{Z_0 + Z_{01}}, \tag{2.36}$$

where $Z_0$ is the characteristic impedance of layer 0. $Z_0$ is a real number, and it is the product of density and wave velocity if loss is not considered, i.e., $Z_0=\rho_0 v_0$. $Z_{01}$ is the impedance (looking in the positive $z$ direction) at the interface between layers 0 and 1.

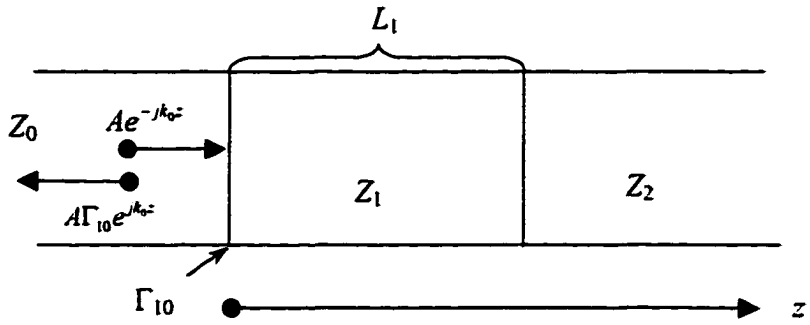


Fig. 2.7. Wave reflection due to multi-layered structure.

Transmission line theory gives [60]:

$$Z_{01} = \frac{Z_{12} - Z_1 \tanh(jk_1L_1)}{Z_1 + Z_{12} \tanh(jk_1L_1)} Z_1, \tag{2.37}$$

where $Z_{12}$ is the impedance at interface between layer 1 and layer 2 and $Z_1$ is the characteristic impedance of layer 1. From Eq. (2.37), one sees that $Z_{01}$ is complex and depends on frequency. In general, $Z_{12}$ is also complex and can be expressed by an expression similar to that for $Z_{01}$. Note that when layer 2 is semi-infinite, then $Z_{12}$ is simply the characteristic impedance of layer 2, namely $Z_2$.

The advantage of using the complex, frequency-dependent reflection coefficient (Eq. (2.35)) is that such a reflection coefficient automatically includes the effects of all multiple reflections from succeeding layers. This is seen as follows: $Z_{01}$ is a function of $Z_{12}$ and $\tanh(jk_1L_1)$. $\tanh(jk_1L_1)$ has information of multi-reflection within layer 1, and $Z_{12}$, dependent on $\tanh(jk_2L_2)$, has information of multi-reflection within layer 2, and so on. By using the complex reflection coefficient each layer can be treated independently, which greatly simplifies the calculation. With the aid of the complex reflection coefficient, one only needs to treat the reflection at the incident interface once, as if it is an interface between two semi-infinite media. This feature makes the processing of multiple reflections neat and simple.

## 2.3. DETECTION OF OA SIGNALS

The piezoelectric transducer nowadays has become the most commonly used detector for optoacoustic signal detection. In order to maximally utilize the sensitivity of this device, the piezoelectric transducer is usually in contact with the sample, so that the acoustic wave can transmit into the detector. It is necessary to investigate the influence of the piezoelectric transducer upon the acoustic signal because, like any other, it is not an ideal linear detector, and hence the voltage output is not proportional to the acoustic signal. The impulse response of a piezoelectric transducer is determined by piezoelectric, electromagnetic and elastic constants of the piezoelectric material, as well as by the geometry of the transducer. In this section, the piezoelectric equations are given first, followed by the introduction of the Mason's model, which is an equivalent electric circuit for a piezoelectric material.

Another commonly used category of ultrasound detection is non-contact optical probing. Although there are many optical probing techniques for OA detection, they all share the same features: non-contact and non-disturbing, which make the completely non-intrusive OA diagnostics possible, wide bandwidth and relative small sensitivity compared with that by the piezoelectric transducers. In this section we will overview several commonly used non-contact detection techniques, followed by the detail of the perpendicular beam refraction method that we used to probe the indirect OA in the surrounding air of the solid sample.

### 2.3.1. Contact detection by a piezoelectric transducer

#### A. Piezoelectricity

A material is said to have piezoelectricity if an electrical field appears in this material when an external force is applied to it and *vice versa*. There are four field variables that can be used to describe a piezoelectric material. Two of them are electrical, namely the electric field strength $E$ [V/m or N/C] and the electrical displacement $D$ [C/m$^2$]; the other two are elastic, namely the dimensionless mechanical strain $S$ and stress $T$ [N/m$^2$]. These variables are related to each other by the electric constants, elastic constants and piezoelectric constants. The relations are described by the piezoelectric equations. For a simple case demonstrated in Fig. 2.8, where $d \ll l$ and $d \ll w$, the one-dimensional piezoelectric equations are [61]:

$$T_3 = c_{33}^D S_3 - h_{33} D_3, \tag{2.38}$$

and

$$E_3 = -h_{33}S_3 + \beta_{33}^S D_3 . \tag{2.39}$$

Here $c_{33}^D$ [N/m$^2$] is the elastic stiffness constant, $\beta_{33}^S$[m/F] is the dielectric impermeability, and $h_{33}$ [V/m] is the piezoelectric displacement constant.

The displacement wave equation for the piezoelectric material is the same as that for a normal acoustic medium which is given by

$$\frac{\partial^2 u_3}{\partial t^2} = \frac{c_{33}^D}{\rho}\frac{\partial^2 u_3}{\partial x_3^2}, \tag{2.40}$$

where $u_3$ is the displacement in $x_3$ direction and $\rho$ is the density.

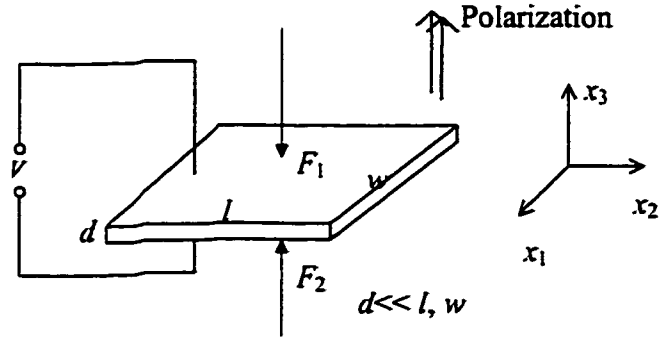


Fig. 2.8. A thin piezoelectric plate in thickness vibration mode.

**B. Mason's model**

Noticing the following facts, relations between the forces acting on the piezoelectric plate and the voltage across the plate were derived by Mason [21].

The voltage across the plate is related to $E$ field by $V = \int_0^d E_3 dx_3$ .

The particle velocities at the two surfaces are $U_1 \equiv \left.\frac{\partial u_3(x_3,t)}{\partial t}\right|_{x_3=0}$ and $-U_2 \equiv \left.\frac{\partial u_3(x_3,t)}{\partial t}\right|_{x_3=d}$ .

The forces at the two surfaces are $F_1 = -lwT_3\big|_{x_3=0}$ and $F_2 = -lwT_3\big|_{x_3=d}$.

The relations derived by Mason are given by

$$F_1 = jZ_0 \tan\frac{\theta}{2}U_1 + (\frac{Z_0}{j\sin\theta} + \frac{1}{j\omega(-C_0/N^2)})(U_1 + U_2) + NV, \tag{2.41}$$

and

$$F_2 = jZ_0 \tan\frac{\theta}{2}U_2 + (\frac{Z_0}{j\sin\theta} + \frac{1}{j\omega(-C_0/N^2)})(U_1 + U_2) + NV. \tag{2.42}$$

Here $Z_0 \equiv lw(\rho v_D)$ is the acoustic impedance, $C_0 \equiv \frac{lw}{\beta_{33}^S d}$ is the capacity of the plate, and $N \equiv \frac{F}{V}\Big|_{\substack{U_1=0 \\ U_2=0}} = C_0 h_{33}$ is a coupling coefficient for force and voltage. The phase is defined as $\theta \equiv \frac{\omega d}{v_D}$, where $v_D$ is the acoustic wave velocity and $\omega$ is the acoustic frequency.

The coupling between the voltage and the force described by Eqs. (2.41) and (2.42) can be graphically represented by an electronic circuit, which is shown in Fig. 2.9. Note that the term $jZ_0 \tan\frac{\theta}{2}$ describes an inductive behavior, while the term $Z_0 / j\sin\theta$ is equivalent to a capacitor. Therefore, the circuit in Fig. 2.9 can be slightly modified to convert to a transmission line model [62], which allows one to conveniently simulate this equivalent circuit using the PSPICE software [63]. The PSPICE circuit will be described in Chapter III where we model the optoacoustic wave propagation and detection.

If one only needs to investigate the relation of the displacement and the voltage, a simple expression can be derived for the open circuit case:

$$V = -h_{33}(u_3|_{x_3=d} - u_3|_{x_3=0}). \tag{2.43}$$

The above equation shows that the open circuit voltage is proportional to the displacement difference between the two surfaces of the plate. The piezoelectric displacement constant $h_{33}$ is normally a large number on the order of $10^9$ V/m; thus, the piezoelectric transducer has very high sensitivity in detection of small displacement. Eq. (2.43) was used in another method that we developed to theoretically calculate the optoacoustic experiment by combining the analytical solution to the wave equation and the Fourier transform technique. This work will also be discussed in Chapter III.

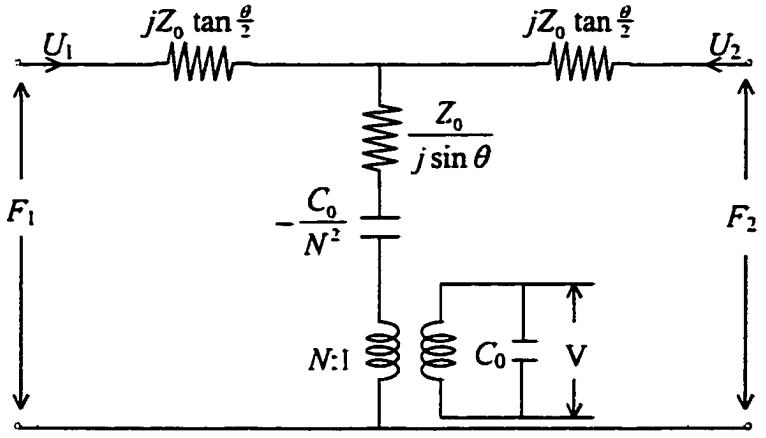


Fig. 2.9. Mason's equivalent circuit for a piezoelectric plate.

### 2.3.2. Non-contact detection by an optical probe beam

#### A. Overview of techniques for non-contact detection

For non-contact ultrasound detection, a laser probe beam is usually used to monitor a certain change caused by the acoustic signal in the solid sample. Such changes include

surface deformation, surface displacement and variation of index of refraction in the solid or in the coupling fluid.

The acoustic wave propagating in the sample will cause surface motion when it arrives at the surface. The displacement is usually detected by the interferometry method. The interferometer is a very sensitive instrument for detecting a small difference in the optical path lengths between a probe and a reference beam which propagate in two arms of the interferometer. When the acoustic wave arrives at the surface where the probe beam is incident, the surface is distorted slightly by the pressure of an acoustic signal. The displacement will cause a change in optical path length of the probe beam and, therefore, an interference pattern will be generated when combining with the probe and the reference beam. The advantage of an interferometer is that it does not require a super smooth and highly reflected surface, although such a surface helps to improve the signal-to-noise ratio. However, it is sensitive to vibrations and thus requires a highly stable environment. The detection sensitivity can reach $10^{-7}\text{nm}(\text{WSr/Hz})^{1/2}$ [64].

Instead of probing the displacement, the beam deflection method can be used to detect the slope of the surface deformation. The deflection angle is approximately twice that of the slope. Therefore, the incident probe-beam should be aligned to the maximum slope. A long distance from the reflection site to the detection plane (where the photo detector is located) may help to increase the displacement of the laser spot in the detection plane, hence, helping to increase the signal-to-noise ratio. However, there is a tradeoff between this displacement and probe beam diffraction. The advantage of this method is that it is insensitive to vibrations and easier to implement. It usually requires a

polished surface and is thus suitable for use with semiconductor samples. The sensitivity can be $10^{-7}$ nm$(W/Hz)^{1/2}$ [64], which is similar to that of the interferometer.

The index of refraction of a medium is modulated by the acoustic propagating in it through modulation of the density. If a probe beam passes through this modulated region, the beam will change its direction. The same detection scheme for the beam deflection can be used for the detection of this refracted probe beam. This method is called beam refraction in order to tell from the beam deflection caused by surface slope.

To perform beam refraction, the probe beam must be able to pass through the sample without too much attenuation, because the photo detector is placed outside the sample. The probe beam can be either parallel or perpendicular to the pump beam [65]. The detection of beam refraction can utilize either a position sensor or a knife-edge and a photodiode. A position sensor directly measures the displacement of the laser spot on the detection plane. For example, the resolution of a two-dimensional position sensor (Hamamatsu S2044) can reach 2.5 μm. However, the rise time is as much as 0.3μs, which is too slow for our nanosecond ultrasonic signals. If the reflected probe beam can be partly blocked by a knife-edge, then the light power falling onto the detected surface will change when the beam is deflected. In this case, a single photodiode can be used to detect the intensity change. In our experiment, a photodiode made by Thorlabs (DET200) is used. Its 1ns rise time is short enough for our optoacoustic signals.

Recently, the perpendicular beam refraction has been used to probe the OA signal transmitted to air from the solid sample by Caron and coworkers [30, 31]. They named this method "gas-coupled laser acoustic detection" (GCLAD). In this method, the probe beam does not need to penetrate into the solid sample. Neither does it need to be reflected

by the surface. Therefore, most lasers can be used as a probe and there is no polish requirement for the sample surface. However, since air is not a good coupling fluid for most solids, the portion of acoustic energy transmitted into air is very small. In order to get a satisfied signal-to-noise ratio, it is required that the OA signal in the solid sample is strong enough [31]. We have successfully used the off-sample perpendicular beam refraction technique to probe the indirect OA signal due to the thermal expansion in air. Since the efficiency of indirect OA generation is relatively higher than the transmission from the solid, the intensity requirement for the pump laser reduces. More details of this method are discussed in the next section.

For all non-contact detection techniques, a continuous probe laser is usually required. A pulsed laser theoretically can also be used and has its own advantages. However, it is only applicable when the OA pulse is very narrow such as in picosecond scale. Longer delay of the probe pulse is required if the acoustic pulse is wider, or if more than one echo is needed. This will require a complicated system for optical pulse delaying, if it is not impossible.

### B. Off-sample perpendicular probe beam refraction

Fig. 2.10 is the schematic for the off-sample perpendicular probe beam refraction. The probe beam is parallel to the sample surface and perpendicular to the pump beam. It is off the surface with a distance $x$. The pressure signal in the surrounding air causes variation of the index of refraction, which results in a beam deflection with an angle $\delta$. If a knife-edge is used to block part of the probe beam, then a photodiode can be used to

detect the variation of light intensity. Otherwise, a position sensor is needed to directly detect the displacement at the detection plane.

If the pressure $\Delta p$ in the surrounding air is known, the corresponding change of the index of refraction is given by [31]

$$\Delta n = (n_0 - 1)\Delta p(x)/(\rho c_a^2), \tag{2.44}$$

where $n_0$ is the ambient index of refraction, $\rho$ and $c_a$ are the density and sound velocity of air respectively.

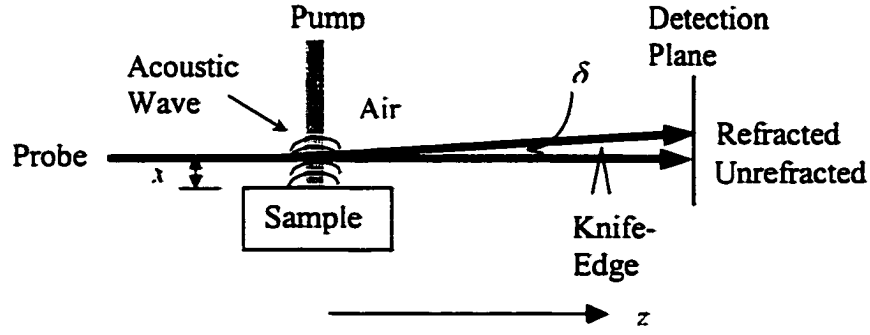


Fig. 2.10. Schematic of off-sample perpendicular probe beam refraction for the detection of indirect OA signal due to the thermal expansion in the surrounding air. If a knife-edge is used to block part of the probe beam, a photodiode can be used to detect the deflection. Otherwise, a position sensor should be used.

The deflection angle is given by [31, 65]

$$\delta = \frac{-1}{n_0 c_a}\int_{-b}^{b}\frac{\partial n}{\partial t}dz, \tag{2.45}$$

where $2b$ is the width of the acoustic field through which the probe beam passes.

From Eqs. (2.44) and (2.45), one can see that the profile of the detected signal by the beam refraction method is the time derivative of the pressure signal if the time derivative of the index of refraction is assumed to be unchanged along $z$ direction.

For a knife-edge beam deflection experiment, maximizing the signal-to-noise ratio is a very important issue since the observed signal is a very weak AC voltage superimposed upon a large DC bias. Any noise will decrease the detection sensitivity. The noise has the following components: environmental noise, laser-intensity fluctuation, laser-pointing instability, electric circuit thermal noise and detector shot noise. The highest frequency of the first three types of noise is usually lower than 50kHz [66]. Since our signals are short pulses in nanosecond scale, these three types of low frequency noise do not need to be taken into consideration. Only the thermal noise and the shot noise are important, since they are wide band.

The thermal noise power is [64]

$$\bar{i}_{th}^2 = \frac{4kT}{R}\Delta f, \tag{2.46}$$

where $\Delta f$ is the bandwidth of the signal, $T$ is the temperature and $R$ is the load impedance.

The shot-noise power is

$$\bar{i}_s^2 = 2e^2\eta\frac{P_d}{\hbar\omega}\Delta f, \tag{2.47}$$

where $\eta$ is the quantum efficiency, $\hbar\omega$ is the photon energy of the probe laser, $e$ is the electron charge and $P_d$ is the probe power falling onto the photodiode.

The signal photocurrent ($i_d$) is proportional to the change of power of the probe laser ($\Delta P_d$) that the photodiode receives due to beam deflection:

$$i_d = \Delta P_d \eta e/(\hbar\omega). \tag{2.48}$$

$\Delta P_d$ is proportional to the power of the probe laser.

Therefore the signal to noise ratio can be expressed as:

$$\left(\frac{S}{N}\right) = \frac{i_d}{\sqrt{\overline{i_{th}^2} + \overline{i_s^2}}} = \frac{\Delta P_d \eta e/(\hbar\omega)}{\sqrt{\frac{4kT}{R}\Delta f + 2e^2\eta\frac{P_d}{\hbar\omega}\Delta f}}. \tag{2.49}$$

Eq. (2.47) shows that the shot noise power is proportional to the light power that the photodiode receives, and hence, to the power of probe laser. Decreasing the laser power will help to reduce the shot noise power. However, the signal photocurrent is directly proportional to the laser power as seen from Eq. (2.48). Hence, the overall effect is that increasing the laser power increases the signal to noise ratio. Therefore, in a beam refraction experiment, one should seek to use a high power probe laser.

# CHAPTER III

# THEORETICAL CALCULATION OF PULSED OPTOACOUSTIC SIGNALS

This chapter presents the theoretical treatment of a one-dimensional pulsed OA signal. From the basic generation theory introduced in the previous chapter, we know that the acoustic signal is initiated in the absorption region. This signal can be modeled by the convolution of the profile of the laser pulse and the impulse response, which is determined by the optical absorption coefficient at the laser wavelength and the boundary condition at the end where the laser is incident. However, the profile of the electrical signal one finally obtains, either by a piezoelectric transducer or a probe beam, is different from that of the initial acoustic signal due to the following reasons. First, each detection scheme imposes its own transfer function on the signal and, often, the transfer function is non-linear. Second, the acoustic signal is usually picked up at a site distant from the laser interaction region. Therefore, the signal generally experiences some distortion before reaching the detector. Finally, additional echoes of the original acoustic pulse may appear due to the multiple reflections at the boundaries.

This chapter presents two methods for calculating the propagating acoustic pulse profile in multi-layered media, including the evaluation of the system response of a wideband piezoelectric detector. This is followed by the evaluation of the response of a detection scheme involving the deflection of an optical probe beam. In the latter

technique, which is completely non-intrusive, the beam probes the indirect OA signal generated by the irradiated solid sample.

## 3.1. CONTACT DETECTION OF PULSED OA SIGNAL FROM A SOLID SAMPLE

In an experiment described in detail in the next chapter, the laser pulses were incident on the front end of a solid sample which has a piezoelectric transducer in good acoustic contact with the back of the sample. The sample can be a single solid or have multiple layers. In this section, we calculate the signal given by the transducer, assuming that the initial acoustic pulse is known. Note that the acoustic pulse details can be calculated as discussed in Chapter II.

An acoustic medium can be modeled in a manner analogous to an electrical transmission line. A piezoelectric transducer can also be similarly represented by a transmission line which is modified by the addition of an electrical-to-mechanical energy transformer. A big advantage of this approach is that it allows one to use electrical circuit theoretical formulation, and enables one to take advantage of any software, such as PSPICE, which is commercially available and dedicated solely to circuit analysis. We refer to this technique as the Equivalent Electrical Circuit (EEC) Method.

Another approach to the same analysis utilizes the principles of the Fourier transform theory. Here, a sinusoidal solution to the wave equation for an acoustic medium is first obtained. The initial acoustic pulse is then decomposed into its harmonic components and reassembled at the detection site by a fast Fourier transform algorithm. We call this method FFT method.

At the end of this section, we compare these two methods with a third one, which solves the relevant partial differential equations (PDE) numerically [67]. It is shown that all three methods yield identical results.

### 3.1.1. The equivalent electrical circuit model

In Chapter II, we summarized Mason's model, which is an electric circuit representation for an ultrasonic transducer. The analytical solution for Mason's model can be obtained, for instance, by using the Laplace transform method. However, since only a few standard functions such as step function, rectangle function and ramp function, have analytical Laplace transforms, only limited inputs with such standard functions have such analytical solutions [62]. While the analytical method helps us to understand the model and the behavior of a transducer, such a method is not practical for a real experiment. In that case, a numerical method, such as those utilizing the Z transform, can be employed. The Z transform is the discrete form of the Laplace transform, and it has been incorporated to the numerical solutions for Mason's model and has yielded results consistent with experimental ones [68]. Several other methods for modeling and predicting the system response can be found in the references given in Hayward's paper [68].

Mason's model can be further modified, by replacing the capacitive and inductive components in the model with a transmission line [62, 63, 69]. This has the advantage of allowing a PSPICE simulation to be done conveniently. In addition, the sample itself can be considered as a transmission line with the following mapping relations: $\rho \equiv \mu \equiv L$; $c_{33}^{-1} \equiv \varepsilon \equiv C$; $F \equiv V$; $u \equiv I$ (see Appendix A). The whole system therefore can be modeled by

cascading several transmission lines. PSPICE is then set up to analyze this combination of transmission lines. The program can also be used to account for the reflection and refraction of the acoustic signal at the various interfaces that it encounters.

There are several unique features in this transmission-line model for simulating the piezoelectric transducer by PSPICE. First, there is a negative capacitance in Mason's model. Although the negative capacitor is not in PSPICE's library as a standard component, it can be modeled as the circuit illustrated in Fig. 3.1 [63]. Here $C_0$ is the absolute value of the negative capacitor. The selection of the value of the reference capacitor $C_s$ is random, but it determines the gain ($\beta$) of the current-controlled current source. The relation of the current and the voltage is given by:

$$I_c = (1+\beta) j\omega C_s V_c . \tag{3.1}$$

From the above equation, one can see that the value of $\beta$ should be set to $-(1+C_0/C_s)$ in order to model the capacitance $-C_0$.

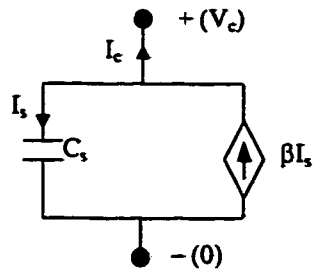


Fig. 3.1. Representation of negative capacitance in PSPICE. $C_0$ is the absolute value of the negative capacitance. $\beta$ is the gain of the current-controlled current source and $\beta = -(1+C_0/C_s)$.

Second, in Mason's model there is an ideal electrical-to-mechanical energy transformer. To guarantee energy conservation between the primary and the secondary coils, this ideal transform can be modeled by a voltage-controlled voltage source and a current-controlled current source [63] (see E1 and F2 in Fig. 3.2).

**A. Modeling the piezoelectric transducer as a transmitter**

A piezoelectric transducer normally has at least two layers: an active element and a backing medium. Piezoelectric ceramic (PZT), quartz or PDFV film can be used as the active material that converts between the electrical and mechanical signals. The sample is usually placed in front of the active element with good contact. A thin wear plate and/or acoustic conducting materials sometimes can also be placed between the active element and the sample. Fig. 3.2 is the complete PSPICE schematic for a transmission-line model of a simple experiment that utilizes a piezoelectric transducer as the acoustic transmitter. The piezoelectric material (PZT) has a backing layer and the sample is placed in contact with the other surface of the PZT. A voltage signal is applied to the PZT as a driving source. The PSPICE schematic is used to model the pressure signal launched into the sample. The upper part of the schematic is the mechanical portion. The transmission line $T_1$ represents the piezoelectric material. $R_b$ is equivalent to the acoustic impedance of the backing material, and $R_f$ is the impedance of the sample. The voltage across resistor $R_b$ represents the force (or pressure) launched into the sample. The voltage-controlled voltage source $E_1$ and current-controlled current source $F_2$ form the ideal electrical-to-mechanical transformer. The lower-right part is the electrical portion of the transducer. The current controlled-current source $F_1$ and capacitor $C_s$ form the negative capacitance.

The capacitor $C_0$ is the intrinsic capacitance of the transducer. Voltage source $V_1$ is the electrical driving source.

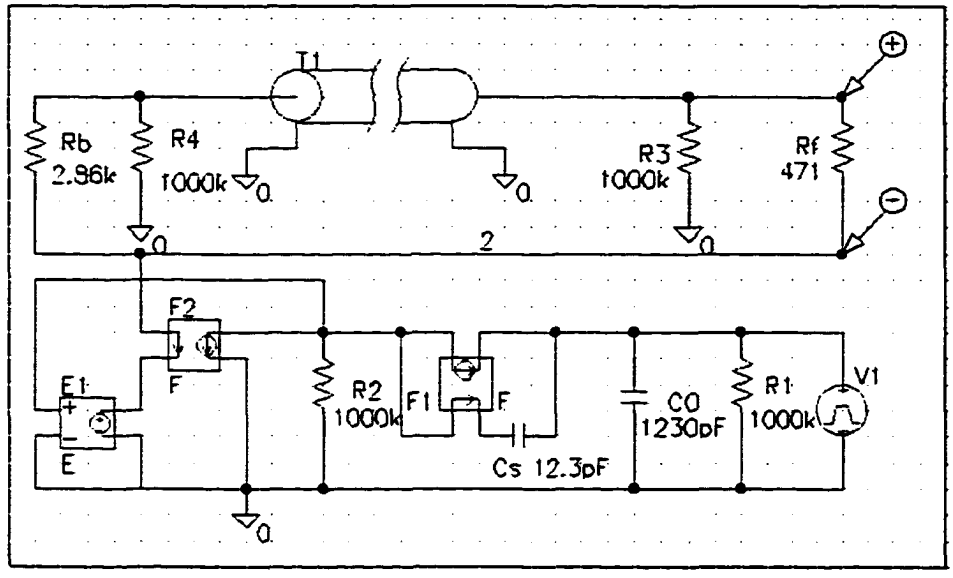


Fig. 3.2. PSPICE schematic of the transmission-line model for a piezoelectric transducer as a transmitter. The upper part is the mechanical portion, the lower-left part is the electrical-to-mechanical energy transformer and the lower-right part is the electrical portion. Voltage source $V_1$ is the electrical driving source, and the voltage across resistor $R_f$ represents the transmitted force.

Hayward successfully modeled the stress signal generated by a piezoelectric transducer driven by a negative voltage spike using z-transform method [68]. The theoretical result was in good agreement with the experimental one. Then Morris was able to reproduce Hayward's result using the circuit theory and a SPICE simulation [63]. Our PSPICE model Fig. 3.2 is modified from Morris's SPICE model. In order to verify the accuracy of this PSPICE model, we took the same values for all components that were used by Morris, and successfully reproduced Morris's result. The voltage across $R_f$, which equivalently is the stress launched into the sample by the piezoelectric transducer, is shown in Fig. 3.3.

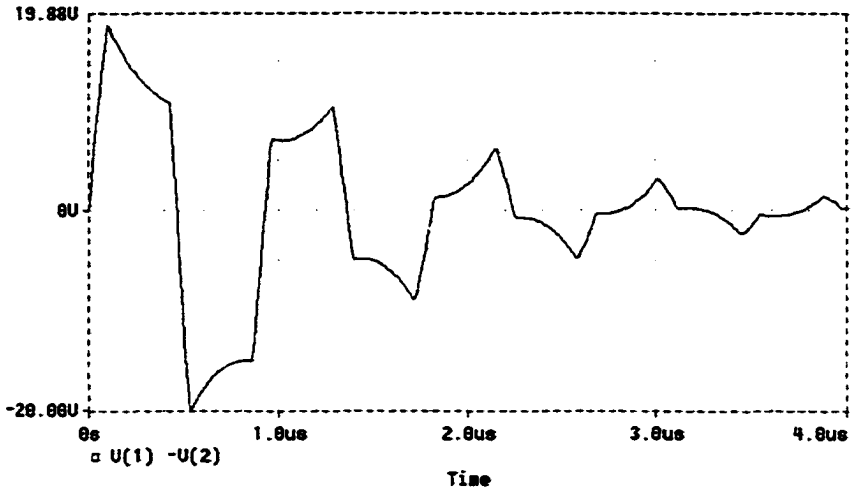


Fig. 3.3. PSPICE output from the schematic shown in Fig. 3.2.

## B. Modeling the piezoelectric transducer as a receiver

In our OA experiments, we used the piezoelectric transducer to detect the acoustic signal and obtain a voltage signal. We modified the schematic shown in Fig. 3.2 and made it suitable for modeling the transducer as a receiver. The new schematic is shown in Fig. 3.4. $V_1$ is a voltage source simulating the stress wave in the sample. $R_f$ is the acoustic impedance of the sample. Note that the sample impedance is in series with the voltage source, instead of parallel to it. The large value of $R_0$ represents open circuit.

Using the schematic of Fig. 3.4, we simulated the step response of the transducer as a receiver. Fig. 3.5 is the computed output for the voltage across the transducer under conditions that (1) the acoustic impedance of the transducer is twice of that of the sample; (2) the backing is air ($R_b \approx 0$); (3) the delay time at the transducer is 100ns. This result agrees with the analytical solution [62].

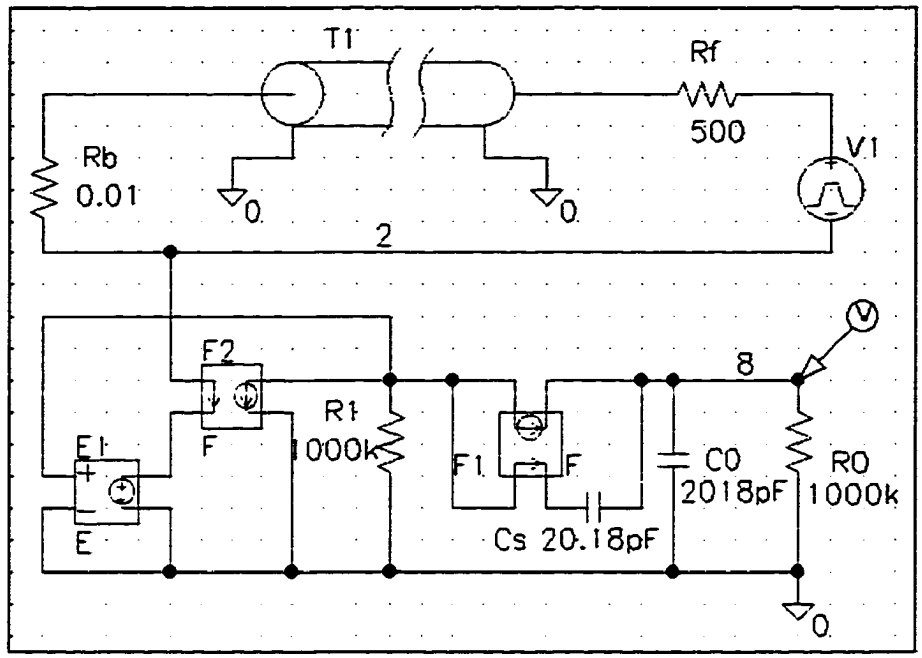


Fig. 3.4. Schematic for modeling a piezoelectric transducer as an acoustic receiver. It is modified from Fig. 3.2.

## C. Modeling the properties of the Panametrics transducer used in our experiments

After we have tested the PSPICE model for the transducer, either as a transmitter or as a receiver, we are almost ready to model a real experiment except for one problem. The piezoelectric transducer that we used in our experiment is a commercial product from Panamatrics Inc. We know the structure of a typical Panamatrics ultrasonic transducer (Fig. 3.6) from the company's technical notes [70]. However, we do not have any parameters of the transducer that are needed in the simulation except that the spectrum of the response was given. According to the testing sheet from the manufacturer, this response spectrum is obtained by launching an acoustic signal into a one-inch long silica by the transducer driven by a negative voltage impulse (spike), and then detecting the acoustic echo using the same transducer as a receiver.

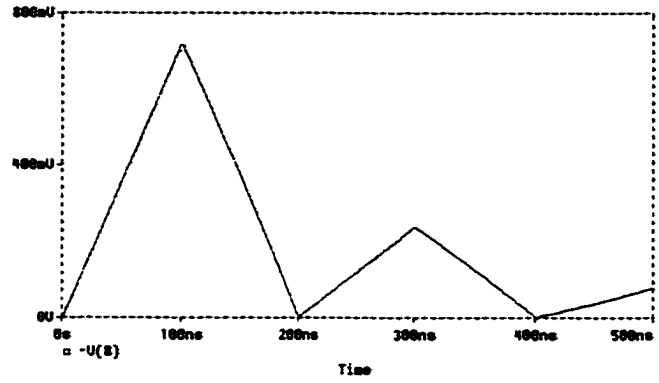


Fig. 3.5. PSPICE output of the voltage across the transducer in response to a step stress driving signal. It is assumed that the impedance of the transmission line is twice the impedance of the sample and the backing is air.

Our goal here is to obtain all parameters required by the PSPICE model as accurately as possible to the real product. This is achieved by simulating the testing experiment described above with selected parameters. Initially we used the typical parameters for PZT materials. Then we compared the simulation result with the spectrum given by the manufacturer and fine-tuned the parameters until these two results reasonably agreed one another.

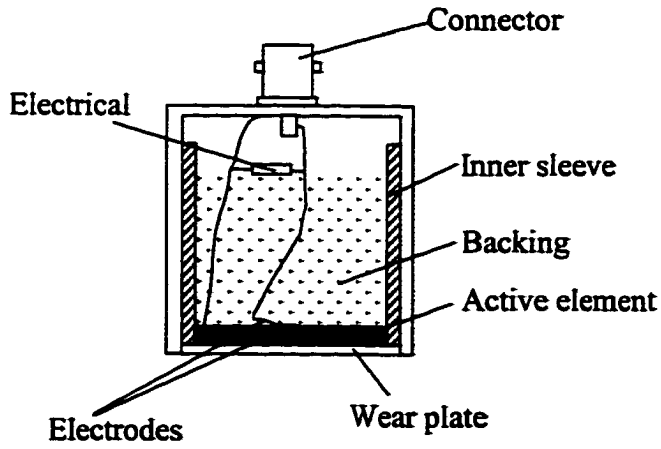


Fig. 3.6. Structure of a typical Panametrics ultrasonic transducer.

Fig. 3.7 is the schematic used to model the testing experiment described above. Although in this experiment the same transducer was used to launch and detect the acoustic signal, we used two separate transmission lines (with same specifications) to model them respectively. The transmission line, T1, and its auxiliary circuit is used to model the transmitter, and T2 and its auxiliary circuit work as the receiver. The silica sample is represented by the transmission line, T3. It is connected to the transmitter by an ideal transformer (E3, F5) and to the receiver by another ideal transformer (E4, F6). The effect of the wear plate is neglected since it is very thin. A negative spike voltage (V3) is applied to the transmitter. The voltage across the load resistor, $R_L$, is the output from the receiver. In order to match the transducer's responsivity to the one given by the manufacturer, two parameters in schematic Fig. 3.7 can be adjusted, namely the delay time of T1 (T2) and the acoustic impedance of the backing material, Rb (Rb2). This delay time, which corresponds to the center of the responsivity spectrum, is determined by the thickness of the piezoelectric element. Impedance Rb determines the width of the spectrum. The backing material absorbs all acoustic signal transmitted into it. Therefore, we can simply use a resistor to simulate it.

Fig. 3.8 is the calculated responsivity of the Panametrics transducer using the circuit shown in Fig. 3.7 and the comparison with the data provided by the manufacturer. Most parameters used to obtain the blue trace have been labeled in Fig. 3.7 except for impedance Z(T1, T2) = 782.7Ω, delay Td(T1,T2) = 26.5ns, impedance Z(T3) = 237.65Ω, delay Td(T3) = 4.252μs, gain β(E1,F2,E2,F4) = 2.4. All these values are based on the published data from [61, 71] and the sensitive area of the transducer which is $1.8\times10^{-5}m^2$,

except Rb and Td (T1, T2), which are adjusted to best simulate the behavior of the transducer.

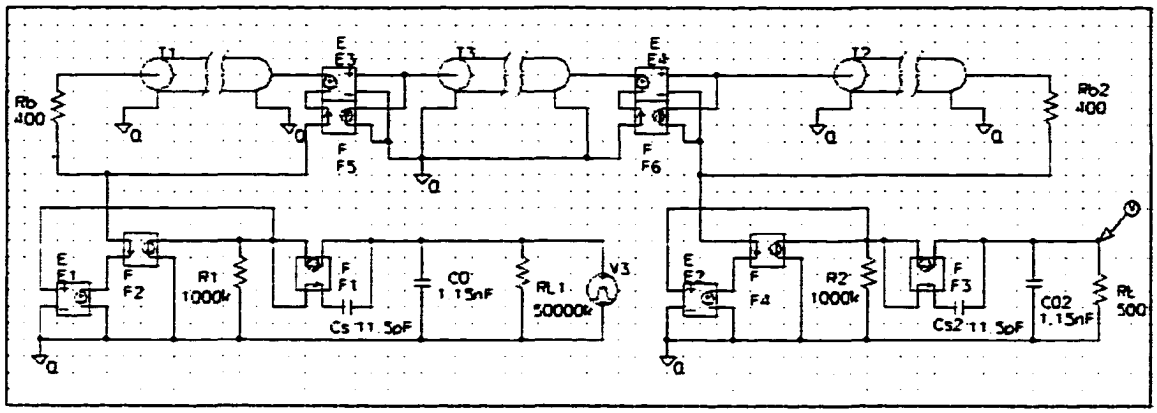


Fig. 3.7. Schematic used to model the testing experiment for the Panametrics transducer. A negative spike voltage (V3) is applied to the transducer (T1 as a transmitter). The generated ultrasound propagates through the silica sample (T3) and then is detected by the same transducer (T2 as a receiver).

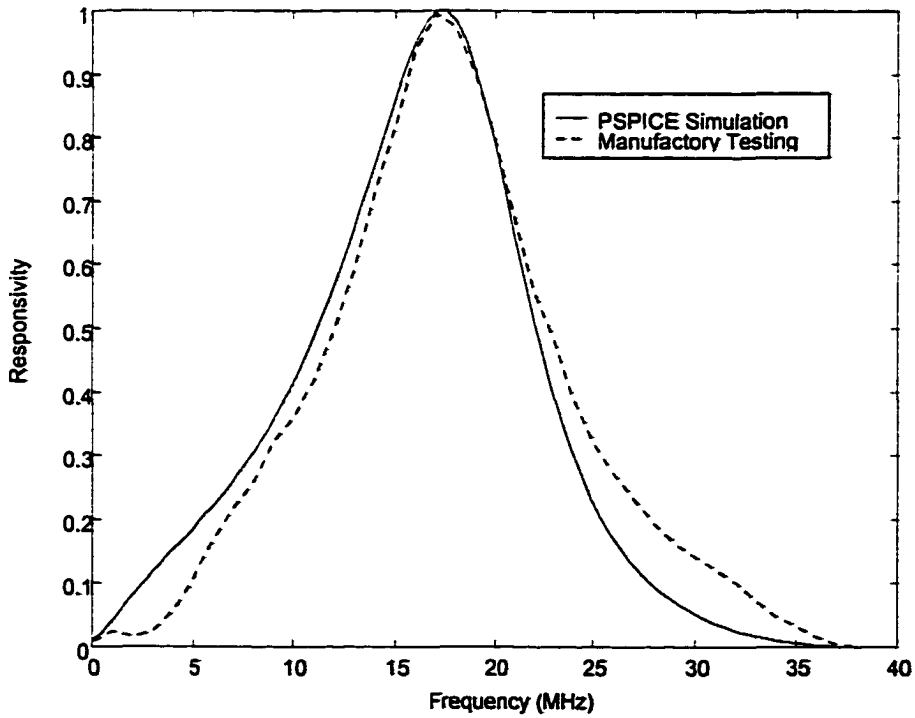


Fig. 3.8. Responsivity of the panametrics transducer by the simulation (solid) and the comparison with the data provided by the manufacturer (dashed). The simulation result is the normalized frequency spectrum of the voltage signal across resistor $R_L$ in Fig. 3.7.

### D. Modeling the optoacoustic experiment

After getting the property parameters of the Panametrics transducer, we are now ready to model the optoacoustic experiment using the EEC method. Fig. 3.9 is the schematic of such a circuit. Voltage source V1 provides the acoustic pressure signal in the sample (T3). The EEC method cannot model the generation of an OA signal. Therefore, the pressure data needs to be provided through a disk file generated by other methods. T2 and its auxiliary circuit model the transducer. The output of the transducer is taken from voltage across the loading resistor, $R_L$. One result from this circuit is presented in 3.1.3, where results from different methods are compared.

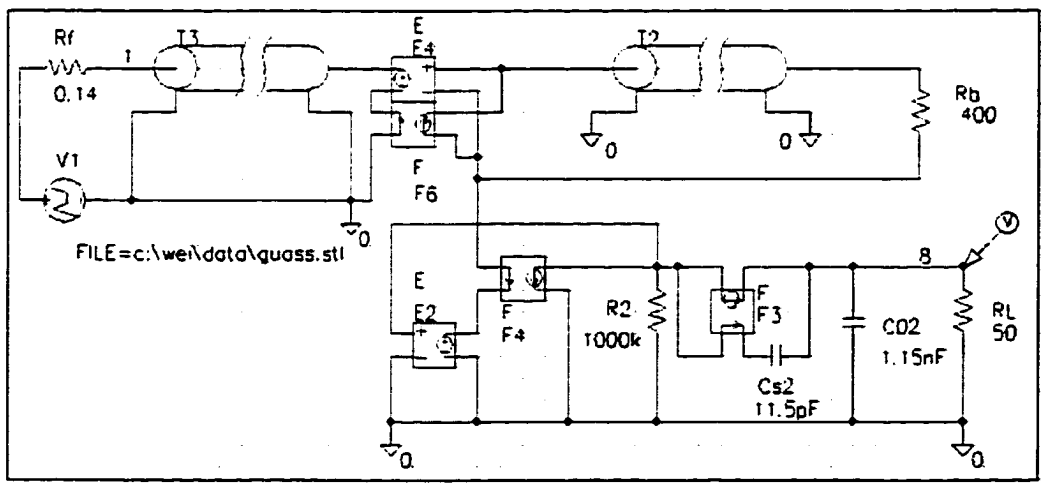


Fig. 3.9. The PSPICE schematic used to simulate an optoacoustic experiment.

### 3.1.2. The fast Fourier transform model

The FFT model is the method we independently developed to calculate the OA signal read from a piezoelectric transducer. This is a technique that combines the sinusoidal

solution to the wave equation for acoustic media and the Fourier transform. First, we apply the propagation theory of an acoustic wave in multiple layers that has been discussed in Chapter II. Then we calculate the voltage signal from the acoustic detector using Mason's theory for the piezoelectric transducer. We use FFT and inverse FFT techniques to decompose the initial acoustic pulse into harmonic components and synthesize the corresponding voltage harmonics into a pulse. Theoretically, this method is an analytical approach to the problem, but it can accept any initial condition by using the Fourier transform technique. Therefore, it is very applicable to problems.

Consider an optoacoustic experiment such as that illustrated in Fig. 3.10. A pulsed laser beam shines normally on the front face of a sample with thickness $L_1$. A pressure contact is made between a piezoelectric transducer and the back end of the sample. The structure of the transducer has been described previously. There is a thin wear plate in front of the PZT layer and a backing layer to absorb leaked acoustic waves from the PZT layer. Since the backing is highly absorptive for acoustic waves and there will be no reflected waves existing in this layer, the backing can be treated as a semi-infinite acoustic medium. Further, since the wear plate is thin, its influence on the experiment can be neglected and thus it is not shown in Fig. 3.10.

For the convenience of calculating the response of the piezoelectric transducer, we use displacement to represent the optoacoustic signal. The initial displacement signal can be converted from the pressure signal calculated from the generation theory presented in Chapter II. Then the displacement at any layer in Fig. 3.10 can be calculated using Eq. (2.34) in Section 2.2.2 of Chapter II, where the theory of the acoustic wave propagation is discussed.

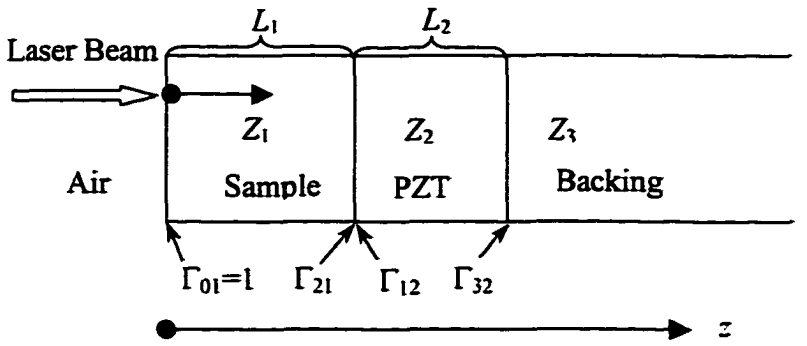


Fig. 3.10. Multi-layered structure for modeling an optoacoustic experiment.

**A. Displacement signal at each layer**

Let $U_0(\omega)$ be the Fourier transform of $u_0(t)$, the signal originating at the surface which is exposed to the laser pulse ($z$=0). One needs to calculate $U(\omega, z)$ in terms of $U_0(\omega)$. The signal registered on the piezoelectric detector can be obtained from $U(\omega, z)$ by recognizing that the open circuit voltage across the piezoelectric transducer is the difference of displacements at two faces of the transducer. Hence, one needs to solve for the displacement at $z=L_1$ and $z=L_1+L_2$, where $L_2$ is the thickness of the detector.

In order to calculate the displacement at any point in space, for all time, with the help of Eq. (2.34), one needs the relevant complex impedances and reflection coefficients which are evaluated as follows.

The impedance at $z=L_1+L_2$ is simply the characteristic impedance of the backing material since it can be treated as a semi-infinite layer. Therefore one gets $Z_{23}=Z_3$, where $Z_3$ is the characteristic impedance of the backing material.

The displacement reflection coefficient for waves incident to the boundary from the transducer is

$$\Gamma_{32} = \frac{Z_2 - Z_{23}}{Z_2 + Z_{23}}, \tag{3.2}$$

where $Z_2$ is the characteristic impedance of the material from which the pulse is incident.

The impedance at $z = L_1$ can be calculated by Eq. (2.37) and is

$$Z_{12} = \frac{Z_{23} - Z_2 \tanh(jk_2L_2)}{Z_2 + Z_{23} \tanh(jk_2L_2)} Z_2. \tag{3.3}$$

The displacement reflection coefficient for waves incident to the boundary from the sample is

$$\Gamma_{21} = \frac{Z_1 - Z_{12}}{Z_1 + Z_{12}}, \tag{3.4}$$

where $Z_1$ is the characteristic impedance of the sample. (Note that, in general, $\Gamma_{ij}$ is not equal to $-\Gamma_{ji}$.).

At $z = 0$, the displacement reflection coefficient can be set to unity for all frequency components since $\Gamma_{01} = \frac{Z_1 - Z_0}{Z_1 + Z_0}$ and $Z_0$ can be approximated to zero since $Z = \rho v$ and $\rho$, the density of air, can be neglected in comparison to the density of the solid sample. Hence, $\Gamma_{01} = 1$.

Now one is able to solve the displacement at $z = L_1$ and $z = L_1 + L_2$. In the sample layer, $U_0(\omega)$ is the original wave starting at $z = 0$. Substituting $z = L_1$ into Eq. (2.34) results in:

$$U(\omega, z = L_1^-) = \frac{(1 + \Gamma_{21})U_0(\omega)e^{-jk_1L_1}}{1 - \Gamma_{01}\Gamma_{21}e^{-j2k_1L_1}}, \tag{3.5}$$

where $k_1 = \omega / v_1$. Eq. (3.5) calculates the displacement at $z = L_1^-$, i.e., the left side of the interface between layers 1 and 2.

We also apply Eq. (2.34) to the transducer layer to obtain the displacements at $z = L_1^+$ and $z = L_1 + L_2$, i.e.,

$$U(\omega, z = L_1^+) = \frac{U_{02} + U_{02}\Gamma_{32}e^{-j2k_2L_2}}{1 - \Gamma_{12}\Gamma_{32}e^{-j2k_2L_2}}, \tag{3.6}$$

and

$$U(\omega, z = L_1 + L_2) = \frac{(1 + \Gamma_{32})U_{02}(\omega)e^{-jk_2L_2}}{1 - \Gamma_{12}\Gamma_{32}e^{-j2k_2L_2}}. \tag{3.7}$$

Dividing Eq. (3.7) by Eq. (3.6)(11) and rearranging slightly, one gets

$$U(\omega, z = L_1 + L_2) = \frac{(1 + \Gamma_{32})e^{-jk_2L_2}}{1 + \Gamma_{32}e^{-j2k_2L_2}} \cdot U(\omega, z = L_1^+). \tag{3.8}$$

Because of displacement continuity at the interface, $U(\omega, z = L_1^-) = U(\omega, z = L_1^+)$, the displacement at $z = L_1 + L_2$ can be obtained by substituting Eq. (3.5) into Eq. (3.8). In the same manner, the displacement can be derived at each boundary no matter how many layers the structure has.

**B. Voltage signal produced by the piezoelectric transducer**

To get open circuit voltage, an inverse Fourier transform should be applied to the displacement at $z = L_1$ and $z = L_1 + L_2$. The voltage is proportional to the difference in these displacements:

$$V_{open} = h_{33} \cdot (u(t, z = L_1) - u(t, z = L_1 + L_2)), \tag{3.9}$$

where $h_{33}$ is the piezoelectric constant of the transducer material.

Since in the experiment the transducer is connected to a preamplifier, one needs to account for the loading presented by the latter. The load resistance parallel with the internal resistance of the transducer forms an effective high pass filter when the internal capacitance is also accounted for.

The transducer capacitance is

$$C_0 = \frac{\varepsilon_0 \varepsilon_r \pi r_2^2}{L_2}, \tag{3.10}$$

where $\varepsilon_r$ is the relative permittivity of PZT and $r_2$ is the radius of the transducer. Let $R$ be the shunt resistance of the inner resistance of the transducer and the input impedance of the preamplifier. The transfer function of this RC high pass filter is:

$$H_{hp}(\omega) = \frac{j\omega RC_0}{1 + j\omega RC_0}. \tag{3.11}$$

Hence, the measured signal voltage can be calculated from the following inverse Fourier transform:

$$V = h_{33} \cdot \mathrm{F}^{-1}\{[U(\omega, x = L_1) - U(\omega, x = L_1 + L_2)] \cdot H_{hp}(\omega)\}. \tag{3.12}$$

### C. Incorporation of acoustic losses in the model

Note that the discussion above holds for materials that are lossless, as well as those which have acoustic losses. In the latter case, one uses the complex acoustic characteristic impedance, which leads to a complex propagation constant.

In general, then, $k$ is a complex variable:

$$k = k_R + jk_I. \tag{3.13}$$

The real part is defined as usual:

$$k_R = \omega / v. \tag{3.14}$$

The imaginary part, $k_I$, accounts for attenuation and is often called attenuation coefficient $\beta$ which has unit of Nepers/meter. In our calculation, we use the unit of inverse meter. As discussed in Chapter II, there are several mechanisms that lead to acoustic attenuation. Here $\beta$ is an effective attenuation coefficient that accounts for all losses. $\beta$ is generally frequency dependent. Here we assume it is a constant in the frequency region of our OA signal as an approximation.

For a lossy acoustic medium the complex characteristic impedance is [72]:

$$Z = \frac{\rho v}{1 + j\beta / k_R}. \tag{3.15}$$

### 3.1.3. Comparison of all three methods

In this section, results of computations for the acoustic signals, based on the two models discussed above, are given. They are compared to the third method, which implements the numerical solution to the relevant partial differential equations and is therefore called the PDE method. All three methods give the same result for a specific problem. Later in this section, we discuss the advantages and disadvantages for each method.

Fig. 3.11 shows the computational results obtained by these three different methods. These computations were performed for a lossless sample with density of 2500 kg/m$^3$, sound velocity of 2273 m/s and thickness of 1.5mm (these are typical parameters for a PVC sample). The initial displacement pulse is assumed to have the same profile as the laser pulse, which is a Guassian pulse with FWHM of 100ns. This is a good

approximation if the OA experiment is laser pulse width-limited ($c_0\tau_L >> 1/\alpha$) and with the free boundary, as discussed in Chapter II. The signal plotted is the open circuit voltage. The first four echoes within 5μs are plotted. The result by the PDE method is taken from [67].

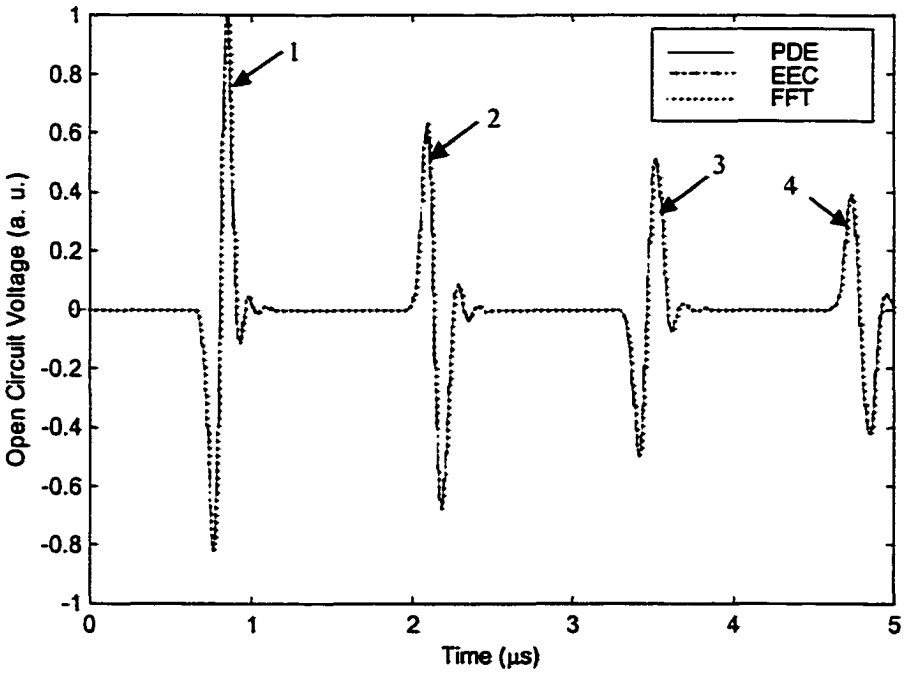


Fig. 3.11. Modeling of an optoacoustic pulse propagating in a typical sample and detected by an open circuit piezoelectric transducer. Results obtained by the PDF, EEC and FFT methods are superimposed.

It is seen from Fig. 3.11 that the results obtained by all three methods are in excellent agreement. While all three methods are clearly valid for our application, each has its advantages and disadvantages.

PSPICE is a commercial software package and has been fully tested. However it is transparent to the user, i.e., the user does not know how it approaches a problem. This restricts its applicability to some standard configurations, and offers the user a very

limited tool, especially when modeling a research experiment. One other major problem with this method is that while there is a standard model for a lossy electromagnetic transmission line in PSPICE, this model incorporates a shunt combination of conductance and capacitance. In a lossy acoustic line one needs to use a series combination of these elements [73]. Hence, utilizing the electromagnetic analog for an acoustic line requires a somewhat tedious conversion that has to be performed for every frequency component present in the input acoustic pulse.

The advantage of the PDE method is that it calculates the displacement at every position and every instant in time. However, this advantage comes with an increased CPU time requirement. An additional disadvantage with the PDE method arises with the difficulties in specifying the correct boundary conditions in situations where the reflection coefficient at the final surface has a magnitude not equal to one. For example, to model a transducer, one has to assume that the backing layer (for the transducer) is very long (several times the sample length). The lower bound on the assumed length of the backing layer depends on the number of pulse echoes one wants to simulate, since, during this time interval, one cannot have the computational artifact of non-physical echoes generated from the back of the transducer. This dramatically increases the number of calculation steps required. However, one great advantage of the PDE method is that it is able to incorporate viscosity losses of the material fairly conveniently.

The FFT method is a numerical implementation of the analytical solutions of the wave equation. It calculates the signal (pulsed or sinusoid) at specified spatial and temporal locations. It provides both time and frequency information, and is hence convenient in spectrum analysis. All the three methods require one to specify the

temporal resolution. It determines the number of discrete time instance. For example, this number could be $10^4$. The PDE method also requires specifying spatial resolution and calculates the signal during the whole time period at each discrete location. Assume, for the purposes of illustration, that the number of discrete location is about $10^4$. To complete the calculation, the CPU needs to collect at least $10^8$ data. PSPICE calculates the signal during the whole time period at each circuit node. The number of nodes is determined by the complicity of the circuit. There are about 50 nodes in the equivalent circuit for the optoacoustic experiment. The CPU needs to collect at least $10^6$ data (both the current and the voltage signal at each node). For the FFT method, the number of discrete time is the same as that of discrete frequency. The program calculates the signal at each interface of the multi-layered structure at frequency domain. For a typical OA experiment the number of the interface is less than 10. The CPU needs to collect about $10^5$ data plus one calculation of discrete Fourier transform (DFT) and one inverse DFT. The calculations of DFT and inverse DFT are based on the FFT algorithm. The above comparison reveals the fact that the algorithm used in the FFT method allows this method to generally be the fastest of the three. On the other hand, one aspect that leads to an increase in the computation time needed for the FFT method is that this method requires one to set an adequate FFT window size. Any signal outside the window will be folded back into this window. Hence, to help identify signals within or outside the window, especially with small attenuation in the sample, it may be necessary to use a large window size. This increases the CPU time.

The influence of the FFT window size is seen by comparing Fig. 3.11 and Fig. 3.12. Fig. 3.11 shows the result of an FFT analysis with a window of 30μs (only the first 4

pulses within the first 5 μs is shown). Fig. 3.12 shows the result obtained for the same problem using an FFT window equal to 10μs. Pulse 7 is physically followed by pulses 8, 9 and so on. Since pulses 8, 9 ... are outside the FFT window, they are simply folded back into the window. The 30μs window in Fig. 3.11 ensures that the echoes folded back can be neglected because their magnitudes are too small to be seen.

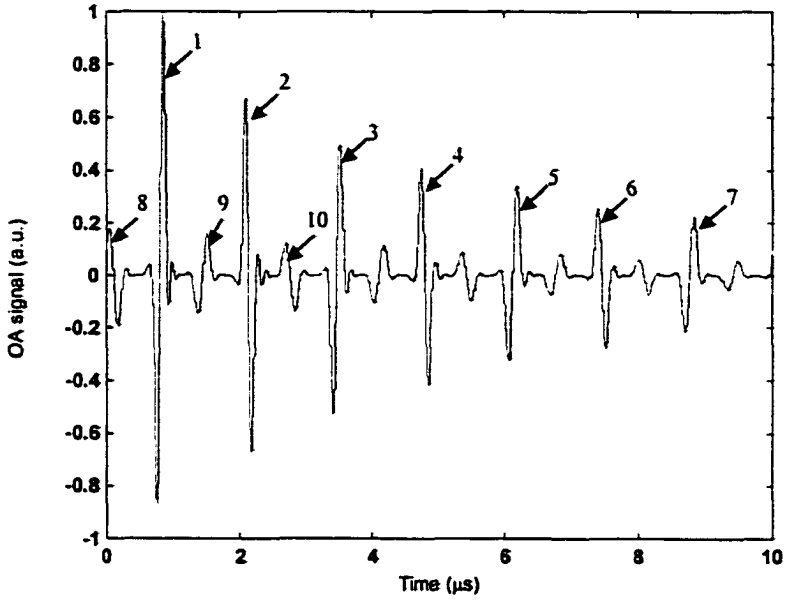


Fig. 3.12. A simulation with FFT window of 10 μs for the same problem defined for Fig. 3.11.

One attraction of the FFT method, as discussed above, is that it is flexible to deal with attenuation. The attenuation may be exponential losses, such as absorption and bulk scattering, or linear losses, such as transmission and scattering at the interface.

As mentioned above, the physically measurable signal is the voltage filtered through a highpass filter from the open circuit voltage. To compare with experimental results, each theoretical computation should include the effect of the high-pass filter. It is easy to

implement a high-pass filter by PSPICE method by simply add one capacitor and one resister to the schematic. For the FFT method, it is also convenient to multiply the open circuit signal by the transfer function of the high-pass filter in the frequency domain before implementing inverse FFT. However the PDE method only deals with the signal in time domain. A convolution of the open circuit signal and the impulse response of the high-pass filter needs to be performed. Convolution calculation would not be as easy as the previous two simulations of the high-pass filter. We have not tried it yet.

## 3.2. INDIRECT PULSED OA SIGNAL IN THE COUPLING GASEOUS MEDIUM

In the previous chapter, we have discussed non-contact detection of an optoacoustic signal utilizing an optical probe beam. We also described the optoacoustic signal generated in the adjacent fluid (often a gas) due to the temperature rise at the surface of the solid sample. This is the indirect pulsed OA signal. Such a signal is conveniently detected by a non-intrusive optical probe that suffers deflections as the result of index-of-refraction variations generated by pressure fluctuations.

In this section, we calculate the deflection of such a beam and the resultant signal generated at a photodiode detector. First, we numerically solve the thermal diffusion problem both inside the solid sample and in the fluid. The solution in the fluid is used to calculate the indirect OA signal. In addition, the solution in the sample helps to identify the condition under which the thermal diffusion-generated OA signal should decouple with the initial thermoelastic OA signal. Finally, the change of index-of-refraction due to

the acoustic wave in the fluid is calculated and this leads to a solution for the signal generated at the photodiode by beam refraction.

### 3.2.1. Numerical solution to a thermal diffusion problem

Here, we discuss a numerical method that we independently developed to solve a general one-dimensional heat diffusion problem within a medium and at the boundary, allowing for the diffusion of heat from one medium into another. We examine heat conduction at the boundary, on which an external source provides thermal energy. Having obtained the solution for this general problem, it is then simple to apply it to the more simplified cases involving only one medium or those in which there is no external thermal source.

In the numerical scheme, the spatial ($z$) coordinate is discretized, with subscript $i$ representing location $z_i$. We set the origin at the boundary; therefore, subscript $i$ varies from $-\infty$ to $\infty$ (Fig. 3.13). In general, the spatial grid size, $h$, is chosen to be different in the two materials, i.e., $h_1 \neq h_2$. (It is found that in general this choice presents an additional flexibility in the numerical scheme that is necessary for a stable solution. The criteria used to choose these grids are discussed below.) Similarly, time is also discretized, with subscript $j$ representing temporal coordinate, $t_j$, and the grid size is $\tau$. The temperature in the cell centered at $z_i$ is assumed to be $T_{ij}$ and is uniform throughout this cell. Heat is assumed to flow between this cell and the adjacent cells across the boundaries. The subscript $i$ on $T_{ij}$ denotes the spatial location, while $j$ denotes the time instant.

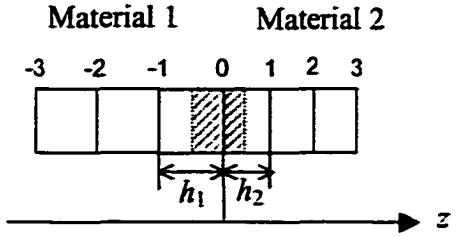


Fig. 3.13. Numerical scheme for the one-dimensional thermal diffusion problem.

The cell at the boundary where $i$=0 is in a somewhat unique location and its characteristics are used to start the numerical formulation. The width of this cell is $(h_1+h_2)/2$. We assume the temperature within this cell is uniform, which is consistent with the boundary condition that the temperature must be continuous. The heat flow into this cell from the left hand side is

$$\Delta E_{0,j}^{-} = \kappa_1 \frac{T_{-1,j} - T_{0,j}}{h_1} A\tau, \tag{3.16}$$

where $\kappa_1$ is the heat conductivity of material 1, $A$ is the cross-section (in $x$-$y$ plane) of the cell. Similarly, the heat flowing into the unit cell from the right hand side is

$$\Delta E_{0,j}^{+} = \kappa_2 \frac{T_{1,j} - T_{0,j}}{h_2} A\tau. \tag{3.17}$$

Hence, the total thermal energy growth in the cell is the sum of these two quantities and the resultant temperature rise is

$$\Delta T_0 = \frac{\Delta E_{0,j}^{-} + \Delta E_{0,j}^{+} + \Delta E_{0,j}^{x}}{A\rho_1 C_{p1} h_1/2 + A\rho_2 C_{p2} h_2/2}, \tag{3.18}$$

where $\Delta E_{0,j}^{x}$ is any additional heat generated by any external source such as the pump laser pulse.

Substituting Eq. (3.16) and (3.17) into (3.18), one gets

$$\Delta T_0 = \frac{t\left(\frac{\kappa_1}{h_1}(T_{-1,j} - T_{0,j}) + \frac{\kappa_2}{h_2}(T_{1,j} - T_{0,j})\right) + \frac{\Delta E^x_{0,j}}{A}}{(\rho_1 C_{p1} h_1 + \rho_2 C_{p2} h_2)/2}. \tag{3.19}$$

Considering the fact that thermal diffusivity $D = \kappa / \rho C_p$, the temperature for unit cell $i$=0 at time $j$+1 can be calculated from (3.19):

$$T_{0,j+1} = T_{0,j} + \frac{\left(\frac{\kappa_1}{h_1}(T_{-1,j} - T_{0,j}) + \frac{\kappa_2}{h_2}(T_{1,j} - T_{0,j})\right) + \frac{\Delta E^x_{0,j}}{At}}{\frac{\kappa_1 h_1}{2D_1\tau} + \frac{\kappa_2 h_2}{2D_2\tau}}. \tag{3.20}$$

Eq. (3.20) is the final format of the numerical solution to a one-dimensional thermal diffusion problem at a generalized boundary. The evolution of the temperature change can be obtained numerically using this equation. If there is no external heat source at the boundary, Eq. (3.20) simplifies to

$$T_{0,j+1} = T_{0,j} + \frac{\left(\frac{\kappa_1}{h_1}(T_{-1,j} - T_{0,j}) + \frac{\kappa_2}{h_2}(T_{1,j} - T_{0,j})\right)}{\frac{\kappa_1 h_1}{2D_1\tau} + \frac{\kappa_2 h_2}{2D_2\tau}}. \tag{3.21}$$

Although Eq. (3.20) is derived for the boundary, it can be applied to any location within one material by setting $h_1$=$h_2$, $\kappa_1$=$\kappa_2$ and $D_1$=$D_2$. Therefore, Eq. (3.20) can be modified for any place other than the boundary in a simple format:

$$T_{i,j+1} = \frac{D\tau}{h^2}(T_{i-1,j} + T_{i+1,j}) + (1 - 2\frac{Dt}{h^2})T_{i,j} + \frac{D\Delta E^x_{i,j}}{\kappa h A}. \tag{3.22}$$

If there is no source term, Eq. (3.22) can be further simplified to be:

$$T_{i,j+1} = \frac{D\tau}{h^2}(T_{i-1,j} + T_{i+1,j}) + (1 - 2\frac{D\tau}{h^2})T_{i,j}. \tag{3.23}$$

One can show that Eq. (3.23) can also be obtained directly from the numerical implementation of the non-source thermal diffusion

$$\frac{\partial^2 T}{\partial z^2} = \frac{1}{D}\frac{\partial T}{\partial t}, \tag{3.24}$$

as expected.

In summary, the generalized one-dimensional thermal diffusion problem can be numerically solved by Eq. (3.22) used within the medium and Eq. (3.20) at the boundary. Starting with an initial temperature distribution in space at time $j$=0, the temperature can be calculated at any location and at any time.

To validate this numerical scheme, first we checked the energy conservation of the system. Then we compared the numerical results with the analytical solutions. Both methods verified that as long as the value of $Dt/h^2$ is properly set, the numerical scheme works well.

### A. Conservation of energy test for numerical solution

The total thermal energy of the system (material 1 and material 2) at time $j$ can be calculated by the following equation, by adding the thermal energy stored in each cell:

$$E_j = \frac{Ah_1\kappa_1}{D_1}\sum_{i<0} T_{i,j} + \frac{Ah_2\kappa_2}{D_2}\sum_{i\geq 0} T_{i,j} + \frac{AT_{0,j}}{2}\left(\frac{h_1\kappa_1}{D_1} + \frac{h_2\kappa_2}{D_2}\right). \tag{3.25}$$

If the system does not have any external heat sources, $E_j$ should be a constant for all $j$. Numerous tests were run and it was found that energy is conserved when $Dt/h^2 < 0.5$. This condition has also been found to be necessary by other researchers who have found it to be true for this problem, but by using another method [74].

**B. Consistency of numerical solution to simple analytical solution**

If the initial temperature is a delta pulse in the middle of an infinite long material and there is no external heat source, the analytical solution of this thermal diffusion problem is

$$T(x,t) = \frac{1}{2(\pi Dt)^{1/2}} e^{\frac{(x-x_0)^2}{4Dt}}. \tag{3.26}$$

This analytical solution can be used to test our numerical scheme. Fig. 3.14 shows such a comparison between these two calculations. Initially, there is a delta pulse at $z = 2.8 \times 10^{-4}$ m. This temperature impulse starts to diffuse in both directions in the sample ($D = 2.3 \times 10^{-4}$ m$^2$/s). Fig. 3.14 plots the temperature distribution in space at two time instants by both analytical and numerical calculations. It can be clearly seen that the numerical scheme works well.

**C. Comparison of numerical and analytical solutions to an OA problem**

Fig. 3.15 shows another comparison of results to a thermal diffusion problem by the numerical and analytical methods. In this example, the temperature distribution for a practical OA problem is solved. The thermal energy initially comes from the absorption of a laser pulse with the FWHM of 7.5ns. The absorption coefficient ($\alpha$) of the sample is $8.7\times10^{4}$m$^{-1}$, taken from one of our measurements for $\alpha$ (details in Chapter VI). The solid sample (location $z<0$) has a diffusivity of $6.4\times10^{-8}$m$^2$/s, and a thermal conductivity of 0.167 Js$^{-1}$m$^{-1}$. For the gas ($z>0$), the thermal diffusivity is $2\times10^{-5}$m$^2$/s and the thermal conductivity is $2.6\times10^{-2}$ Js$^{-1}$m$^{-1}$. This figure plots the temperature distribution in the solid sample and in the gas at time 160ns after the laser starts to deposit energy. The analytical

solution was obtained by the RG model, which was introduced in the previous chapter. Since the RG model only gives the solution to a sinusoidal heat source, we have used the Fourier transform and its inverse transform to decompose and synthesize the pulse signal.

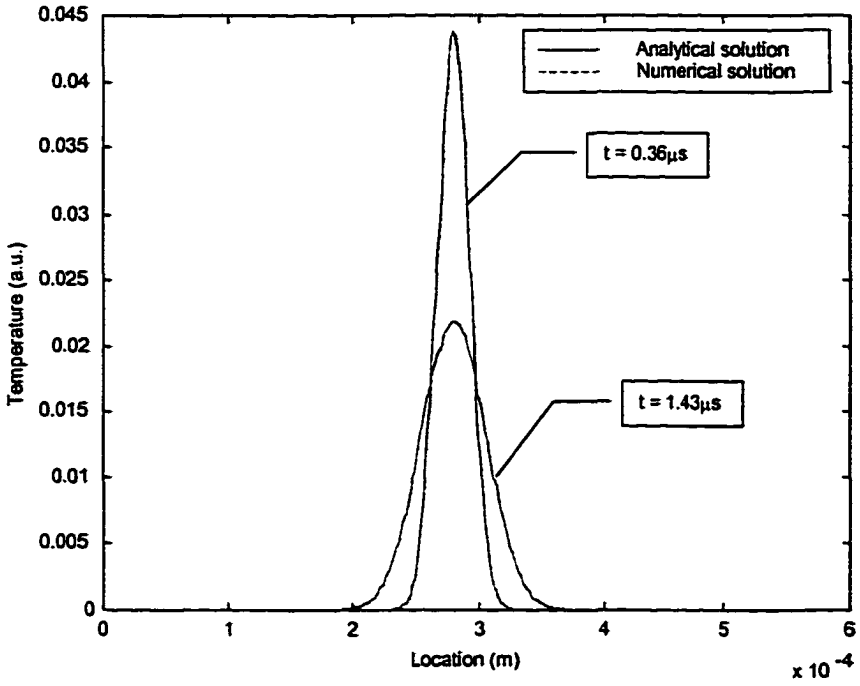


Fig. 3.14. Solutions to a thermal diffusion problem where the initial temperature is an impulse in the middle of the sample ( $D = 2.3 \times 10^{-4} m^2/s$ ). Here the boundaries are far from the center, and, therefore, the diffusion is considered to occur in an infinite long medium.

Fig. 3.15 shows that the results given by the numerical and analytical methods are in good agreement. The slight difference in the gas (z>0) that leads the temperature to negative values from the analytical solution, which is physically incorrect, may come from the FFT technique. FFT is a numerical implementation of the Fourier transform. It assumes that the signal it takes for the transformation is periodic. Errors may be introduced when the inverse FFT is used to recover an aperiodic signal.

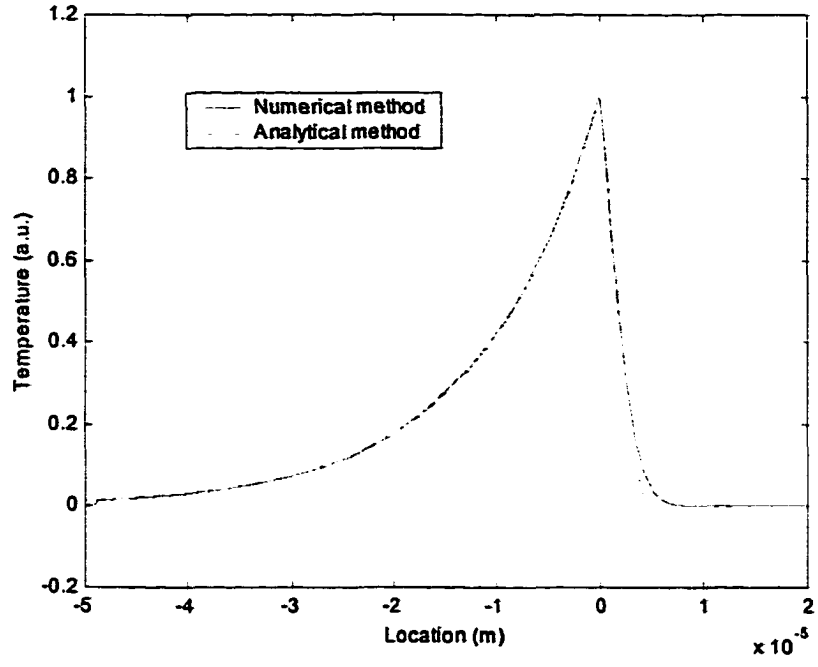


Fig. 3.15. Solutions to a thermal diffusion problem with a boundary condition by the numerical method and by the analytical method (RG model and the Fourier transform). The thermal energy is initially deposited by a laser pulse with FWHM of 7.5ns. The figure shows the temperature distribution in the solid sample (location $z<0$) and in the gas ($z>0$) at time 160ns after the laser starts to deposit energy.

## D. Minimization of error in numerical calculation

In the numerical calculation, the choice of the value of $D\tau/h^2$ is important. If the value is set to be too small, the error will build up in the later steps. If this value is too large, the sampling rate is not enough to follow the rapid change of temperature in the very early stages. As mentioned above, many test runs showed that the value of $D\tau/h^2$ must be smaller than 0.5. It is to be emphasized that in this dissertation no attempt was made to investigate the mathematics of numerical analytical theory.

In the simplified problem above, it is possible to perform numerical experiments to find which value of the parameter results in the smallest error since the exact analytical solution is known. After several tests it was found that the value of $D\tau/h^2$ should be set

to 0.1661 to minimize the numerical error. The experiments showed that primary errors often occur at the center of the temperature pulse ($z = z_0$). The error at $z = z_0$ in the example shown in Fig. 3.14 was calculated to be 2.24% under the condition $D\tau/h^2 = 0.1661$. For a real application, this error is expected to be less, because the actual temperature would not change impulsively.

### 3.2.2. Calculation of the pressure profile due to thermal diffusion

Our numerical method allows one to calculate the temperature at anytime and anywhere during the thermal diffusion process. Therefore, one is able to calculate the acoustic signal generated by thermoelastic effect due to the temperature variation caused by thermal diffusion. As discussed in Chapter II, the resultant acoustic signal in the solid sample is called the thermo-acoustic portion of the total optoacoustic signal. The resultant acoustic signal in the surrounding fluid (often just air) is called the indirect OA signal. At each time instant, the newly generated pressure is proportional to the change of temperature. As soon as a pressure signal is generated at one place, it starts to propagate to the wave direction at sound speed. Therefore, the pressure at a certain place and a certain time is the sum of the pressure generated locally and the pressure propagated from other places generated sometime ago. The analytical expression of this pressure signal due to thermal diffusion has been described by Eq. (2.20). It is repeated here for a quick reference:

$$p_{ac}(z-ct)=\int_0^{\infty}dt'\int_0^{\infty}dz'\frac{\partial T(z',t')}{\partial t'}\delta(z'-z+c(t-t'))\ \ (z>ct),$$

$$p_{ac}(z-ct)=\int_0^{\infty}dt'\int_0^{\infty}dz'\frac{\partial T(z',t')}{\partial t'}[\delta(z'-z+c(t-t'))+k_r\delta(z'+z-c(t-t'))]\ \ (z<ct). \tag{3.27}$$

In this section, the numerical algorithm for implementation of the above equations used to calculate the pressure signal is given through an example. Our algorithm solves a difficulty that may appear if the time and space grids for the acoustic signal and for the temperature distribution are different.

Fig. 3.16 is the schematic used for the example where we calculate the pressure signal in the solid sample monitored at $z = z_2$, as well as the signal in the fluid monitored at $z = z_2'$. First, we calculate the temperature distribution at discrete locations and discrete times in both the solid and the fluid. Then, we calculate the temperature increments for all times and locations, i.e., $\Delta T(z_i, t_j)$. Finally, we add all correlated $\Delta T$ in a manner described below and yield the pressure profile.

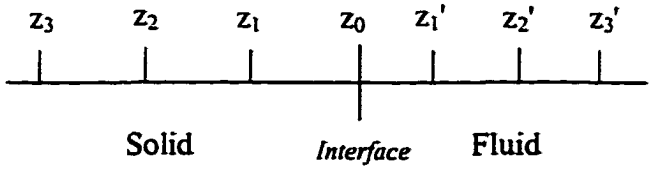


Fig. 3.16. Schematic for the calculation of the pressure signal due to thermal diffusion.

### A. Thermo-acoustic (pressure) signal in the solid sample

Previously we have discussed the criteria of choosing the time and spatial grids. Here we summarize these criteria. Let $\tau_{th}$ be the time grid, and let $h_s$ and $h_f$ be the spatial grids for the solid and the fluid respectively. Then $D_m\tau_{th}/h_m^2 < 0.5$, where $m$ denotes either $s$ or

*f*. For minimum error, $D_m\tau_{th}/h_m^2 = 0.1661$. There is another set of time and spatial grid, namely $\tau_a$ and $\chi_a$. It is required that $\chi_a = c_s\tau_a$, where $c_s$ is the sound speed in the solid. Generally, these two sets of grids do not share the same values, because there is a different requirement for each set. This mismatch produces some difficulties for the conversion from temperature to pressure. The solution is to use the interpolation technique to generate a new set of data in a manner that both the temperature and the pressure have the same sampling rates in both time and space.

To reduce the amount of interpolation, we let the two signals have the same time grid, i.e., $\tau_{th} = \tau_a$, and one spatial grid is integer times of the other, i.e., either $h_s = N\chi_a$ or $Nh_s = \chi_a$, where $N$ is an integer. This can be achieved by setting

$$\tau = \tau_{th} = \tau_a = \frac{D_s}{N^2 A c_s^2} \quad (\text{if } h_s = N\chi_a), \tag{3.28}$$

or

$$\tau = \tau_{th} = \tau_a = \frac{N^2 D_s}{A c_s^2} \quad (\text{if } Nh_s = \chi_a), \tag{3.29}$$

where $A = D_m\tau_{th}/h_m^2 = 0.1661$.

Then

$$h_m = \sqrt{D_m \tau / A^2}\,, \tag{3.30}$$

and

$$\chi_a = c_s\tau\,. \tag{3.31}$$

If $h_s = N\chi_a$, then only $N$-1 linear interpolations are required between $\Delta T(z_i, t_j)$ and $\Delta T(z_{i+1}, t_j)$. In the case of $Nh_s = \chi_a$, $N$-1 interpolations are required between $\Delta T(z_i, t_j)$ and $\Delta T(z_i, t_{j+1})$. Note that each new interpolated sample, as well as the existing sample at ($z_i$,

$t_j$), now has the value of $\Delta T(z_i, t_j)/N$. This is not a linear interpolation, and the algorithm is required by the principle of energy conservation.

Suppose we need to monitor the acoustic signal at location $z_2$, we can use the scheme described below with the aid of Fig. 3.17. In this example, $N$=2, i.e., $h_s = 2\chi_a$. We first calculate $\Delta T$ at location $z_0$, $z_1$, $z_2$ and at time $t_1$, ... , $t_9$ (circles in the figure). Then we linearly interpolate data at location $z_{01}$ and $z_{12}$ at each time instant (stars in the figure). At time $t_1$, the pressure signal is the one generated locally at ($z_2$, $t_1$). At time $t_2$, the signal is the one generated locally at ($z_2$, $t_2$) plus the one propagated from its neighbor but generated at last time instant, i.e., the value at ($z_{12}$, $t_1$). This method applies for all the rest of the time instants. Therefore, the pressure signal at location $z_2$ at each time instant is the sum of data on the diagonal line as illustrated in the figure. Note that, to be complete, pressures generated in locations on the left of location $z_2$ sometime ago need also be added to the signal. However, this contribution can be neglected if $z_2$ is far away from the absorption region.

We have used the method illustrated in Fig. 3.17 to calculate the thermo-acoustic portion and then the total OA signal for a case where the influence of thermal diffusion cannot be neglected. Fig. 3.18 shows the theoretical OA signal generated in an aluminum sample by a laser impulse, considering the thermal diffusion effect (blue) or not (red).

The parameters used for the calculation are: absorption in aluminum $\alpha = 10^8 m^{-1}$, diffusivity $D_s = 9\times10^{-5} m^2 s^{-1}$, and sound velocity $c_s = 6.3\times10^3 m/s$. Since $D_s\alpha/c_s = 1.4$, the decoupling condition, Eq. (2.21), i.e., $d >> D_s/c_s$, is not met ($d$ can be approximated by $1/\alpha$). Therefore, the thermo-acoustic wave should strongly couple with the OA wave. This is seen in Fig. 3.18 where the total OA signal with thermal

diffusion is quite different from the signal for which thermal diffusion is not considered. The profile that we obtained while considering the thermal diffusion effect is in agreement with Thomsen's result [28]. We have also tested the case where the decoupling condition Eq. (2.21) is met using the same method. No obvious coupling between the thermo-acoustic and optoacoustic waves was observed.

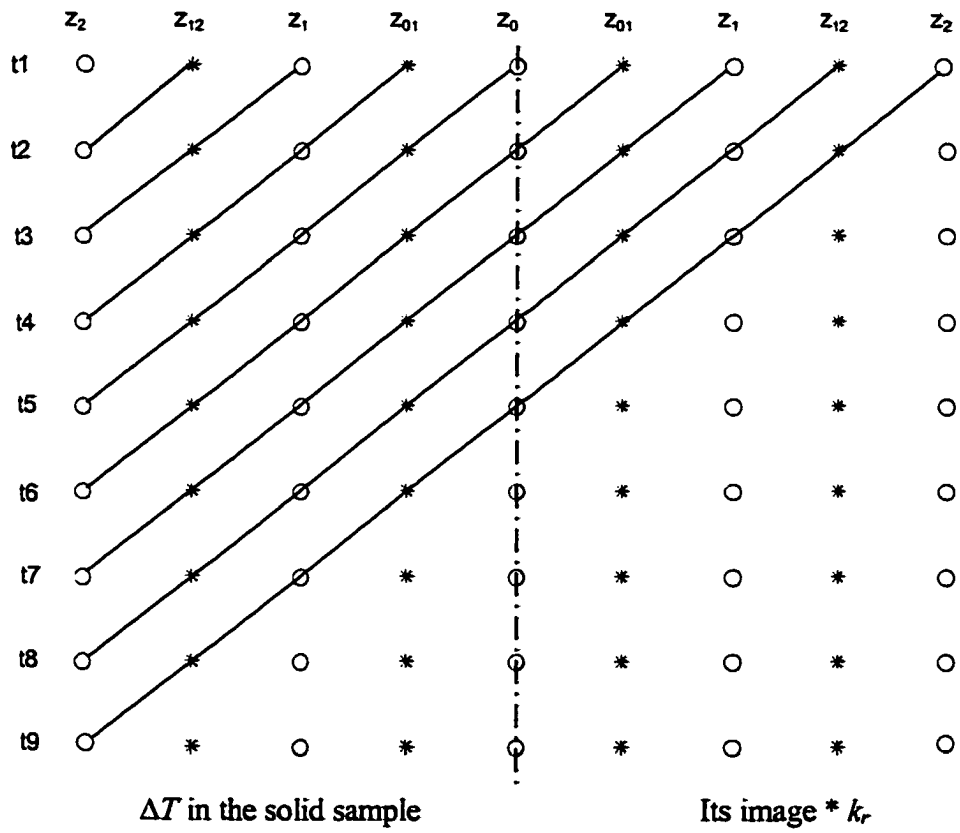


Fig. 3.17. Calculation of acoustic signal at location $z_2$ from temperature changes $\Delta T$ in the solid sample. The circle denotes the data derived from the numerical algorithm for the thermal diffusion. The star denotes the interpolated data. The acoustic signal at each time instant is the sum of the data on the corresponding diagonal line.

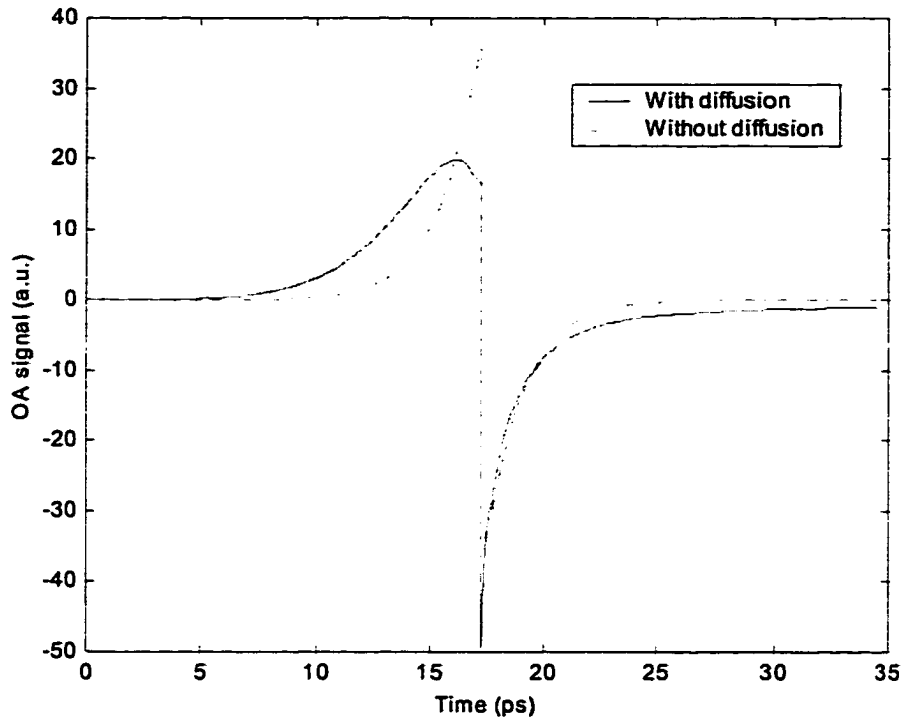


Fig. 3.18. Theoretical OA signal generated in an aluminum sample by a laser impulse, considering the thermal diffusion effect (solid) or not (dashed). In this case, the decoupling condition, Eq. (2.21), is not met since $D_s\alpha / c_s = 1.4$. This indicates the thermo-acoustic wave and the OA wave are strongly coupled, which is proven by the computed results.

## B. Indirect OA (pressure) signal in the fluid

Calculation of the indirect OA signal in the fluid follows the same steps used for the calculation of the thermo-acoustic signal in the solid. The rules for selection of temporal and spatial grids also apply here. However, if one desires to obtain both the thermo-acoustic and the indirect OA signal from one experiment, one may need to calculate the temperature distributions twice using different sets of time and spatial grids, one for the thermo-acoustic signal and the other for the indirect OA signal. This is because it is difficult to simultaneously fulfill the selection rules for the solid and for the fluid.

Because of the geometry shown in Fig. 3.16, the indirect OA signal at $z_2'$ at each time instant is the sum of data on the cross diagonal line illustrated in Fig. 3.19. Again, here we neglect the contribution from the pressures generated at locations on the right of location $z_2'$ because of their weak amplitudes.

Although the method used to calculate the indirect OA signal in the fluid is the same as that used for the thermo-acoustic signal in the solid, physically there are two differences between these two calculations. First, the initial condition of the thermal diffusion problem in the solid has the profile of the energy absorbed in the solid, which is an exponentially decaying curve, while the initial condition for the fluid is zero everywhere. Second, the pressure signal generated in the fluid is purely due to thermal diffusion; no direct optoacoustic signal is produced in this region.

Fig. 3.20 is the calculated indirect OA signal in the air due to the excitation of a PVC sample with a laser impulse. The absorption coefficient of PVC was assumed to be $\alpha = 4.3 \times 10^{4} m^{-1}$, diffusivity for PVC $D_s = 6.4 \times 10^{-8} m^2 s^{-1}$. For the fluid (air) $D_f = 2 \times 10^{-5} m^2 s^{-1}$, sound velocity $c_f = 366 m/s$. The signal was monitored in the air at $z$ = 1.256mm. This result shows that the indirect OA signal corresponding to a laser impulse is also impulse-like but asymmetric with a long tail. The contour of the tail is determined by many factors, such as the thermal properties of the solid and the fluid, as well as the optical absorption coefficient of the solid. It is difficult to directly extract the information of each of these parameters from the profile of the signal. For a practical laser pulse with finite pulse width, as a rough estimate, one should expect that the pressure signal in the fluid follows the profile of the laser pulse, since the actual pressure

signal has a profile resultant from the convolution of the laser pulse and the impulse response illustrated in Fig. 3.20.

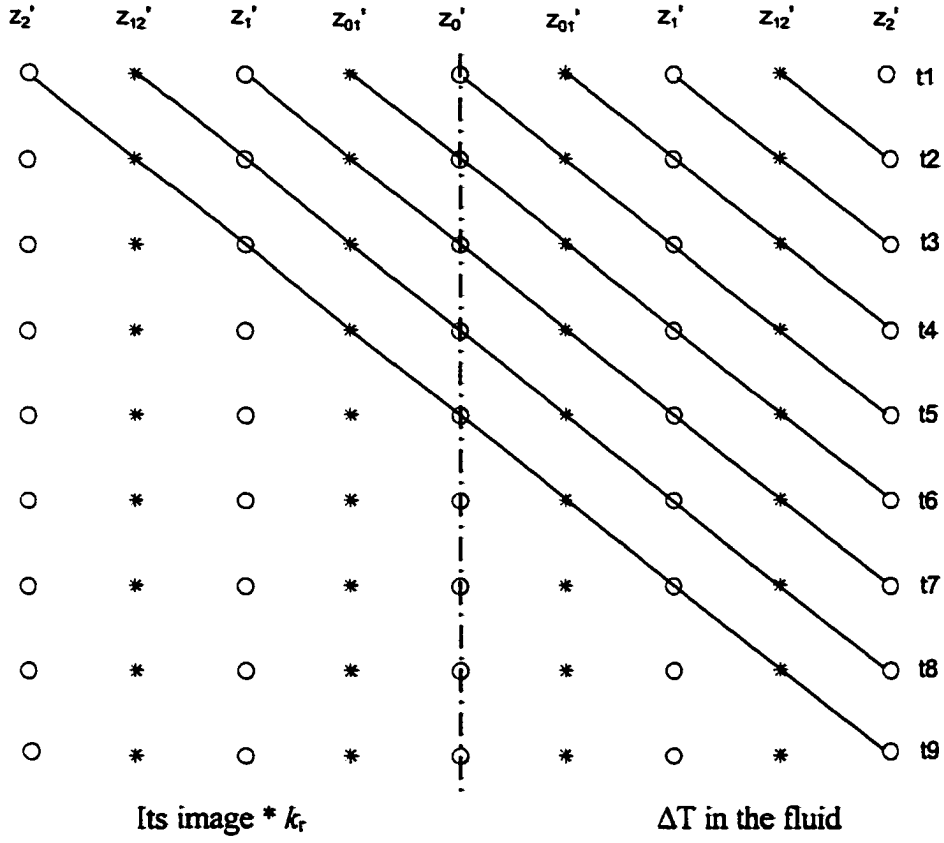


Fig. 3.19. Calculation of acoustic signal at location $z_2'$ from temperature changes ΔT in the fluid. The circle denotes the data derived from the numerical algorithm for the thermal diffusion. The star denotes the interpolated data. The acoustic signal at each time instant is the sum of the data on the corresponding cross diagonal line.

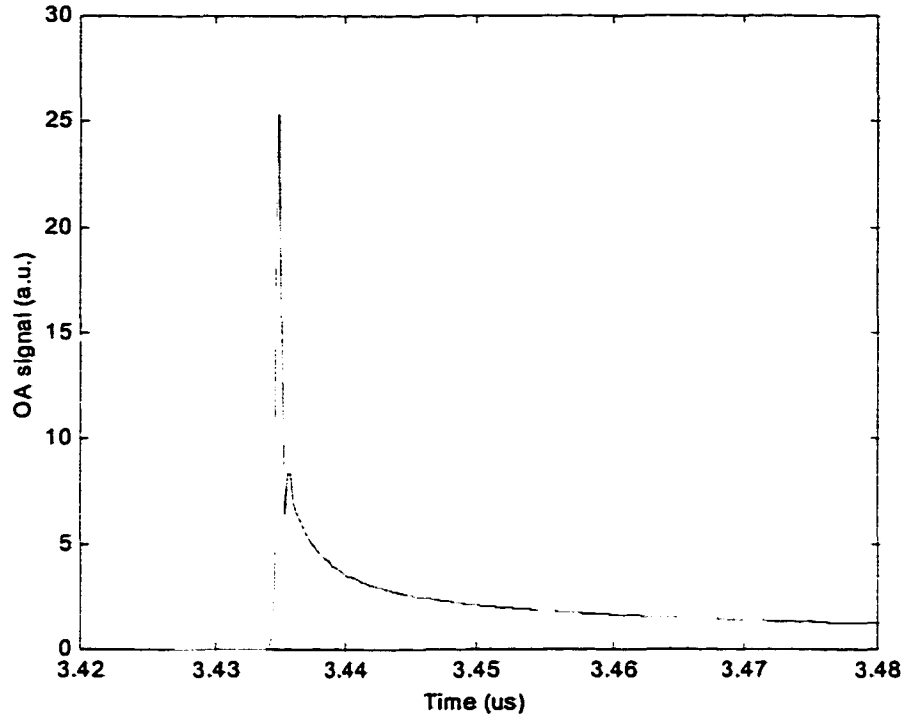


Fig. 3.20. Theoretical indirect OA (pressure) signal generated in the air by exciting a PVC sample using a laser impulse.

### 3.2.3. The indirect OA signal detected by the beam refraction method

In Chapter II, we have discussed the principle of utilizing the beam refraction method to probe an acoustic signal in a medium. This method can be used to detect the indirect OA signal in the surrounding air. The deflection angle can be calculated from Eqs. (1.45) and (1.46). If one is only interested in the signal profile, the relation of the deflection angle $\delta$ and the pressure $p$ can be expressed by combining these two equations as follows:

$$\delta(x) \propto \int_b^b \frac{\partial p(x,z)}{\partial t} dz \,. \tag{3.32}$$

The geometric relation of the acoustic field and the probe beam is shown in Fig. 3.21.

Since we assume that the acoustic wave is a plane wave, $\partial p / \partial t$ along the $z$ direction remain unchanged for a fixed $x$. Therefore, the profile of $\delta$ (and, hence, the detected signal) is the time derivative of the pressure signal, if the probe beam has a very narrow dimension $2a$. However, normally this dimension cannot be neglected because the sound velocity in air is relatively slow. A typical probe beam has a dimension $2a$=100μm, and it takes about 0.3μs for the acoustic wave to pass through this length. The pressure pulse in our experiment has a pulse width less than 100ns, which is estimated from the pulse width of the pump laser. Therefore, if such a probe beam is used to detect this acoustic signal, the result will suffer tremendous broadening. The detected signal can be calculated as the convolution of the pressure signal and the spatial profile of the probe beam. In our measurement, this broadening was obvious. These results will be shown in Chapter IV.

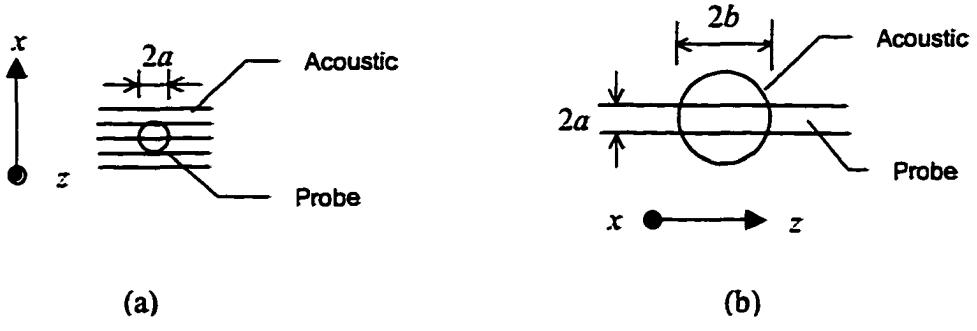


Fig. 3.21. Geometric relation of the acoustic field and the probe beam: (a) in the $x$-$y$ plane; (b) in the $y$-$z$ plane. $2a$ is the dimension of the probe beam and $2b$ is the dimension of the acoustic field, which is roughly the same as the pump beam.

# CHAPTER IV

# EXPERIMENTS AND RESULTS OBTAINED

In this chapter, two types of optoacoustic experiments, both utilizing pulsed light sources, are described. For the first type experiment, a piezoelectric transducer is in contact with the back epicenter of the sample; while for the second type, a probe beam in the surrounding air and parallel with the front surface of the sample is used to detect the indirectly generated OA signal. Apparatuses for both type experiments are described with the aid of schematics, followed by the experimental results and discussions. We have used the methods developed in Chapter III to model these experiments. The theoretical results are also presented together with the experimental ones. It will be seen that most of these theoretical results are in quantitative agreement with the experimental ones.

## 4.1. EXPERIMENTS

### 4.1.1. Setup for contact detection using a piezoelectric transducer

An optoacoustic experiment using a piezoelectric transducer to pick up the acoustic signal is illustrated in Fig. 4.1. Light pulses from a laser are incident to the sample surface and OA signals are initiated in the absorption region. Four pulsed lasers have been used in our experiments, namely a diode laser (Hamamatsu L4356-01), a nitrogen laser (Laser Photonics LN103C), a Nd:YAG laser (Physics) and an excimer laser (Tachisto 801XR). For the last one, we actually used the incoherent light of the passivation mixture. From now on, we will call this incoherent light the passivation light.

The acoustic signal was picked up at the back of the sample by a 20MHz (center frequency) piezoelectric transducer (Panamatrics V116-RM). Depending on the magnitude of the signal from the transducer, one or two stages of amplification may be needed. The first stage is a pulse amplifier (Picosecond Pulse Labs® 5818B), with a gain of 18dB. The second stage is the internal amplifier of an oscilloscope (Tektronix 7804) with a gain of about 14dB. The amplified signal was fed to a 400MHz digital oscilloscope (Tektronix TDS380). The signal was also sampled and digitized by the scope, and the data were sent to a PC for further processing and storage through a GPIB interface. The scope was triggered either by the trigger output from the laser driver (for the diode laser and the Nd:YAG laser) or by the laser pulse split from the main pulse and received by a photo multiplier (for the nitrogen laser) or a photodiode (for the passiviation light). Since the signal was generally noisy, 256 shots were averaged to obtain a clean signal by the scope itself before the data were transferred to the PC.

Table 4.1 lists wavelength, pulse width, energy per pulse and repetition rate for each laser. The pulse widths were measured from the pulse profiles shown in Fig. 4.2. The profiles were taken by a photo multiplier (for the nitrogen laser) or by a photodiode (for other lasers) with fast enough rise time. For instance, the photodiode (Thorlabs DET200) used has a rise time of 1ns. The pulse energy was estimated from the menu and the condition of the laser.

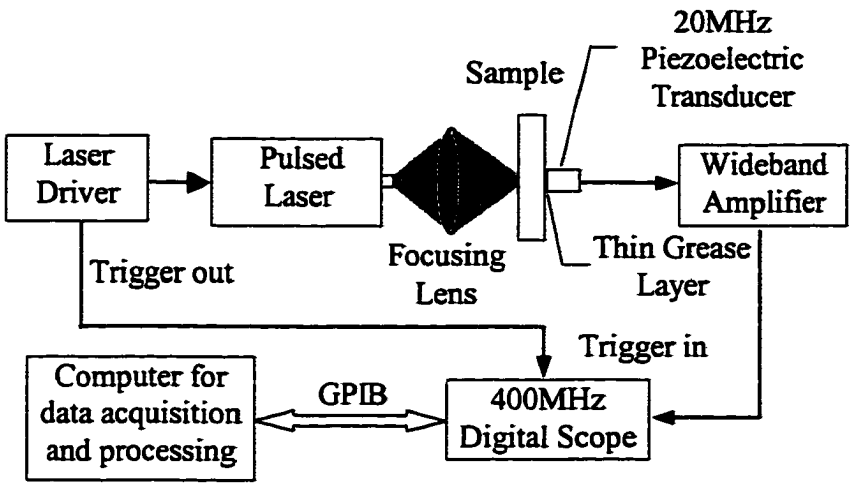


Fig. 4.1. Schematic of apparatuses used for an optoacoustic experiment. The acoustic signal is picked up by a piezoelectric transducer. The experimental data are averaged by a digital scope and stored in a PC for signal processing.

Table 4.1. Specifications of light sources used in optoacoustic experiments

| Light Source | Wavelength | Pulse Width (FWHM) | Operation Repetition Rate | Typical Energy Per Pulse |
|---|---|---|---|---|
| Diode Laser | 880nm | 101ns | 1kHz | 2μJ |
| Nitrogen Laser | 337nm | 2ns | 5Hz | 50μJ |
| Passivation Light | 773nm | 11ns | 1Hz | 1mJ |
| Nd:YAG | 1064nm | 54ns | 5Hz | 100mJ |

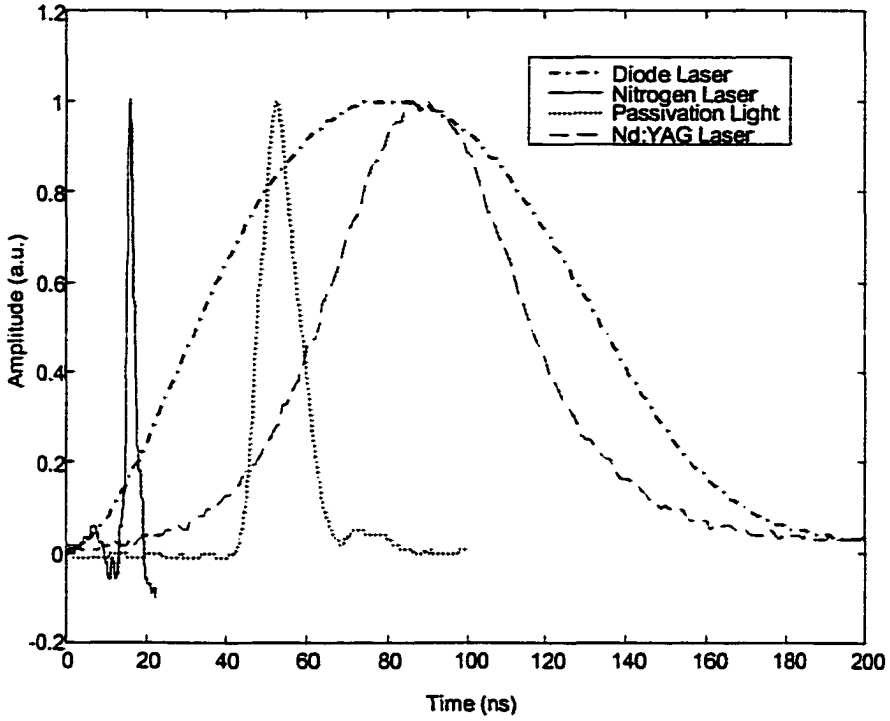


Fig. 4.2. Temporal profile of light pulses used in optoacoustic experiments. The pulse widths have been measured and listed in Table 4.1.

The diode laser that we used has the weakest pulse energy (see Table 4.1). Such a weak laser is not often used in literature to excite OA signals, yet we were able to use it to generate signals with reasonably high signal-to-noise ratio. The advantages of utilizing a semiconductor laser include (a) the compact size of the whole system; (b) it is inexpensive; (c) there is no RF noise from gas discharge existing in other lasers used; and (d) a high repetition rate.

In order to efficiently and conveniently transfer data from the digital scope to the computer, we used LabVIEW to program a Windows application. LabVIEW is a graphical programming language designated for scientific instrumentation. It can directly manipulate a data acquisition board, or control and communicate with other devices

through a data interface or a data bus such as GPIB (general purpose industrial bus). A LabVIEW program is called a VI (virtual instrument). A VI has two parts, namely the panel and the diagram. The panel is the graphical user interface, which contains indicators and controls. The diagram is a graphic representation of the codes.

Fig. 4.3 shows a part of the panel of the VI that is used to communicate with the scope as well as to process experimental data. The diagram of this VI is given in Appendix II. This VI can acquire a signal from the scope or load the data of a signal from a disk file and then display the signal on the screen. It can also save the whole acquired signal or the portion selected by the user to a disk file.

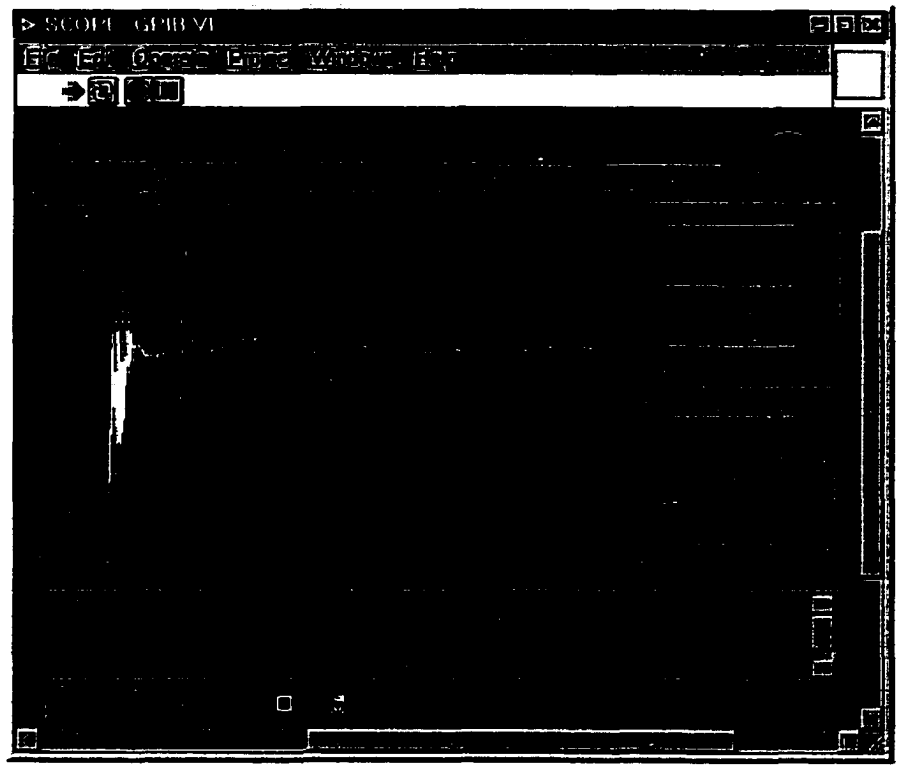

Fig. 4.3. Front panel of the LabVIEW VI (Virtue Instrument) for data acquisition and processing.

For an OA experiment, if the background noise is not random, one can obtain the signature of the noise by blocking the laser and then saving it as a reference. Later, this background noise can be subtracted from a measurement with the laser unblocked, which yields a better signal. The VI provides such a function that allows the user to subtract the noise, whose data have been saved in the disk, from the current on-display signal (the "Subtract" button).

The file used to store the data of a signal is in ASCII mode. Each file has a header and a data area. The header contains a description of the signal and the experiment. The data area contains data of time and amplitude of the signal. When a signal is acquired from the scope, the user can type a description such as date and experimental conditions in the "Comments" box. Later the description will be automatically retrieved and displayed in the same text box when the data file is loaded from the disk.

By default, the useful data are only located in the second half of an acquisition from the scope. One can use the "Half Screen" button to zoom to the second half, or one can directly type the upper and low borders of the display window.

This VI provides a smoothing function for further noise removing if the averaging function of the scope does not give a satisfied result. It utilizes a time window whose size can be preset by the user to slide along the time axis of the signal and smooth out the sharp features. Chapter V discusses some other signal denoising methods, such as the wavelet technique.

The "Address" in the front panel refers to the address of the device (i.e., the scope) to which the GPIB connects. The "Channel" refers to the five channels available from the

scope, namely CH1, CH2, MATH, REF1 and REF2. The "Format" defines how the data is interpreted, with the choice of "Unsigned" (all positive) and "Signed" (bipolar).

The VI also provides tools (not shown in Fig. 4.3) for the user to communicate with the scope manually by typing commands in a text box. Although they are rarely used, they are necessary if the user needs to manipulate the scope through functions not provided above.

### 4.1.2. Setup for noncontact detection using a probe beam

Fig. 4.4 is the schematic of the apparatuses used for OA generation and detection by a non-contact probe beam. It is similar to the experimental setup for the contact detection discussed above, except that there is no piezoelectric transducer at the back of the sample. Instead, a probe beam is located in front of the sample. The probe beam does not penetrate into the sample but passes through the surrounding air. The beam is parallel with the surface of the sample. Any changes of the index-of-refraction of air caused by the density fluctuation due to the pressure wave in air will refract the optical beam. As a result, the probe beam changes it propagating direction. In our experiment, a knife-edge was used to partially block the probe beam. A photodiode was placed behind the knife-edge to detect the intensity changes of the portion that was unblocked. Normally the angle of the changing direction is very small. Therefore, the photodiode was placed at a reasonably long distance (about 1.5m) to the probe-acoustic interaction region in order to have relatively large displacement at the detection plane.

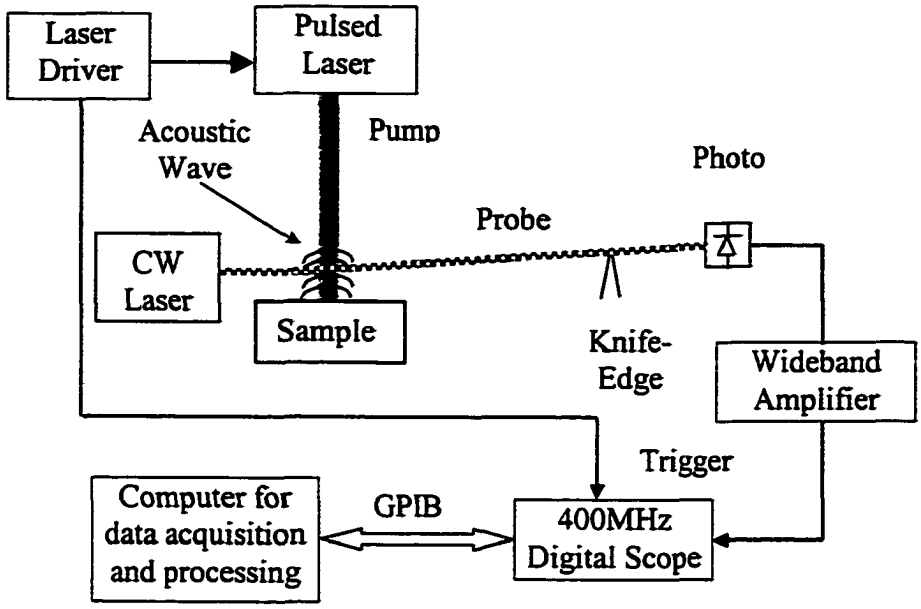


Fig. 4.4. Schematic of apparatuses used for an indirect OA generation. The acoustic signal in air is detected by the photo diode responding to the probe beam refraction.

As discussed in Chapter III, a high intensity probe laser is required to get a high signal-to-noise ratio. In our experiment, a diode laser (Sanyo DL-7140-201) with 70mW maximum output was used. In literature, higher power up to hundreds mW has been used.

Theoretically, such a detection scheme is able to probe three signals due to the absorption of laser energy in the solid sample. One is the indirect OA generation in the air. Another is the OA signal generated in the solid sample and transmitted from solid-air interface. The third is the photothermal signal, which also causes beam refraction not by the pressure, but by the increased temperature due to the thermal energy diffused from the interface.

The indirect OA signal and the transmitted pressure signal are overlapped in time. Due to the large acoustic impedance mismatching, the transmission efficient is very low. Therefore, the indirect OA signal generally is dominant. These two signals can be

identified by the signal duration. The indirect OA signal only has one pulse because the air can be considered as a semi-infinite long medium and there is no reflection occurring at the other end. However, the transmitted pressure signal normally has echoes following the first pulse due to the multi-reflection at both ends of the solid sample. The photothermal signal can be almost completely separated from the OA signals because it arrives at the detection site with much longer delay. This is due to the slow speed of thermal diffusion compared with the acoustic velocity. For our experiment, the OA signal was normally observed in microsecond scale while the photothermal signal was found in millisecond scale.

The sensitivity of our non-contact detection system was not optimized so that the transmitted pressure signal has not been clearly recorded yet. In section 4.2.2, we will present the results of the indirect OA signals. Although the photothermal signals were also observed in experiments, they will not be discussed in this work since they are irrelevant to the subject.

## 4.2. RESULTS OBTAINED AND COMPARISONS WITH THEORIES

### 4.2.1. Contact detection with PVC samples at various wavelengths

Optoacoustic experiments were first performed on PVC material using the diode laser at a wavelength of 880nm. A series of PVC samples with various thicknesses, as well as those with a multi-layered structure, were used. Theoretical calculations based on the experimental conditions were also done to compare with the experimental results.

Three other light sources, namely the nitrogen laser at 337nm, the Nd:YAG laser at 1064nm and the passivation light at 773nm, were also used to excite OA signals in a PVC

sample. These experimental results, as well as the corresponding theoretical results, are given below.

The experimental setup has been described previously. To obtain the theoretical results, we first used the convolution theory to calculate the pressure signals generated in the absorption region, and then used the FFT method developed in Chapter III to calculate the voltage signals from the piezoelectric transducer.

The profiles of the pump pulses have been measured and plotted in Fig. 4.2. The optical absorption coefficients were also experimentally measured by the spectral ratio technique that we developed and will be presented in Chapter VI. Therefore, the pressure profile induced by a laser impulse can be calculated by Eq. (1.14) given in Chapter II. Then the pressure profile induced by a practical optical pulse is the convolution of the pulse profile and the OA impulse response.

The FFT method models the experiment as an acoustic signal propagating in multiple layers. These layers namely are the surround air, the sample (one or more layers, dependent of the sample's structure), the piezoelectric plate and the backing. The displacements at the two ends of the piezoelectric plate were used to produce the theoretically calculated voltage signal.

### A. OA results by the diode laser

The OA results from experiments on PVC material with various thicknesses are shown in Fig. 4.5, Fig. 4.6 and Fig. 4.7. These thicknesses are 2mm, 1.5mm, and 1mm, respectively. All theoretical results are superimposed onto the experimental ones in these figures. All the parameters used in the theoretical calculations are kept the same except

the sample thickness. The optical absorption coefficient is $\alpha = 28\text{mm}^{-1}$ (see Chapter VI). An effective acoustic attenuation constant $\beta = 0.17\text{mm}^{-1}$ has been assumed for all three calculations. Note that it is an approximation by assuming $\beta$ a constant since, in general, it is frequency dependent. In our calculations we assumed the attenuation constant does not depend on frequency, because the signal's bandwidth is relatively small (less than 10MHz). The value of $\beta$ came from experiments. It can be obtained from the ratio of an acoustic echo to its preceding one, since this ratio is the product of the reflection coefficients at two boundaries, which are already known, and the percentage of the acoustic signal leftover after other losses during one round trip in the sample.

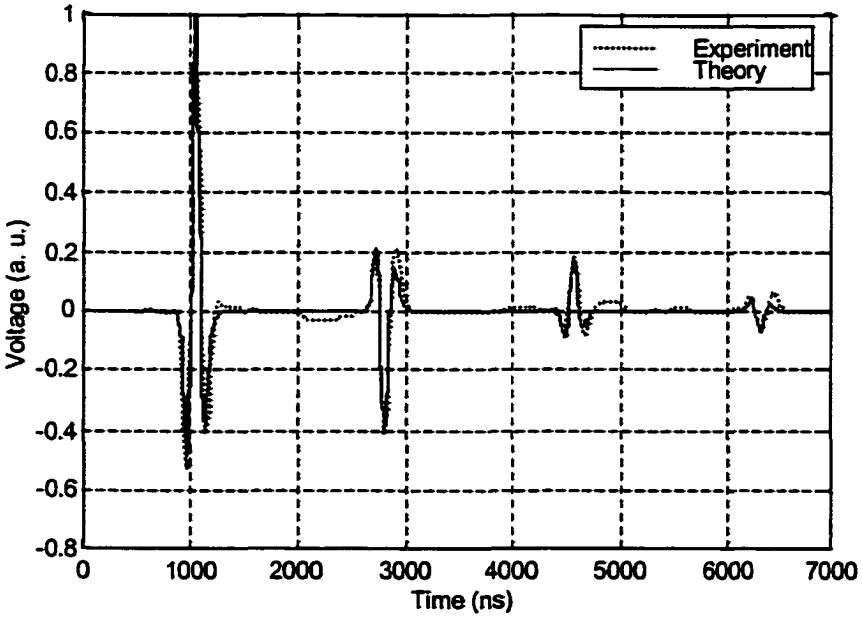


Fig. 4.5. Experimental and theoretical results from a 2mm-thick PVC sample by the diode laser. For the theoretical calculation, laser pulse width $\tau_L$ = 101ns, optical absorption $\alpha$ = 28mm$^{-1}$, and acoustic attenuation $\beta = 0.17\text{mm}^{-1}$.

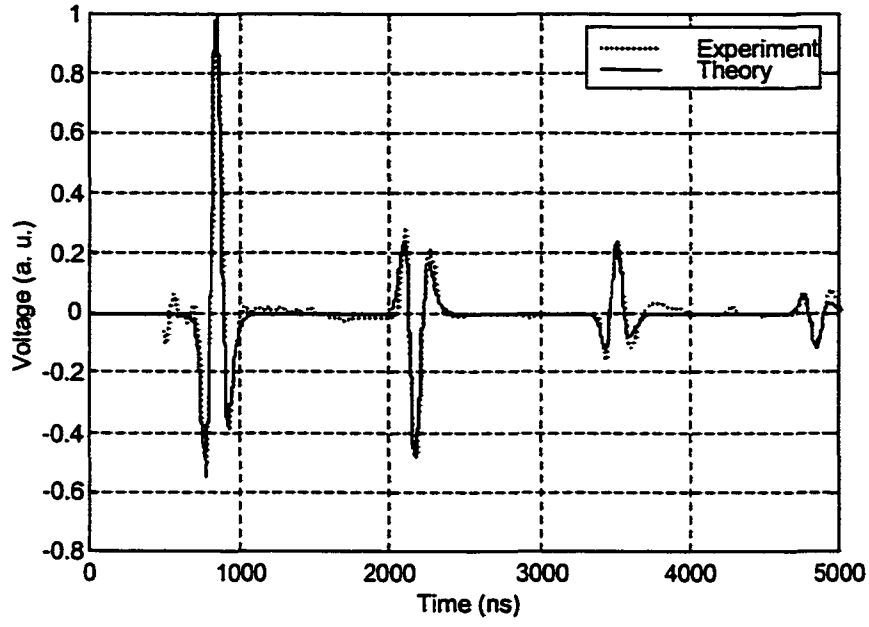


Fig. 4.6. Experimental and theoretical results from a 1.5mm-thick PVC sample by the diode laser. For the theoretical calculation, laser pulse width $\tau_L$ = 101ns, optical absorption $\alpha$ = 28mm$^{-1}$, and acoustic attenuation $\beta = 0.17\text{mm}^{-1}$.

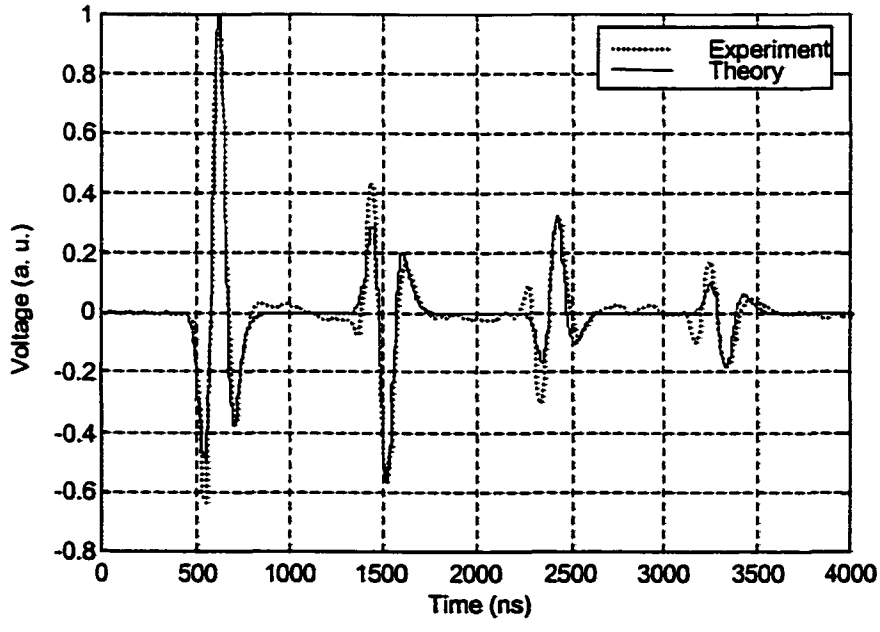


Fig. 4.7. Experimental and theoretical results from a 1mm-thick PVC sample by the diode laser. For the theoretical calculation, laser pulse width $\tau_L$ = 101ns, optical absorption $\alpha$ = 28mm$^{-1}$, and acoustic attenuation $\beta = 0.17\text{mm}^{-1}$.

The high attenuation is due to the long molecular chain of PVC material. PVC (polyvinyl chloride) is a thermoplastic polymer. Its molecular unit is [57]

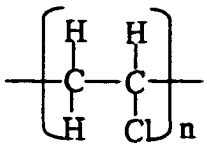


where n=500~1500. The chain size ranges from 50 to 500 microns. PVC belongs to linear class polymers. Unlike crystalline structures, the arrangement of the chains is almost entirely random (Fig. 4.8). There are no primary forces holding neighboring chains together. This arrangement shows that PVC is isotropic material. The energy relaxation is along the molecular chain, and thus, can be any direction. This explains that the attenuation of PVC is much larger than the attenuations found in crystalline materials. No other experiments measuring the acoustic attenuation constant of PVC were found. The measured attenuation constants of some other polymers have the same scale as our measurement of PVC [75].

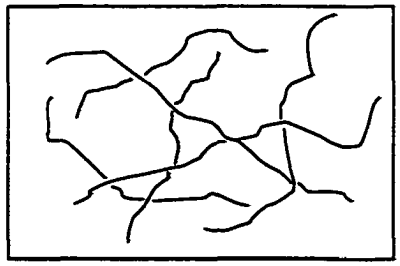

Fig. 4.8. The arrangement of PVC molecular chains.

After successfully interpreting the experimental results involving a single sample, we are able to extend our computation to the case where a multi-layered sample is used. Fig.

4.9 shows the results for a two-layer sample from both experiment and calculation. As illustrated in Fig. 4.10, the first layer irradiated by the diode laser has a thickness of 1.0mm. The second layer, adjacent to the transducer, has a thickness of 0.5mm. Both layers are PVC and are adjoined by a thin layer of grease. This experiment is set to check the computation model for the multi-layered structure and is also a good illustration of crack detection by ultrasonic technique. The theoretical calculation is in good agreement with the experimental result. They clearly show that pulse 2 and pulse 3 are due to the discontinuity between the two pieces of samples by comparing this result with the result obtained from one single-piece sample with a thickness of 1.5mm (see Fig. 4.6). Fig. 4.10 also shows how these echoes are originated.

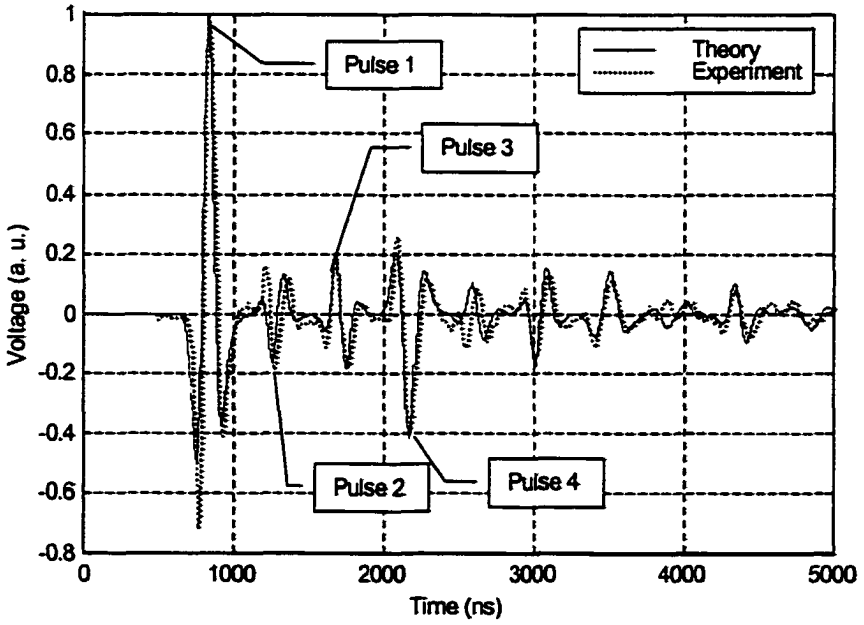


Fig. 4.9. Experimental and theoretical results from a two-layer sample by the diode laser. The first layer is 1mm thick and the second layer is 0.5mm thick. Both layers are PVC and they are coupled by a thin grease layer.

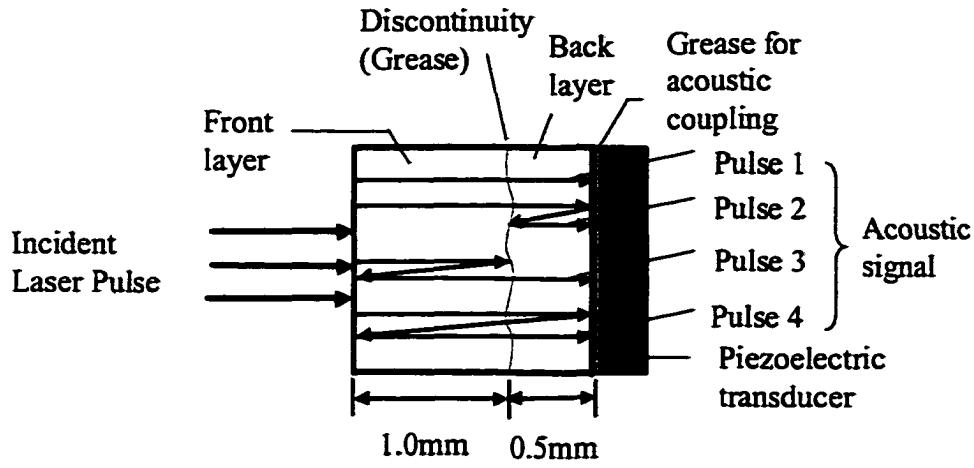


Fig. 4.10. Schematic of the generation of the pulse sequence observed in Fig. 4.9. Additional echoes (pulses 2 and 3) appear due to the reflections at the discontinuity.

**B. OA results with the nitrogen laser**

The OA experiments by the diode laser were actually laser pulse width limit (see the discussion in Chapter II, section 2.1.1.A) since the pulse width is about 100ns. Therefore, the pulse profile itself can be used as an approximation of the initial acoustic displacement signal and yields a reasonably good agreement between the theory and the experiment. However, this is not true for the experiment involving the nitrogen laser that has a pulse width of 2ns. Fig. 4.11 gives the results from a 1.5mm PVC sample induced by the nitrogen laser. If only the laser pulse profile is used to calculate the signal, then the theoretical signal pulse width is much narrower than the experimental one. The theoretical result shown in Fig. 4.11 was obtained by assuming the optical absorption coefficient $\alpha = 87\text{mm}^{-1}$, which is a result from Chapter VI. It is seen from Fig. 4.11 that the pulse widths from both the experiment and the theory are in reasonable agreement.

This provides a way to validate the spectral ratio theory that will be discussed in Chapter VI for the measurement of the optical absorption coefficient.

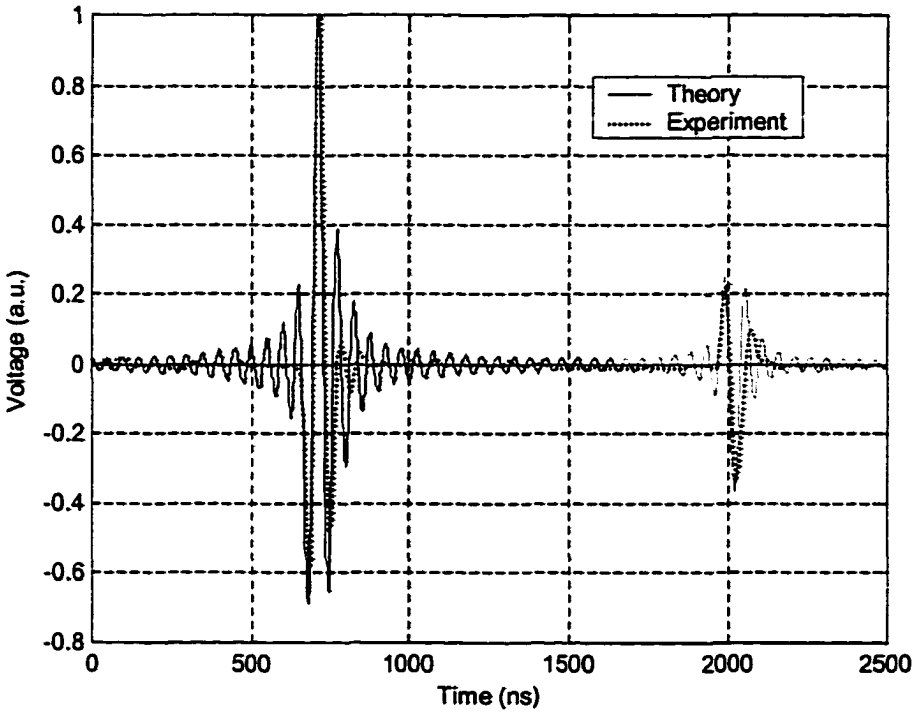


Fig. 4.11. Experimental and theoretical results from a 1.5mm-thick PVC sample by the nitrogen laser. For the theoretical calculation, laser pulse width $\tau_L$ = 2ns, optical absorption $\alpha$ = 87mm$^{-1}$, and acoustic attenuation $\beta$ = 0.25mm$^{-1}$.

The theoretical signal has more oscillations than the experimental one. This is because the center frequency of the signal is higher than the one induced by the diode laser. This center frequency now is closer to the resonant frequency of the piezoelectric transducer. In practice, the manufacturer has taken special treatment to reduce this oscillation.

The acoustic attenuation coefficient $\beta$ used here is 0.25mm$^{-1}$, which is different from the previous experiment. There are two reasons that may account for this change. First,

the center frequency of the OA signal has increased, for which one expects higher acoustic losses. Second, the dimension of the laser spot has changed, which results in a different diffraction loss. Unfortunately, we have not been able to measure the size of the laser spot.

**C. OA results with the passivation light**

Fig. 4.12 shows the experimental and theoretical results with a 1.5mm PVC sample and the passivation light. The results are similar to those obtained by the nitrogen laser, since the light pulse width (11ns) is also narrow. Therefore, the contribution of the absorption length cannot be neglected. Here $\alpha = 34\text{mm}^{-1}$ has been used for calculation. Also, the theoretical signal shows some oscillations. Comparing with the experiment result with the nitrogen laser, the acoustic pulse for this experiment is wider. Therefore, there are fewer oscillations, and the acoustic losses are smaller ($\beta = 0.19\text{mm}^{-1}$).

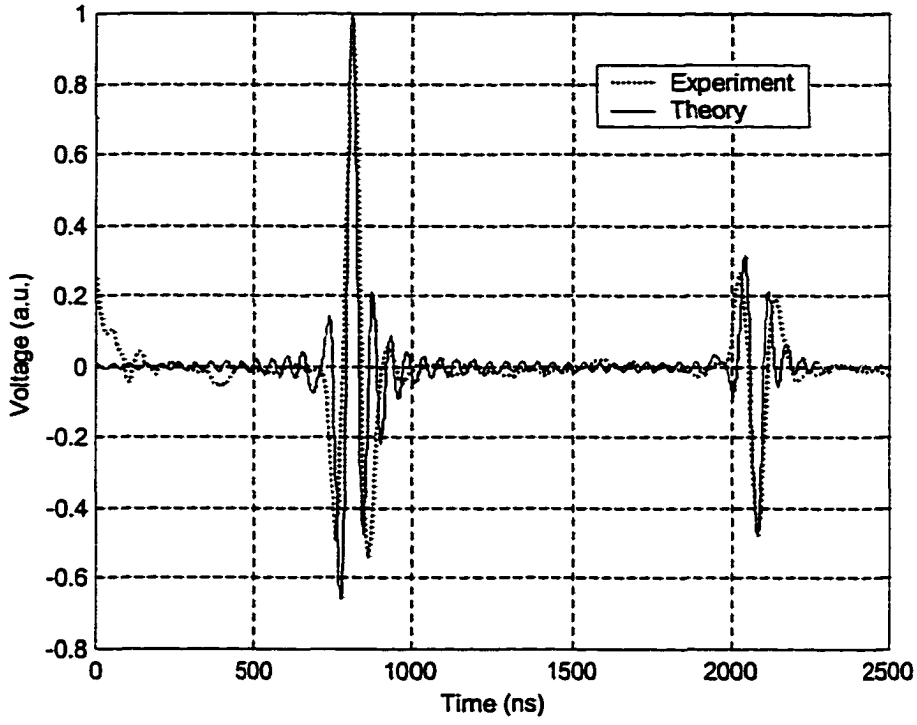


Fig. 4.12. Experimental and theoretical results from a 1.5mm-thick PVC sample by the passivation light. For the theoretical calculation, laser pulse width $\tau_L$ = 11ns, optical absorption $\alpha$ = 34mm$^{-1}$, and acoustic attenuation $\beta$ = 0.19mm$^{-1}$.

## D. OA results by the Nd:YAG laser

Fig. 4.13 shows the OA signals with a 1.9mm PVC sample and the Nd:YAG laser. These results are similar to those obtained by the diode laser, since the laser pulse width (54ns) is also wide. No obvious oscillation of the signal is seen. However, the influence from the absorption region still cannot be neglected. We have not done experiments to measure the optical absorption coefficient $\alpha$. From the trend of the coefficients for PVC at three other wavelengths, we expect $\alpha$ at 1064nm is in the order of $10^1$mm$^{-1}$ but less than 28mm$^{-1}$ which is the value for $\alpha$ at 880nm. We found that by assuming $\alpha$ = 10mm$^{-1}$, the theoretical pulse has the pulse width close to the experimental one.

For the acoustic losses, we expect the value of $\beta$ is smaller than that for the previous experiments since the acoustic pulse width is wider. However, the experiment turned out that $\beta = 0.26\text{mm}^{-1}$, which is quite larger than the previous result. The diffraction losses for this experiment may have increased.

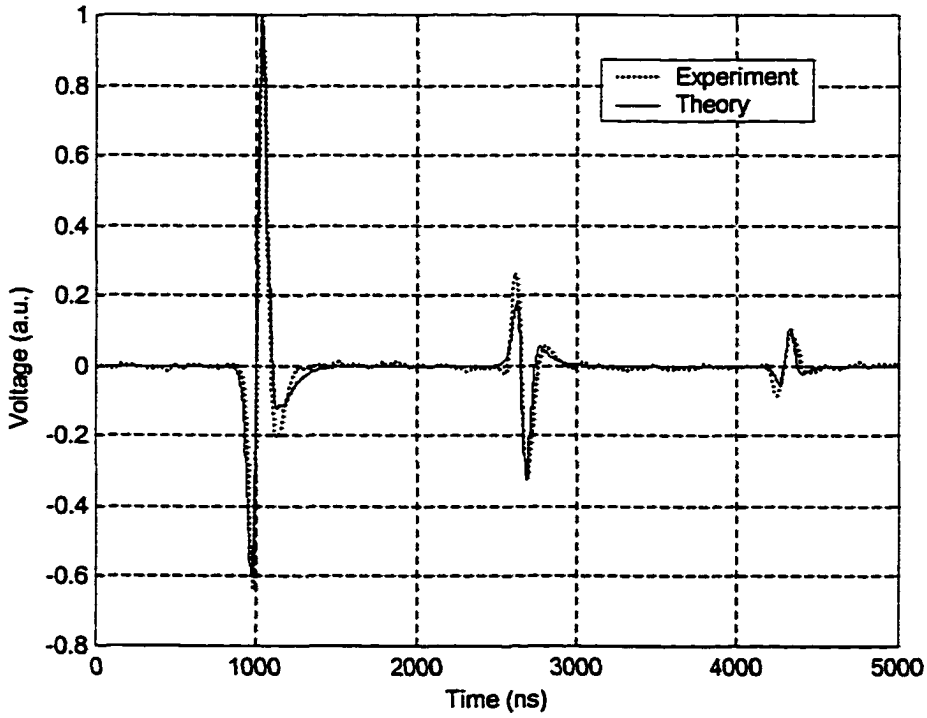


Fig. 4.13. Experimental and theoretical results from a 1.9mm-thick PVC sample by the Nd:YAG laser. For the theoretical calculation, laser pulse width $\tau_L = 54\text{ns}$, optical absorption $\alpha = 10\text{mm}^{-1}$, and acoustic attenuation $\beta = 0.26\text{mm}^{-1}$.

### 4.2.2. Noncontact detection on PVC sample pumped with Nd:YAG laser

We have used a probe laser to measure the indirect OA signal in air due to the absorption of the pump laser in the solid sample. We also have used the method developed in the previous chapter to model this indirect OA signal. The results and the comparison are given in this section.

The probe beam has been placed in various positions in order to investigate the acoustic attenuation in air. The signals as well as the estimate of the attenuation are also presented here.

**A. Model of the indirect OA signal in air**

As calculated in Chapter III and shown in Fig. 3.20, the indirect OA pressure signal in the air induced by a laser impulse is also like an impulse but with a long slowly decaying tail. Therefore, for an experiment pumped by a laser with finite pulse width, the indirect pressure signal should have a profile close to the laser pulse. The Nd:YAG laser that we used to generate the OA signal has a pulse width of 54ns. The computed indirect pressure signal in the air is shown in Fig. 4.14, in which the laser pulse profile is also given as a comparison to the pressure signal. The figure shows that the main portion of the pressure signal follows the profile of the laser pulse, but it decays slowly. This is due to the thermal diffusion in air.

Knowing the pressure in the air, theoretically the beam deflection anger $\delta$ can be calculated from Eq. (3.32) in Chapter III. An ideal position sensor should give a signal which follows the profile of $\delta$, which is a time derivative of the pressure signal. However, the probe beam always has a finite geometric dimension. Since the acoustic velocity in air is much slower, the transition time for the acoustic signal to pass through the probe beam cannot be neglected. For instance, if the probe beam has a diameter of $2a = 100\mu m$ (see Fig. 3.21), the corresponding acoustic transition time is 270ns assuming the sound speed is 366m/s. This time is much longer than the pulse width of the acoustic signal itself which is about 50ns. Consequently, the detected signal from the probe beam suffers

a tremendous broadening. This signal can be calculated from the convolution of $\delta$ and $f(x)/c_a$, where $f(x)$ is the spatial profile of the probe that normally is a Guassian function and $c_a$ is the sound velocity in air.

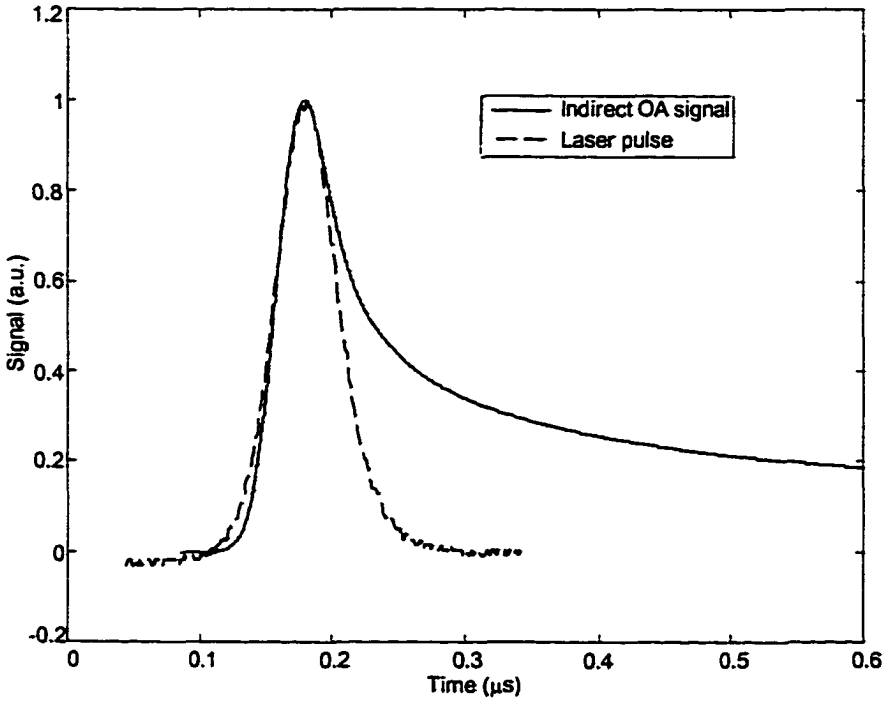


Fig. 4.14. The calculated indirect OA pressure signal in the air generated by the Nd:YAG laser. The main portion of the pressure pulse follows the profile of the laser pulse, but it decays slowly due to the thermal diffusion effect.

Another difficulty to model this detected signal comes from the knife-edge detection scheme that we actually used in our experiment. If the dimension of the probe beam can be neglected and the direction of the displacement of the probe on the knife-edge plane is perpendicular to the knife-edge, then the intensity change on the photodiode is proportional to $\delta$. However, the probe beam has a finite dimension and each portion of the probes is separately affected by the pressure signal. Hence, some of the deflection

may be completely blocked by the knife-edge. In addition, the relation of the orientation of the knife-edge and the direction of beam spot displacement on the knife-edge plane is unknown. These factors make it difficult to model the effect of the knife-edge, which is no longer a linear process.

In the experiment, we observed the broadening of the signal. We also observed that this broadening was a function of the dimension of the probe beam as one expects. The other important phenomenon that we noticed in the experiment was that the signal profile from the photodiode behind the knife-edge was close to the time derivative of the deflection angle. Therefore, we took a three-step approach to calculate the signal from the photodiode in response to the indirect pressure in the air: (1) calculate the indirect pressure signal, which has been done previously and the results has been shown in Fig. 4.14; (2) calculate the deflection signal as a convolution of the time derivative of the pressure signal and the profile of the probe beam $f(x)/c_a$; and (3) take the time derivative of the result from step 2 as an approximation of the final result from the photodiode.

Fig. 4.15 shows the comparison between the experimental result and the theoretical one that is yielded by the three-step approach. The probe beam was assumed to be Guassian and had a FWHM of 100μm. This value was estimated from the experiment. This comparison shows that the calculated signal has pulse width close to the experimental one. The first 700ns from both signals are also similar, and later the experimental one exhibits broadening. As another comparison, the theoretical signal assuming an infinitely small dimension of the probe beam is also shown in this figure. It can be seen that this is not a good approximation for a practical experiment.

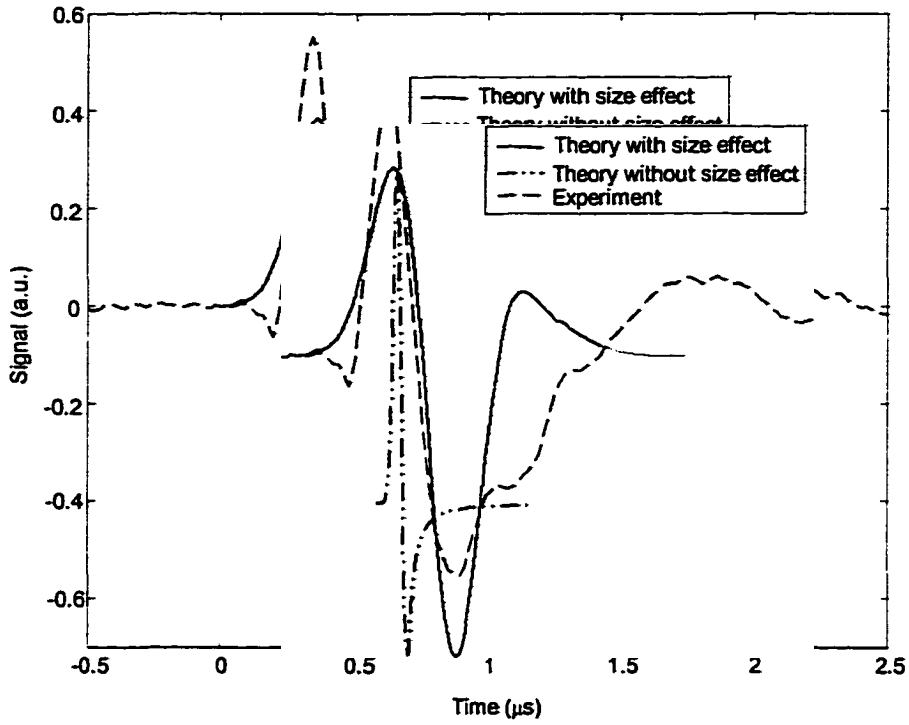


Fig. 4.15. Theoretical and experimental results from a probe beam with a spatial FWHM of 100μm. The blue one is the theoretical result considering the influence of the dimension of the probe beam. It has roughly the same pulse width as the experimental one. The black trace is the theoretical result assuming the probe beam is infinitely narrower.

We also use the above three-step approach to calculate the signal probed by a wider probe beam. This result, superimposed on the experimental one, is shown in Fig. 4.16. This experiment used a probe beam with a FWHM of 0.8mm, which corresponds to a transition time of 2.2μs for the acoustic wave to pass through it. In this case, the theory matches with the experiment quite well.

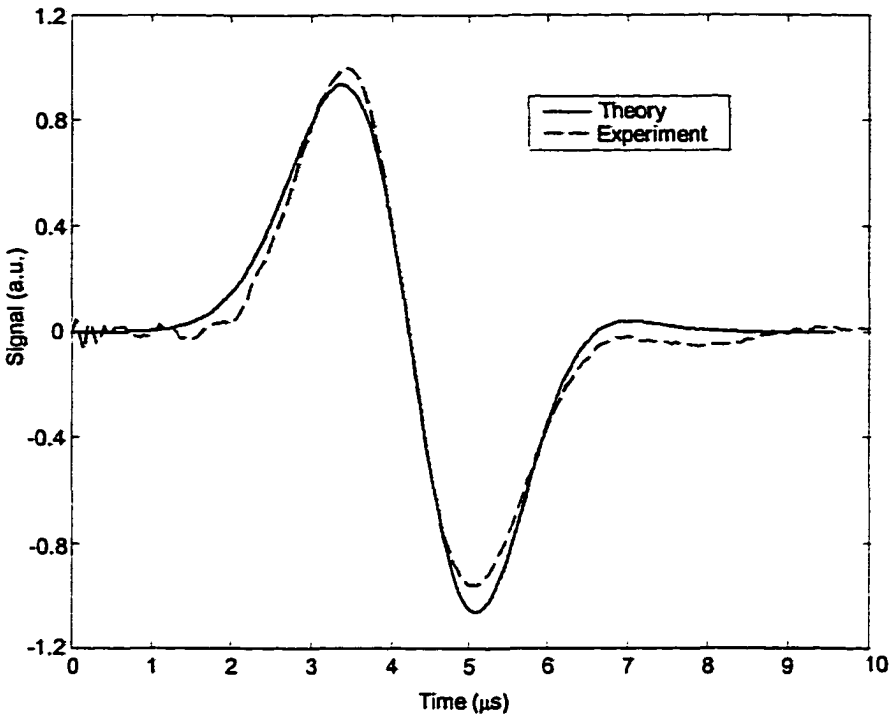


Fig. 4.16. Theoretical and experimental results from a probe beam with a spatial FWHM of 800μm.

## B. Acoustic attenuation in air

Using the experimental setup that has been discussed previously and shown in Fig. 4.4, and by varying the distance from the probe beam to the sample surface, we have observed acoustic attenuation as well as distortion. These experimental data can be used to give a quantitative measurement of the attenuation. Tam has used the similar apparatus to perform similar measurement [20]. In his experiment, the gas (pure $CO_2$ or a $CO_2$+$H_2O$ mixture) was confined in a chamber at a constant temperature environment. Our measurement is performed in the open air without any control of the environment.

Fig. 4.17 shows the indirect OA signal as a function of positions. The origin of the position axis was set to where the first signal was measured. Actually, it was about

0.5mm away from the solid sample surface. All the remaining signals were measured further way from the surface.

We took the peak value of the signal at each location as a representative of the signal amplitude. Then these peaks were normalized to the peak at position $x$=0. The effective acoustic attenuation coefficient can be obtained from the relation of the normalized signal amplitude and its corresponding position. Fig. 4.18 plots the logarithms of the peak amplitudes versus the position. The attenuation coefficient $\beta$ then is the absolute value of the slope. Our measurement yields $\beta = 0.48\text{mm}^{-1}$, i.e., the acoustic attenuation in air is 0.48 nepers/mm.

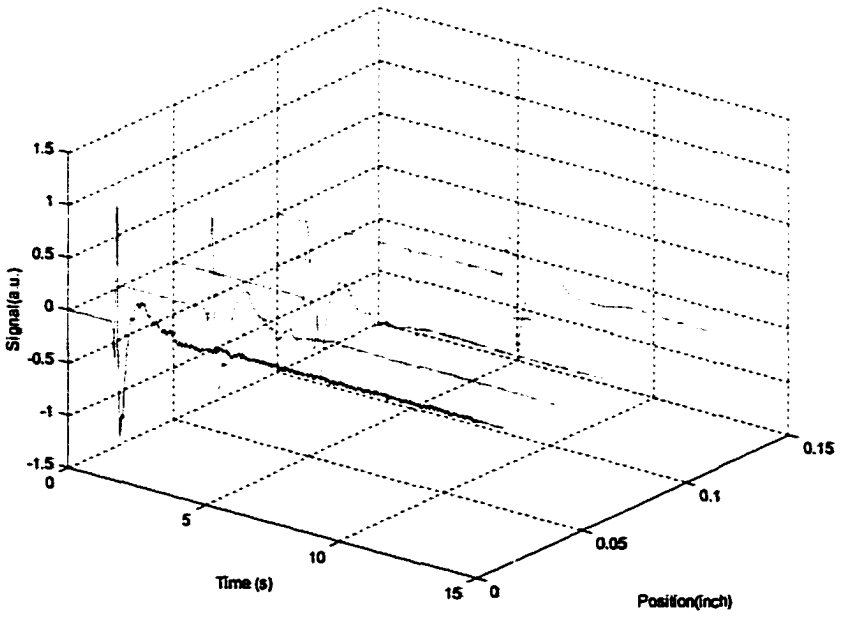


Fig. 4.17. Indirect OA signal in the air as a function of time as well as of position. The origin of the position axis was set to where the first signal was measured. The rest of the signals were measured further away from the sample surface.

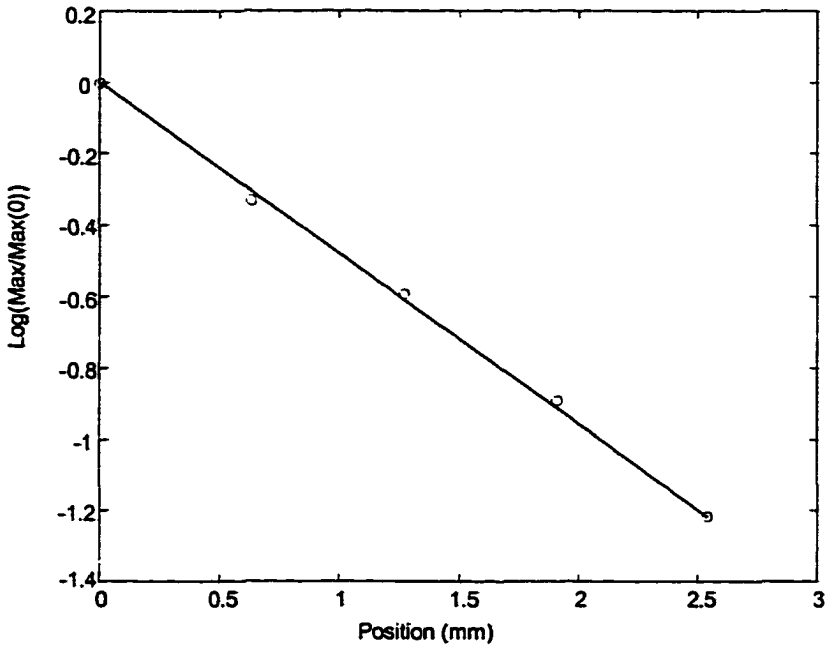


Fig. 4.18. Acoustic attenuation versus distance. The peak value from each OA signal at various locations has been compared with the peak at x=0. The acoustic attenunation coefficient β was measured from the slope to be 0.48mm$^{-1}$, i.e. 0.48nepers/mm.

The peak amplitude method can only give an estimate of the attenuation coefficient. The frequency dependent attenuation can be obtained by comparing the frequency spectra of signals at two locations. Fig. 4.19 gives the frequency dependent measurement by the spectral comparison method. The ratio of spectra magnitudes from two indirect signals at $x$ = 2.54mm and $x$ = 0 was used to yield the attenuation coefficient at a unit of nepels/mm. The trend of the frequency dependence of the attenuation in air is similar to that of pure $CO_2$ investigated by Tam [20].

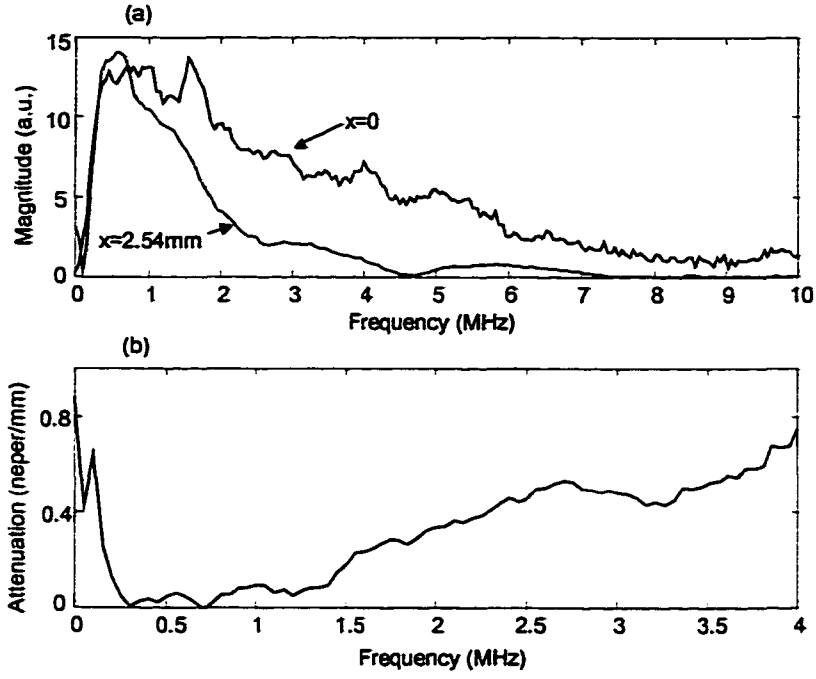


Fig. 4.19. Acoustic attenuation as a function of frequency. (a) Spectra of OA signals at $x$=0 and $x$=2.54mm. (b) Attenuation versus frequency. The attenuation was taken from the magnitude ratio of the spectra and converted to the unit of nepers/mm.

# CHAPTER V

# OPTOACOUSTIC SIGNAL PROCESSING BY THE FOURIER AND WAVELET TRANSFORMS

This chapter presents methods that we developed to treat optoacoustic experimental data. These include a Fourier transform method to measure echo interval in frequency domain and wavelet transform methods to interpret optoacoustic signals as well as to remove noise from experimental data. These methods have not been widely used previously to treat OA signals. The treatment here is general; therefore, it can be used in other applications also.

## 5.1. ECHO TIME MEASUREMENT FROM FREQUENCY SPECTRUM

### 5.1.1. Introduction

The measurement of acoustic pulse propagation velocity in any medium, or the measurement of the sample thickness, requires one be able to resolve the time separation between acoustic pulse echoes. To increase the accuracy of the measurement, one desires to record several echoes within one trace. This allows measurements of several intervals between echoes, which can then be averaged. In many experiments, however, where a digital scope is used (as for example in the experiments undertaken in this work), one is restricted to a fixed number of samples in a given run. In such a case, an increase in the

time window to include more echoes does not necessarily increase the accuracy of the measurement because of the concurrent loss in the resolution in the location of each echo.

Another reason for not taking a long sequence of echoes is that the acoustic pulse deforms along the path due to diffraction and dispersion. Consequently the location of the peak in each pulse may vary from early echoes to late echoes. Therefore, there is an advantage if one only measures the first two echoes, as long as one does not need to extract dispersion information.

Here we prove that the time separation between pulse echoes can be equivalently obtained in the frequency domain. This method is especially useful for an experimentally obtained time sequence where the time signal may suffer distortion by noise.

### 5.1.2. Principle

First assume that there is no distortion from the first to the second echo, but there is an attenuation of the second echo due to the transmission loss at the boundaries. Therefore, the signal can be illustrated as Fig. 5.1, and it can be expressed as

$$s(t) = f(t) + k_1 f(t - T), \tag{5.1}$$

where $f(t)$ describes the profile of the first echo only, $T$ is the separation between these two echoes and $k_1$ is the attenuation factor whose absolute value is less than one.

The Fourier Transform of Eq. (5.1) is:

$$S(\omega) = F(\omega)(1 + k_1 e^{-j\omega T}). \tag{5.2}$$

Hence, the magnitude of $S(\omega)$ is

$$|S(\omega)| = |F(\omega)|(1 + k_1^2 + 2k_1 \cos(\omega T)). \tag{5.3}$$

Fig. 5.2 plots the magnitude $|S(\omega)|$ of $s(t)$ shown in Fig. 5.1. It is an amplitude modulation of the spectrum of the arbitrary pulse $f(t)$. The period of the frequency modulation is $1/T$. Therefore, by measuring the period at the spectrum of signal $s(t)$, one is able to get the time separation between two echoes.

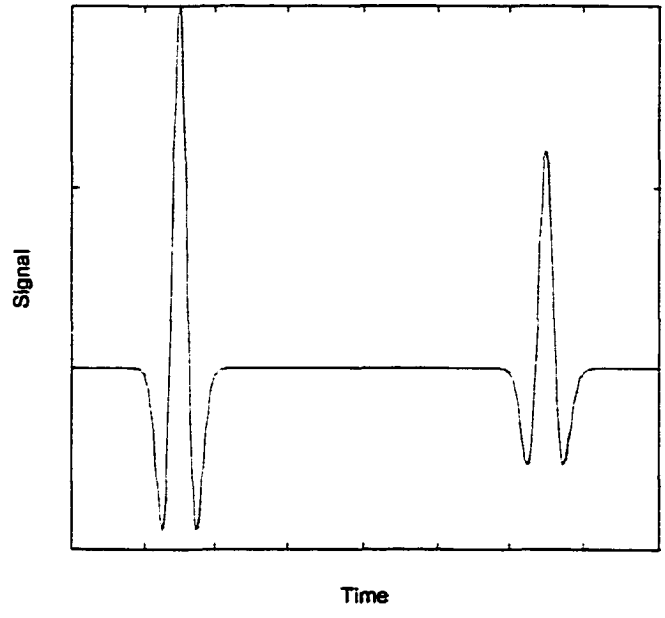


Fig. 5.1. An ideal echo pair used in the theory. The second echo is assumed to be identical to the first one except the magnitude is smaller due to the transmission loss at the boundary.

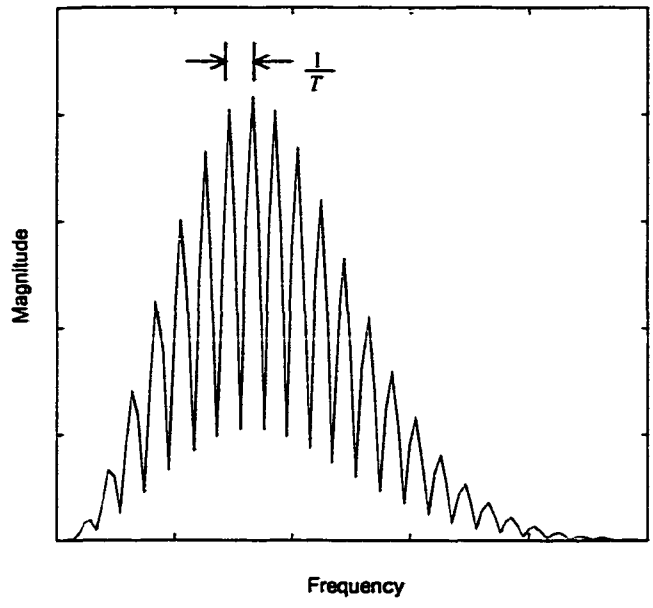


Fig. 5.2. The Fourier transform of the signal shown in Fig. 5.1. The period of the frequency modulation yields the separation between the echoes of the time signal.

When $1/T$ is smaller than the bandwidth of signal $f(t)$, there is more than one cycle of the modulation within the bandwidth. (The smaller of $1/T$ compared to the bandwidth, the more number of cycles.) In the ideal case where the second echo does not exhibit distortion in the shape, taking one measurement or average of several measurements of the modulation period makes no difference since both yield the accurate time separation $T$ without any error. Also, in this case, there is no difference in taking the measurement of $T$ whether in frequency domain or directly in time domain.

However, in practice the time signal in an experimental environment will suffer distortion due to the inherent dispersion and all kinds of unavoidable noise. This makes the measurement of $T$ in time domain inaccurate and sometimes difficult. For instance, the peak-to-peak or center-to-center or some other criterion can be used as a

measurement of $T$. Taking different criteria may give different results from the same signal, and thus generate ambiguity.

The Fourier transform of a pair of distorted echoes results in the fluctuation of the modulation period. However, separation $T$ can be more accurately obtained by taking the average of several measurements of the modulation period as long as the condition that $1/T$ is much smaller than the bandwidth of signal $f(t)$ is met.

The advantage of this Fourier transform method comes from the feature that this method utilizes the whole signal of each echo, while the direct measurement in time only takes a pair of points from consecutive echoes. Note that the Fourier Transform of a time sequence that contains more than one echo will not give the spectrum of each echo because the result from the transform exhibits interference. Therefore, the Fourier transform cannot be used if one needs to analyze the spectrum of each echo. Instead, one needs to utilize short time Fourier transform or wavelet transform which will be discussed in section 5.2.

### 5.1.3. Application to optoacoustic signals

Fig. 5.3 is the signal of one OA experiment done on a tissue sample. The pump laser was the nitrogen laser, and the OA signal was picked up at the other side of the sample by the 20MHz piezoelectric transducer (The experiment setup has been described in Chapter IV). It can be seen that the background noise is not trivial in this experiment. Also, there is considerable distortion in the second echo. For instance, the negative peak is not at the negative center for the second echo. A direct peak-to-peak measurement in time domain

yields the separation between the echoes to be 6.06μs. It is hard to estimate the error of this measurement because there is only one measurement.

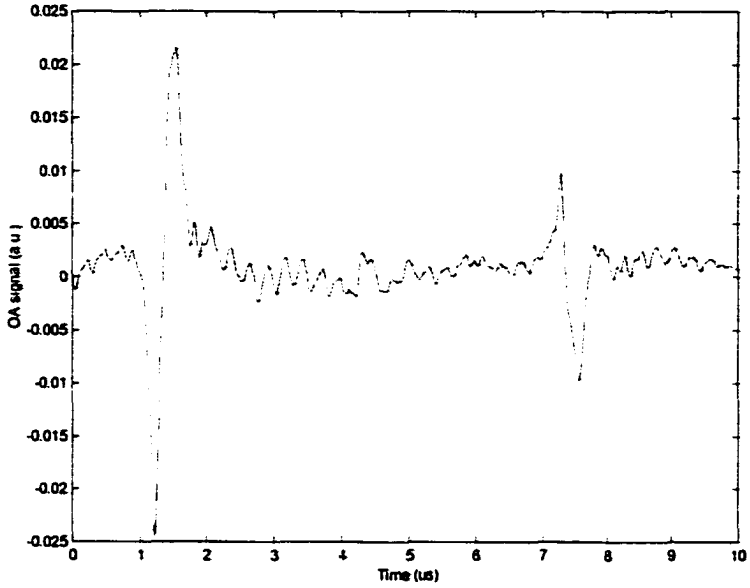


Fig. 5.3. An OA experimental result from a tissue sample excited by the nitrogen laser.

Fig. 5.4 is the Fourier transform of the OA signal. The average modulation period based on 30 measurements was 0.1632MHz. The variance of the measurement was calculated to be 0.0080MHz. Therefore, the measurement of the time separation using the Fourier transform method was 6.13±0.31μs.

From this example one can see that the results from the direct measurement in the time domain and from the calculation in the frequency domain are very close. For this example the difference in these results is about 1%. However, the measurement from the frequency spectrum has a higher confidence level and the variance can be easily determined.

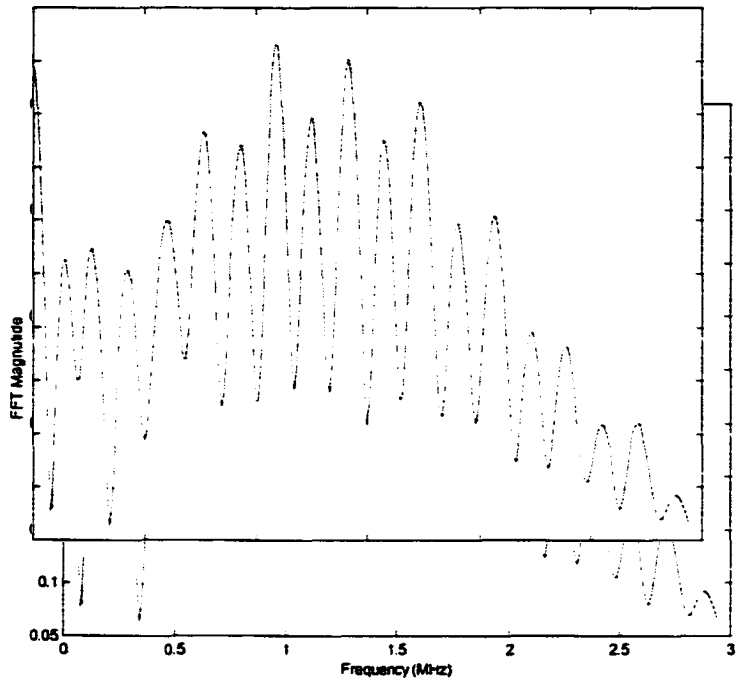


Fig. 5.4. Fourier transform of the OA signal shown in Fig. 5.3. The average of the modulation period is used to calculate the time separation between echoes.

## 5.2. ECHO SEPARATION BY WAVELET TRANSFORM IN TIME-FREQUENCY SPACE

### 5.2.1. Introduction to wavelet transform

Mathematical transformations use basis functions that satisfy certain mathematical requirements to represent data in another space. By the transformation method, one has another representation of data and gains a new (and maybe powerful) tool to analyze data. Among all these transforms, The Fourier transform is the one that has been most commonly used. However, the wavelet transform developed in the past 10-20 years has shown many advantages over the Fourier transform, and has found applications in many areas.

By using the Fourier transform, one gains the frequency information of a signal but loses the time information. For example, two completely different time signals may have the same power spectrum by the Fourier transform. Generally the Fourier transform can be only applied to a stationary signal. For a non-stationary signal, one usually desires to obtain the frequency contents varying with time. For this purpose the short time Fourier transform (STFT) was used before.

The idea of STFT is to frame the original signal into pieces by using a time window, and then to apply the Fourier transform to each piece. Therefore, the STFT yields both the time and frequency information of a non-stationary signal. One can plot the result from the STFT in a time-frequency space. Note that the frequency contents obtained by STFT correspond to the entire time window but not to a specific time location, and also the frequencies are not accurate. The uncertainty of the frequencies are related to the width of the window and governed by the uncertainty principle. The wider the time window is, the more accurate the results are in the frequency domain, but the less accurate they are in the time domain. To analyze a signal, one desires to get high frequency resolution in the low frequency region and high time resolution in the high frequency region. Thus, a dynamic window size is required, which is not provided by the STFT because the width of the window is fixed.

In summary, to analyze the frequency contents of a non-stationary signal, a transform is required to present this signal in a time-frequency space. In addition, multiresolution results balanced by the uncertainty of time and frequency are desired. The wavelet transform is the ideal candidate for such purposes.

The wavelet transform has two unique features that often make it more useful than other transforms, especially the Fourier transform. First, in wavelet analysis, large windows are used to look at gross features, and small windows are used to look at the finer features. The selection of the window size is performed automatically without the user's intervention. Second, the basis function set used in a wavelet transform can have a variety of forms as long as they meet certain mathematical requirements, while each of the other transforms has its own unique basis function; for example, the Fourier transform uses sinusoid functions to represent a signal. The choice of basis function is really determined by the data to be represented and the application. If the best wavelets are adapted to the data, or if the coefficients are truncated below a threshold, the data can be sparsely represented. This sparse coding makes the wavelet transform an excellent tool in the field of data compression and signal denoising.

Because of its prominent features, the wavelet transform has gained many applications in the applied fields. Besides data compression and signal denoising, other applications include sub-band coding, signal and image processing, magnetic resonance imaging, speech discrimination, earthquake-prediction, as well as solving partial differential equations. This section introduces the wavelet transform and the concept of time-frequency window, followed by the application of time-frequency localization to our experimental data. In the next section the procedure of signal denoising will be given, followed by denoising demonstrations applying this method to our optoacoustic experimental results.

### 5.2.2. Wavelet transform and time-frequency localization

In this section, the short time Fourier transform is first briefly described. Then we discuss the wavelet transform and its varying time-frequency window. This is followed by a comparison between these two transforms.

In STFT, a time-localization window $\phi(t-b)$ can be used to segment the signal, and then the Fourier transform of the short time signal is taken. Here, $b$ is the sliding parameter because it determines temporal location of the window. The window is also called "time-frequency" window because a time window sliding along the time axis is equivalent to a frequency-localization window sliding along the frequency axis. This can be seen from the definition of the STFT:

$$\begin{aligned}(G_\phi f)(b,\xi) &= \int_{-\infty}^{\infty} f(t)e^{-j\xi t}\phi(t-b)dt \qquad \text{(time-localization)} \\ &= \frac{e^{-jb\xi}}{2\pi}\int_{-\infty}^{\infty}\hat{f}(\omega)e^{jb\omega}\phi^*(\omega-\xi)d\omega \quad \text{(frequency-localization)},\end{aligned} \tag{5.4}$$

where $f$ is the signal, $b$ and $\xi$ are used to localize the time and frequency respectively. The carat represents the Fourier transform of the appropriate function, and the star denotes the complex conjugation.

The uncertainty principle governs the product of the widths of the time window and the frequency window, i.e.,

$$\Delta_\phi \Delta_{\hat{\phi}} \geq \tfrac{1}{2}, \tag{5.5}$$

where $\Delta_\phi$ is the width of the time window $\phi$ and $\Delta_{\hat{\phi}}$ is the width of its Fourier transform, i.e., the frequency window $\hat{\phi}$. For the Fourier transform, the width of the time window is

infinite so that the width of the frequency window shrinks toward zero. Therefore, the spectrum is accurate to each single frequency.

The widths of the time and frequency windows in a STFT are fixed (Fig. 5.5). However, it is desired to have a wide time-window to analyze low frequencies thoroughly and a narrow window to locate high frequencies more precisely. Unfortunately, STFT does not have such automatic zoom-in and zoom-out capability. On the other hand, the wavelet transform does.

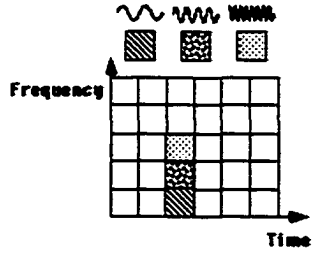


Fig. 5.5. Fourier basis functions and time-frequency windows of the STFT [76].

The definition of the wavelet transform is similar to that of the STFT. It can be expressed as:

$$(W_\psi f)(b,a) = \frac{1}{\sqrt{a}} \int_{-\infty}^{\infty} f(t)\psi^*(\frac{t-b}{a})dt. \tag{5.6}$$

Here $\psi(t)$ is the basic wavelet, $b$ is a translation parameter that represents a shift in time, $a$ ($a > 0$) is the dilation parameter representing a frequency shift, and $(W_\psi f)(b,a)$ is the wavelet transform coefficient indexed by $b$ and $a$.

A basic wavelet $\psi(t)$ must meet certain conditions. Namely, $\psi(t)$, $|t|^{1/2}\psi(t)$ and $t\psi(t)$ must be in $L^2$ and $\hat{\psi}(0)=0$. These conditions indicate that the wavelet $\psi(t)$ is a bandpass filter.

The translation parameter $b$ slides the time window along the entire time axis. The time-window function $\frac{1}{\sqrt{a}}\psi(\frac{t-b}{a})$ is given by

$$[b+at^{*}-a\Delta_{\psi}, b+at^{*}+a\Delta_{\psi}], \tag{5.7}$$

where $t^{*}$ and $\Delta_{\psi}$ are the center and the width of the basic wavelet $\psi(t)$, respectively. The width of this time window $\frac{1}{\sqrt{a}}\psi(\frac{t-b}{a})$ is therefore $2a\Delta_{\psi}$.

It can be seen that the wavelet transform also works as a frequency windowing of the spectrum of the signal. It can be obtained from the Parseval identity that

$$(W_{\psi}f)(b,a)=\frac{\sqrt{a}}{2\pi}\int_{-\infty}^{\infty}\hat{f}(\omega)e^{-jb\omega}\hat{\psi}^{*}(a\omega)d\omega. \tag{5.8}$$

Therefore, $a$ slides the frequency window along the positive frequency axis. The frequency window is given by

$$[\frac{1}{a}(\omega_{+}^{*}-\Delta_{\psi}^{+}), \frac{1}{a}(\omega_{+}^{*}+\Delta_{\psi}^{+})], \tag{5.9}$$

where $\omega_{+}^{*}$ and $\Delta_{\psi}^{+}$ are the center and the width of $\hat{\psi}$, i.e., the Fourier transform of the basic wavelet $\psi(t)$, respectively. The width of the frequency window $\frac{\sqrt{a}}{2\pi}\hat{\psi}^{*}(a\omega)$ is therefore $\frac{2}{a}\Delta_{\psi}^{+}$. The scale parameter $a$ not only locates the frequency window but also determines the width of this window. To map $a$ to an exact frequency, one may consider

$$a\rightarrow\xi=\frac{c}{a} \quad \text{for some } c>0. \tag{5.10}$$

The constant $c$ is called a calibration constant in frequency units. It is dependent on the wavelet basis, and can be obtained by applying the wavelet transform to a sinusoidal signal with a known frequency.

Now we can see the differences of the STFT and the wavelet transform. As mentioned above, the widths of both the time window and frequency windows of a STFT transform are rigid. However, for a wavelet transform the value of $a$ decreases when it locates a higher frequency $\frac{2}{a}\Delta_{\hat{\psi}}^{+}$, which corresponds to a narrower time window with width $2a\Delta_{\psi}$, and vice versa. Thus, the wavelet transform has automatic zoom-in and zoom-out capabilities. This relation is shown in Fig. 5.6. Note that the product of the widths of the time-window and the frequency-window remains constant and obeys the uncertainty law, i.e.,

$$\Delta_{\psi}\Delta_{\hat{\psi}} > \tfrac{1}{2}. \tag{5.11}$$

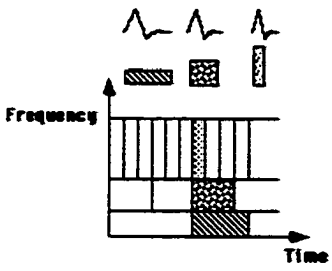


Fig. 5.6. Daubechies wavelet basis functions and time-frequency window of the wavelet transform [76].

Eq. (5.6) actually defines an integral wavelet transform (IWT) or continuous wavelet transform (CWT). The CWT coefficients can be obtained in a discrete formulation as the following equation [77]:

$$W_{\psi}(b,a)=\left(\frac{\delta t}{a}\right)^{1/2}\sum_{b'=0}^{N-1}x_{b'}\psi^{*}\left[\frac{(b'-b)\delta t}{a}\right], \tag{5.12}$$

where $x$ is the time sequence with $N$ samples, $\delta t$ is the sampling period, and $b$ and $b'$ are the indexes. Normally the time window slides along the time axis one sample a time, therefore, for a given dilation $a$ there are $N$ CWT coefficients. It is convenient to compare the transformed signal with the original signal if both have the same length. The other more important reason is that (forward and inverse) fast Fourier transform algorithm can be used to evaluate Eq. (5.12) and yields $N$ coefficients for a given $a$ simultaneously and efficiently [77].

In the calculation of CWT coefficients, the dilation parameter $a$ is also discrete. Although the value of $a$ can be arbitrary, it is often chosen to increase as the power of two. The details of how to select this parameter can be found in many references such as [77]. (Note that the inverse of $a$ is proportional to the frequency.) Such a choice guarantees higher resolutions in lower frequencies and lower resolutions in high frequencies.

From the process of the CWT calculation, one should see that CWT adds lots of redundancies into the transformed signal. More redundancies usually help the user to more easily interpret the data. Also, the plot of CWT in the time-frequency space has higher resolutions than that of discrete wavelet transform, which is briefly introduced below.

The CWT is often used for applications, such as time-frequency localization, because of the resolution and redundancy. However, the amount of computation is large. To overcome this difficulty, a discrete wavelet transform (DWT) can be used. This can be

obtained by evaluating the time sequence at the position $b = k/2^j$ with binary dilation $a = 2^{-j}$, where $j$ is an integer. It can also be conveniently calculated by utilizing quadrature filters (a pair of complementary low-pass and high-pass filters) and down-sampling technique (up-sampling for the reconstruction) [78]. The number of DWT coefficients is the same as the number of the time samplings, but the calculation of DWT is much faster.

In most practical applications, the DWT has a large number of coefficients that are zero or in small value if the wavelet basis set is properly chosen. Therefore, a signal can be sparsely represented by its DWT by ignoring these small or zero coefficients. When it is necessary, then, the signal can be reconstructed without any substantial loss in fidelity by padding zeros to the transformed sequence for the purposes of the inverse DWT. This technique has been widely used for data and image compression. Note that for DWT, orthogonal wavelet bases are often used for the convenience of reconstruction, while such bases are not possible to be applied to CWT [79].

### 5.2.3. Time-frequency localization method for echo separation of OA signals

To compare the wavelet transform and the short time Fourier transform, a clean and simple signal taken from our optoacoustic experiments was used to test the localizability of the STFT and the wavelet transform. The results show that the wavelet transform yields better time-frequency resolution. We apply the wavelet transform to some of our other OA experimental results. We show that, in addition, the wavelet analysis can be a powerful tool to identify different *acoustic modes* within a solid sample.

Fig. 5.7 shows an OA signal in time domain and its STFT. The OA signal was the result with the diode laser upon a PVC specimen, which has been present in the previous chapter. Note that all experimental signals were sampled by the digital scope. This chapter deals with the data processing, the absolute value of the time is not important. Therefore, all time axes in the figures presented in this chapter by default are labeled by the sample sequence unless other units are specified. Also, the frequency axes are not calibrated since we are only interested in their relative values. The time sequence that we use as an example has 499 samples and includes four acoustic echoes (pulses). The width of the time-window for the STFT was 64. This window slides along the time axis one sample a time. For the convenience of comparison, power spectra are plotted for all transforms. The power spectrum is shown in Fig. 5.7 by the contour plot where the inner contour represents the higher power. Another three-dimensional plot of the same STFT is shown in Fig. 5.8 for the better visual effect. With the aid of the STFT, the four echoes are separated in the time-frequency space.

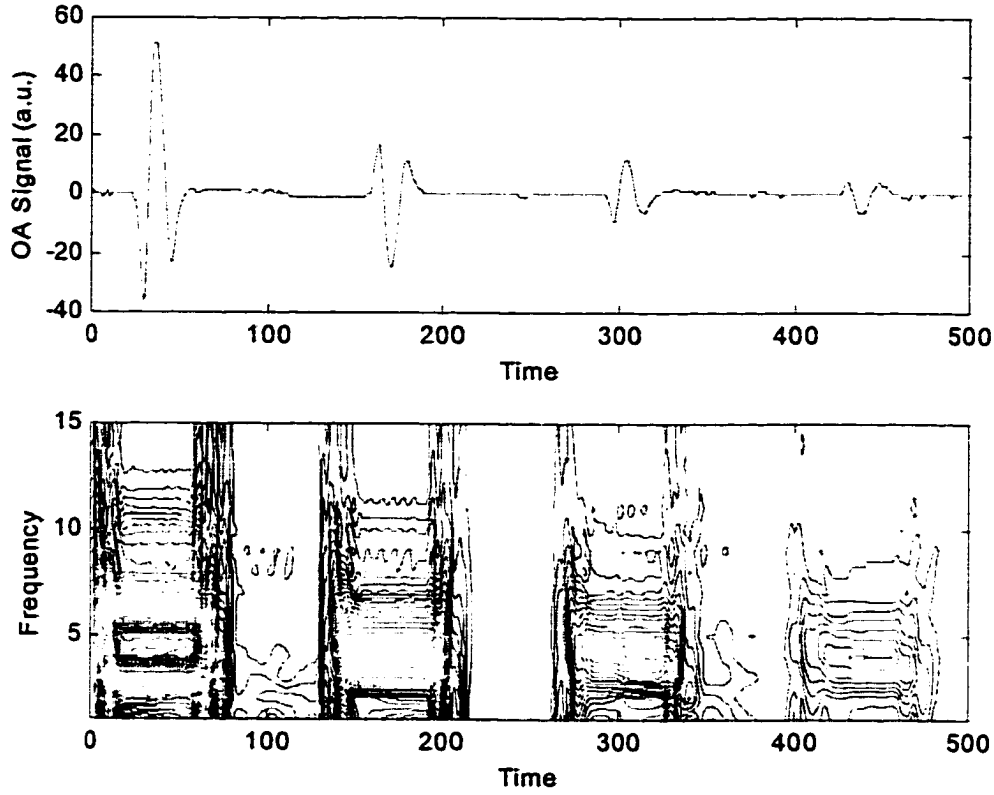


Fig. 5.7. An OA time signal and its STFT transform. The time axes are numbered by samples. The frequencies are not calibrated. The larger number means the higher frequency. The time window slides one sample a time.

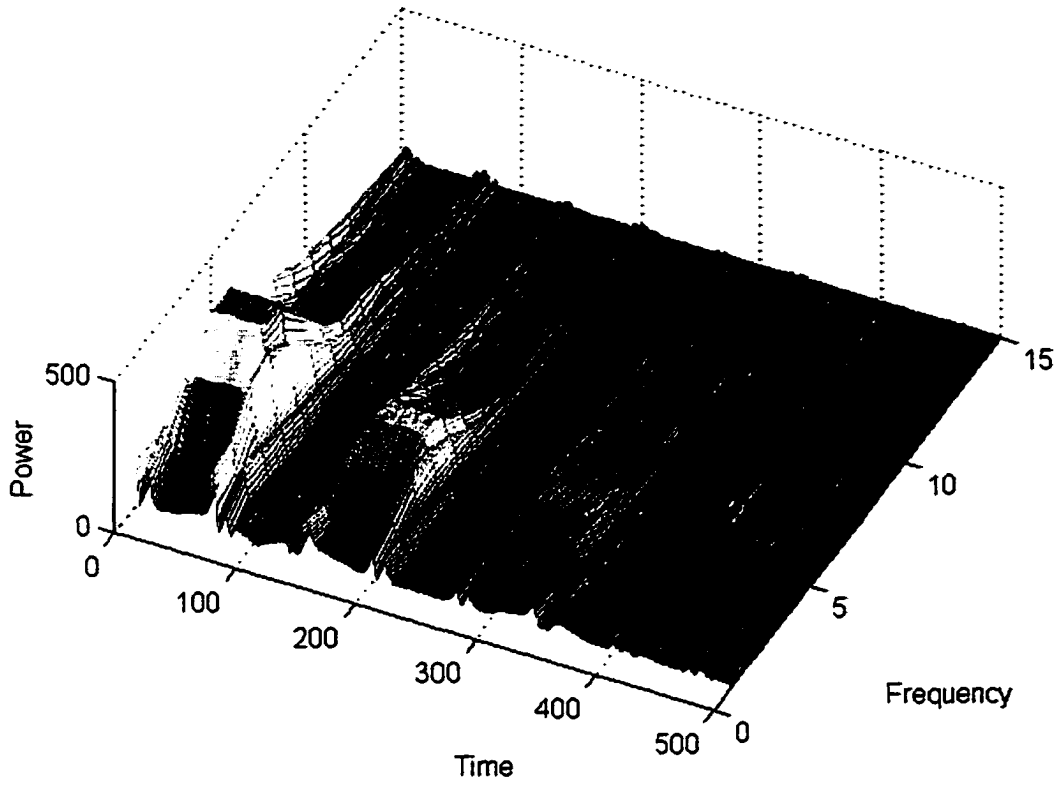


Fig. 5.8. Three-dimensional representation of the same STFT that has been shown in Fig. 5.7.

The continuous wavelet transform of the same OA signal is shown in Fig. 5.9 (contour plot) and Fig. 5.10 (3-D plot). These results are generated using the Molet-6 wavelet. The profile of the Molet-6 wavelet is shown in Fig. 5.12. Note that the number at the vertical axis is the level of the dilation. The real value of the dilation parameter $a$ in this case is $2^{L/4}$, where $L$ is the dilation level shown in the plot. The four echoes in the time space are clearly resolved in the time-frequency space.

The contours in the STFT plot (Fig. 5.7) are like rectangles. This is due to the fact that the widths of the time and the frequency windows are fixed. As a comparison, the contour in the CWT plot (Fig. 5.9) is like an inverse teardrop. The time width at low

dilation level (high frequency) is narrow. This is because the wavelet transform has the time-window that zooms in for high frequencies and zooms out for low frequencies. This example clearly shows that the wavelet transform has better time-frequency localization resolutions.

The power of time-frequency localization of the wavelet transform can be seen particularly in this example by noticing another small but important feature. The dilation level of the center contour corresponding to each echo shifts slightly upward for later echoes (Fig. 5.9), which means that the center frequency of the echo decreases for later echoes. This is physically correct because the acoustic loss is frequency-dependent with a higher loss at the higher frequency region. Such a frequency shifting effect is not easily seen by the STFT (Fig. 5.7) due to the poor time-frequency resolution. Hence, pulse broadening is easily discerned by the wavelet transform method.

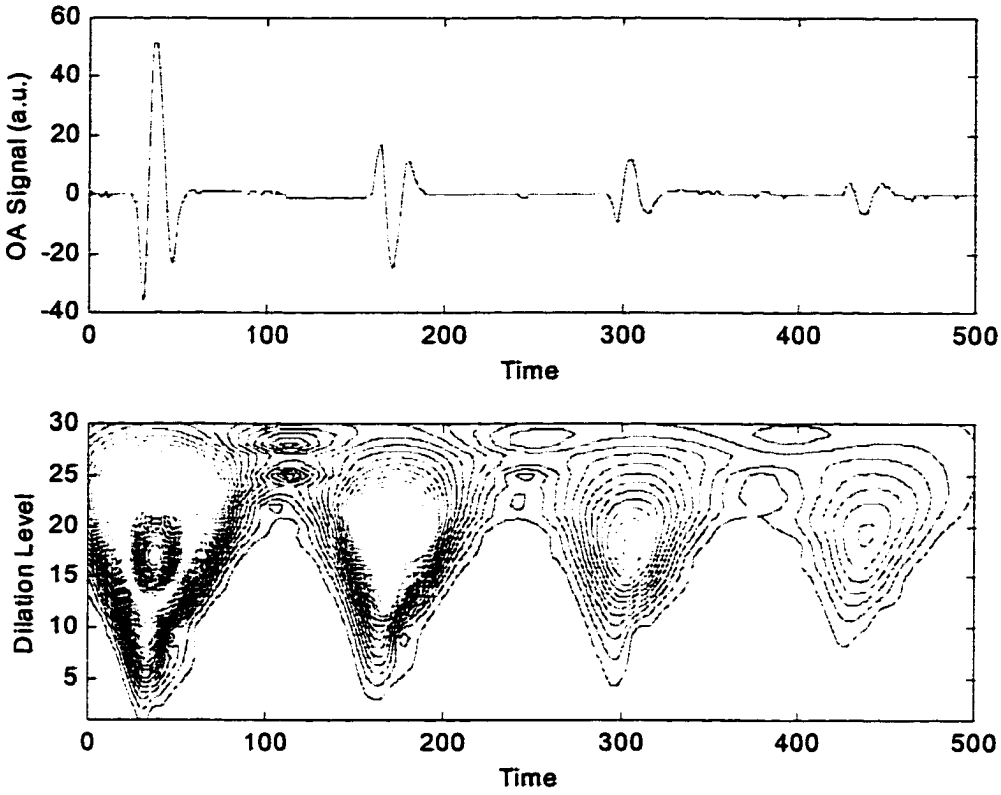


Fig. 5.9. The same OA time signal (Fig. 5.7) and its CWT transform using Morlet wavelet bases. The time axes are numbered by samples. The dilation level $L$ can be mapped to frequency by the logarithm relation $\log_2 f = c \times 2^{-L/4}$, where $c$ is a calibration constant. Therefore, a higher dilation level corresponds a lower frequency.

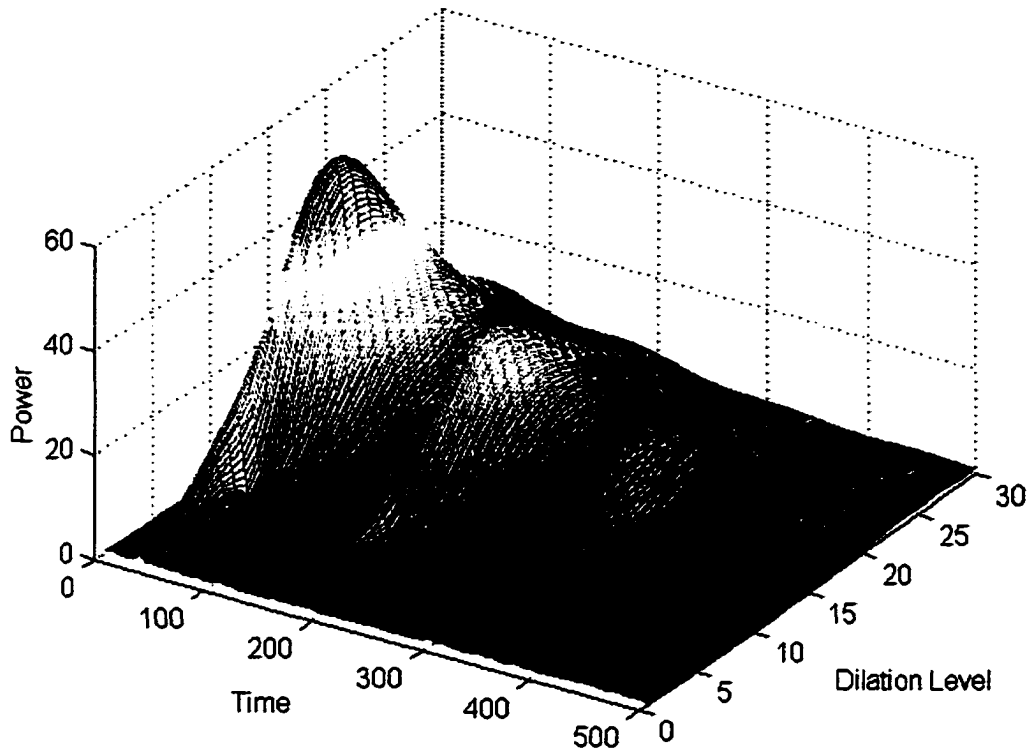


Fig. 5.10. Three-dimensional representation of the same CWT shown in Fig. 5.9.

As mentioned earlier, there are many choices for the wavelet basis functions. The wavelet used to produce Fig. 5.9 and Fig. 5.10 is Morlet-6. The Morlet-6 is a complex wavelet (see Fig. 5.12). As a comparison, the DOG-2 (second derivative of the Gaussian function) wavelet (also named Mexican hat) was used to process the same OA signal and yielded the results shown in Fig. 5.11. The DOG-2 is a real wavelet (Fig. 5.12). There are two main differences between these two wavelet transforms (by Morlet-6 and DOG-2 wavelets). First, the wavelet transform using DOG-2 wavelet exhibits finer scale structure in time space, yet coarser scale in frequency space. Second, the center frequency of the same echo from the OA signal is located at different dilation levels in the two plots. This

is because the calibration constant for the conversion between the dilation parameter $a$ and the Fourier frequency is different for each wavelet. The choice of wavelet basis function is really application dependent.

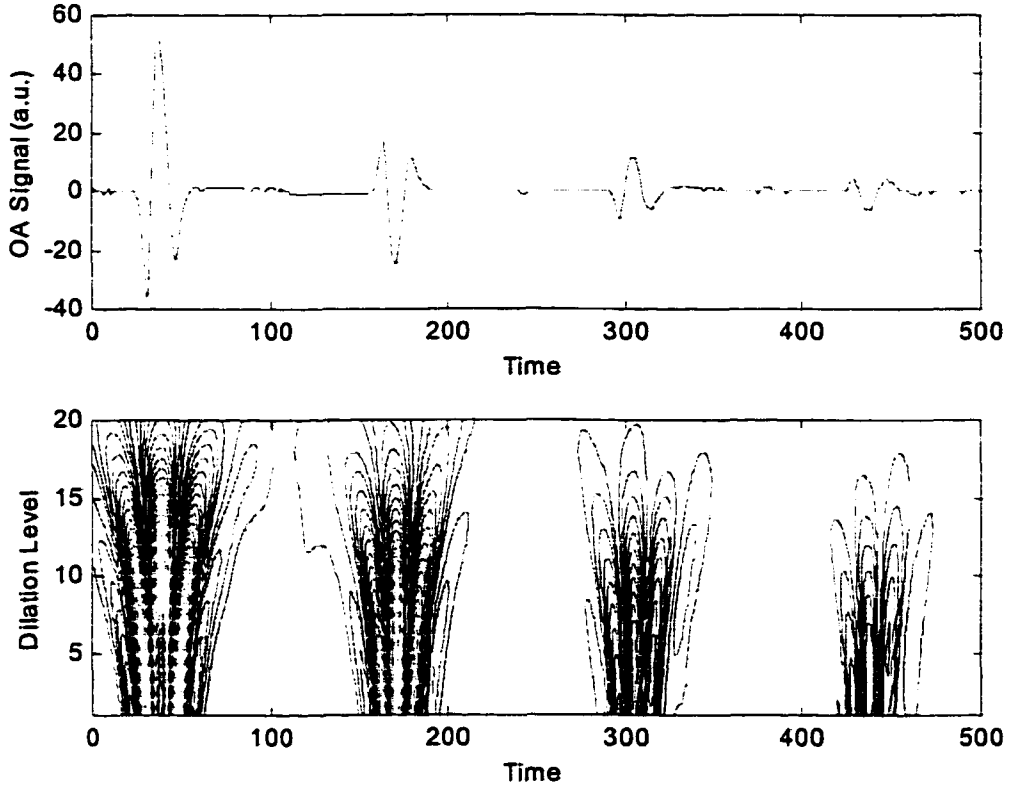


Fig. 5.11. CWT of the same time signal (Fig. 5.9) but using DOG2 wavelet bases.

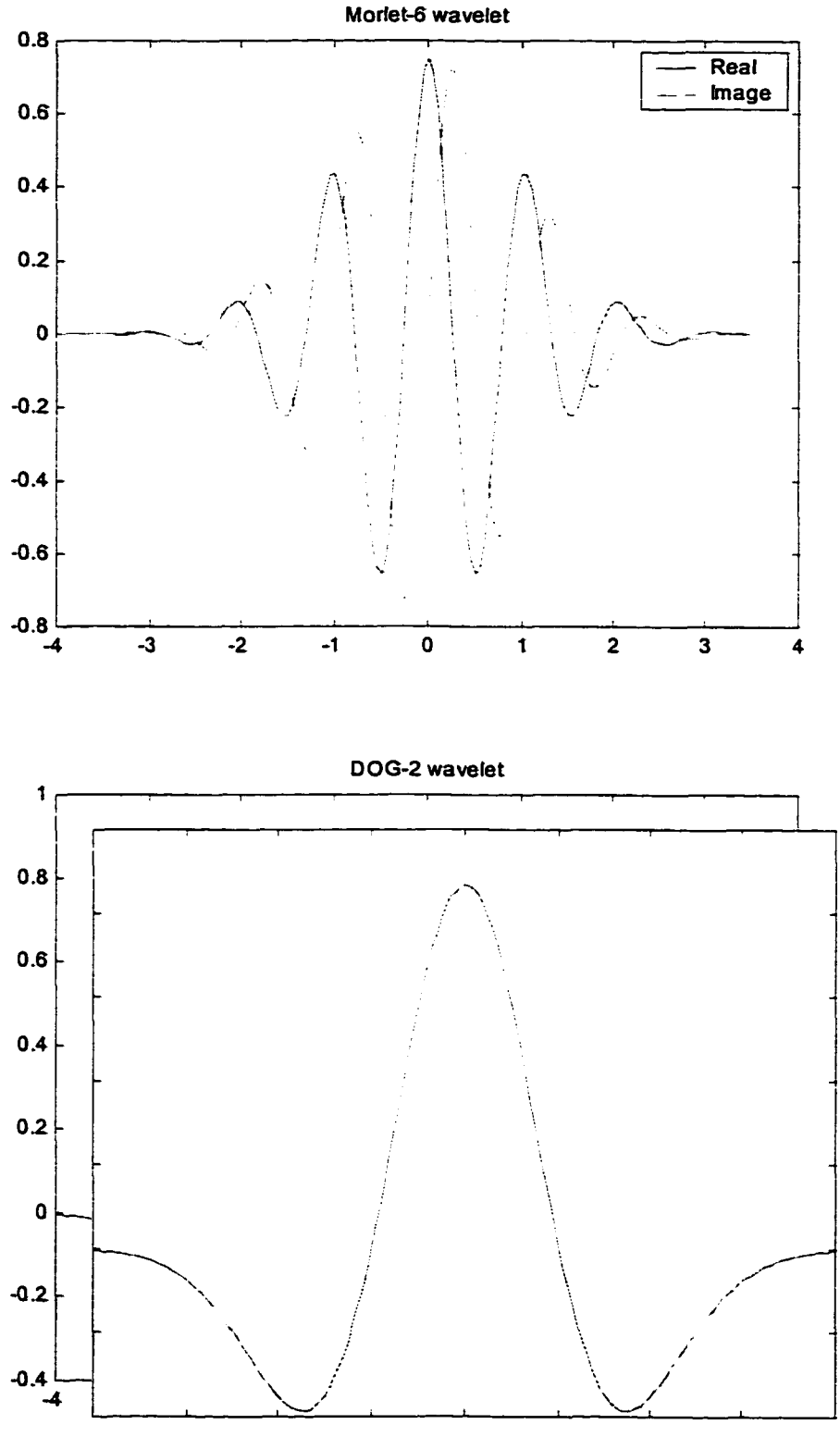


Fig. 5.12. The wavelets that have been used to produce Fig. 5.9 - Fig. 5.11.

Fig. 5.13 shows the OA signal obtained from an aluminum sample excited by the passivation light as well as the CWT of the signal. Compared with the result obtained from a PVC sample, the aluminum's OA signal is much more complicated, although both samples are excited by the same light source. This complexity comes from the coexistance of both the longitudinal and shear acoustic modes within the alumininum sample. Note that the generation mechanisms have been discussed in Chapter II. These two acoustic modes mix together in the one-dimensional time space. However, they can be clearly separated in the two-dimensional time-frequency space by the wavelet transform (the lower plot in Fig. 5.13). The longitidinal mode acoustic pulses are wide band, which is reflected in the plot where the dilation extends toward level 1. The shear mode acoustic pulses are narrow band, and in the plot the dilation only extends to about level 10.

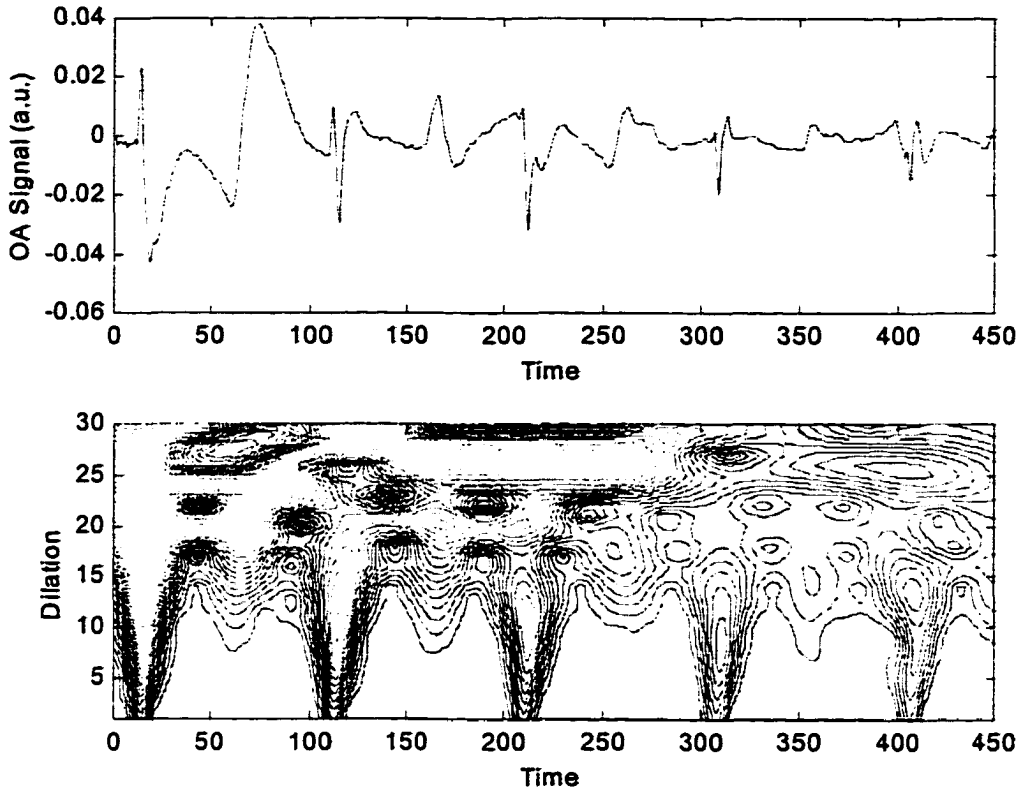


Fig. 5.13. An OA signal from an aluminum sample and its wavelet transform. The longitudinal and shear waves are clearly separated in the time-frequency space. The wide band pulses (lower dilation levels) are in longitudinal wave mode and the narrow band (higher dilation levels) pulses are in shear wave mode.

## 5.3. SIGNAL DENOISING BY WAVELET SHRINKAGE

Signal denoising is one of many successful applications of wavelet transforms. In this section the process of denoising will be briefly described, followed by a discussion of the advantage of denoising by wavelet transforms. Finally, the denoised signal from the optoacoustic experimental result by wavelet shrinkage is presented, and compared with the results by other traditional methods.

### 5.3.1. Principle

The process of removing noise by applying a threshold to the DWT coefficients has been summarized by Donoho, who named this method wavelet shrinkage [80]. Assume that the noisy signal $y$ has $n$ samples, i.e., $y_i = f(t_i) + \sigma z_i, i = 1,...,n$ ; here $f(t_i)$ is the real signal and $z_i$ is a white noise with standard deviation $\sigma$. To process signal denoising, first, one obtains the wavelet coefficients of the noisy data (the noisy signal are preconditioned and normalized to $\sqrt{n}$). Then one applies thresholding to the noisy wavelet coefficients. All coefficients whose absolute values are less than the threshold $t = \sqrt{2\log(n)}\sigma / \sqrt{n}$ are set to zero.

There are two ways to deal with those coefficients whose absolute values are larger than or equal to the threshold $t$. For *soft-thresholding*, the threshold $t$ is subtracted from each absolute value; while for *hard-thresholding*, these coefficients keep their original values. Finally, one reconstructs the signal using the inverse wavelet transform with the shrunken wavelet coefficients, producing the estimated (less noisy or noiseless) $\tilde{f}(t)$.

Note that in this process, forward and inverse discrete wavelet transforms are used for the purpose of simple and fast computation.

The foundation of the wavelet shrinkage method lies on the fact that for most practical useful signals, only a few DWT coefficients are significant while the remaining coefficients are zero or insignificant since almost all the signals have limited bandwidth. However, white noise evenly spreads out over all DWT coefficients with small amplitude. This is because the white noise has a limited energy content but a wide band spectrum. Therefore, the DWT of a contaminated signal shows several coefficients standing out from the rest of the small coefficients. By setting all insignificant coefficients to zero, the wavelet shrinkage can effectively suppress the noise and still keep the signal's fidelity.

The behavior of wavelet shrinkage is very different from other traditional denoising methods, such as the linear smoothing or the filtering method. The linear smoothing method suppresses noise at the expense of significant broadening, and in fact, it erases certain features of the signal. The filtering method suppresses noise at a certain frequency band but cannot filter out all the noise if the noise is white. At the mean time, it may filter out part of the signal, causing the signal distortion. All these differences are shown in the examples given below.

### 5.3.2. Application to remove noise in OA signals

Noise exists for all practical experimental signals. For a repeatable pulsed experiment, such as the pulsed optoacoustic experiment where the acoustic signal pattern repeats with the repetition of pumped laser pulses, the best way to remove the random

noise is to take multiple measurements and get an average from all the acquired signals. This can be achieved by using a Boxcar Averager or a digital scope operating in the average mode. However, if the laser repetition rate is very slow, for example the excimer and the nitrogen lasers that we used for our OA experiments work at several Hz, it usually takes a long time to get a good average. The averaging method is not applicable for some applications such as OA imaging in a scanning manner. In this case, the wavelet shrinkage method introduced above can be used to effectively remove white noise existing in a single shot.

Here, we use the wavelet denoising technique to process a very noisy OA signal, and then compare it with the results obtained by other denoising methods. The averaged result from a digital scope will be used as a reference, since it is the closest measurement that we can obtain to the real signal.

Fig. 5.14 shows the OA signal obtained from the PVC sample pumped by a nitrogen laser. Fig. 5.14(a) is the signal recorded by a single shot and it contains a lot of noise. Most of the noise presented in this single shot has been removed by a digital scope operating at average mode (at level 256). The averaged signal is shown in Fig. 5.14(b). This averaged signal will be used as a reference to compare with the results from every denoising method used in this section.

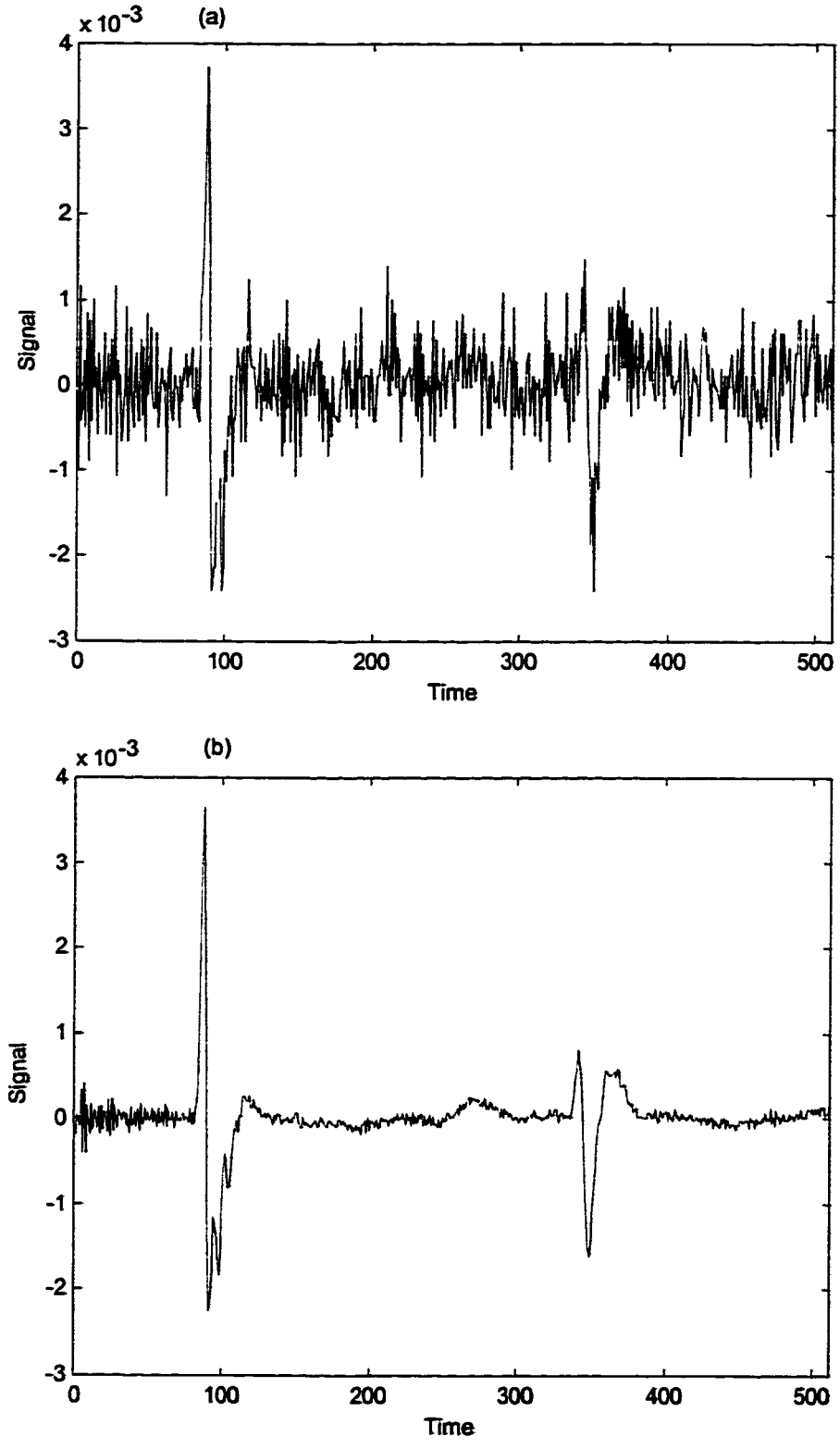


Fig. 5.14. An optoacoustic signal: (a) a single shot; (b) averaged by multiple shots.

**A. Denoising by wavelet shrinkage**

Fig. 5.15 shows the denoising process by the wavelet shrinkage method. The noisy signal is plotted in Fig. 5.15(a). It contains 512 samples. The DWT of the noisy signal is plotted in Fig. 5.15(d). The DWT also contains 512 coefficients. Note that in this plot the vertical axis is the amplitude of the coefficients, and all coefficients are combined and plotted along the horizon axis by both time and frequency in a way described below. The axis is non-uniformly divided into 9 segments. From left to right, each segment contains 2, 2, 4, 8, ..., 256 coefficients. Each segment covers the whole time range, which means that the time sampling rate doubles from one segment to its right neighbor. All coefficients within a segment have the same frequency, and the frequency increases with the power of two, segment by segment from left to right.

In order to use the wavelet shrinkage method, one needs to determine the threshold. For most practical signals, the variance is unknown. Therefore, one has to use an empirical threshold often determined by the visual effect of the output signal. Fig. 5.15(d) shows that the DWT of the noisy signal is also noisy, but all significant coefficients appear at the low frequency region. It is quite safe to assume that all nonzero coefficients in the second half-region (between indexes 257 and 512, which is the highest frequency region) are due to the noise and thus can be shrunk to zero. This is because for our experiment (and this is true for many other applications), the signal is over sampled over the Shannon sampling limit. Therefore, at least all DWT coefficients in this region should be zero. For the best visual effect, the threshold can be set to the maximum magnitude of the noisy coefficients in the second half region. In Fig. 5.15, the threshold has been set to $1.5\times10^{-3}$ for both soft- and hard-thresholding. Both results are visually noiseless.

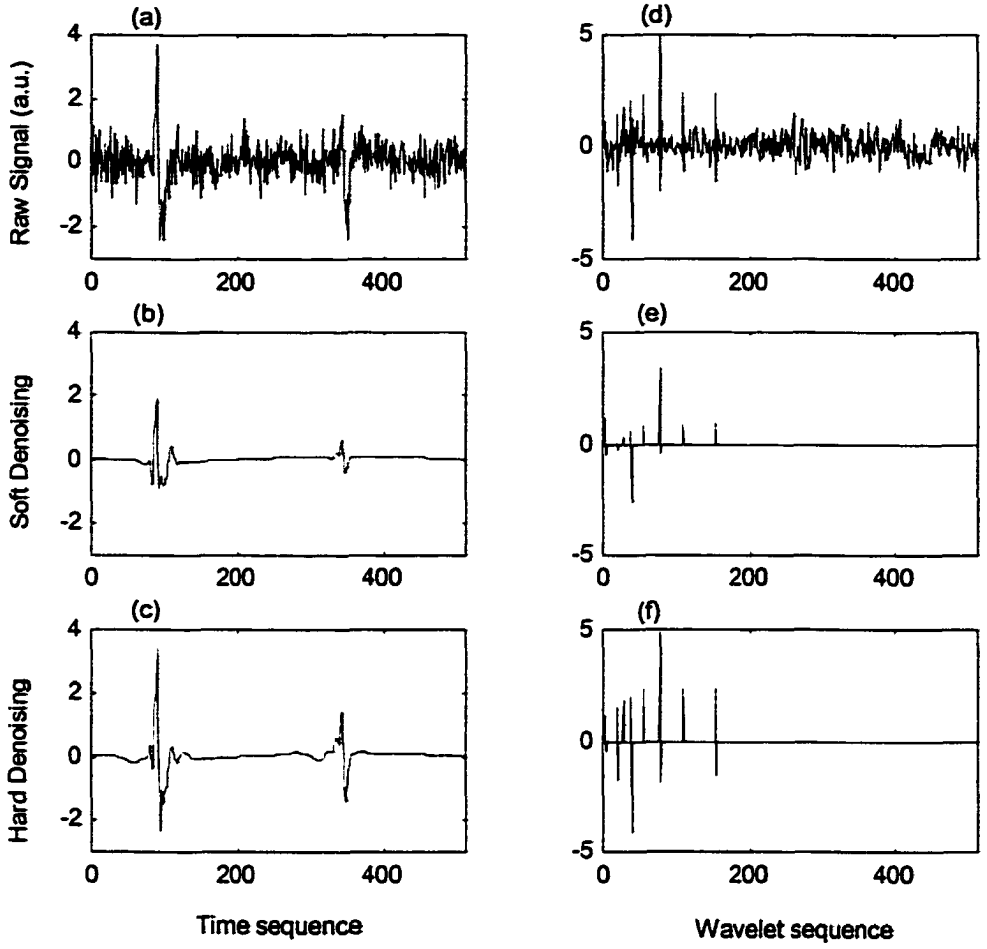


Fig. 5.15. The signal before and after denoising: (a) raw signal; (b) signal denoised by soft-thresholding; (c) signal denoised by hard-thresholding; (d)-(e) corresponding DWT coefficients to (a)-(c). All the vertical scales have a factor of $10^{-3}$. The threshold for both denoising is set to be $1.5\times10^{-3}$.

However, if the threshold is set too high, some useful information may also be removed from the signal and errors will be introduced in the result. This is because any DWT coefficients that are below the threshold, but belong to the real signal, will be treated as noise and shrunk to zero. To reduce the risk of losing useful information, the wavelet basis set that most resembles the main feature of the time signal needs to be used to perform the DWT. By using the optimized wavelet, the signal can be transformed into

a lesser number of DWT coefficients but with higher amplitudes. For this treatment, the Coilet-3 wavelet basis (Fig. 5.16) has been used.

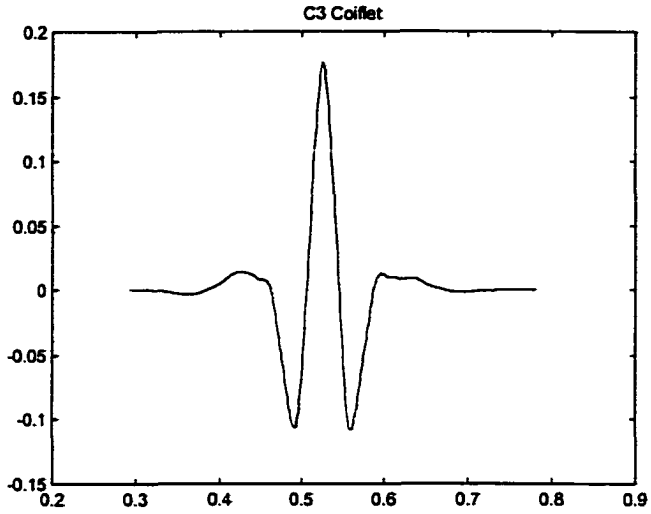


Fig. 5.16. Coiflet-3 wavelet basis function.

The three results, namely the averaged signal, the one obtained by soft-thresholding and the one obtained by hard-thresholding are superimposed in one plot (Fig. 5.17). From this figure we draw the following conclusions. First, both thresholding methods are able to effectively remove noise and keep the fidelity of the signal, especially in that the signal pulses are not broadened. Second, the result from hard-thresholding maintains the signal amplitude while the result from soft-thresholding decreases a little bit in amplitude. This is because the coefficients that belong to the real signal shrink by the amount of the threshold in the soft-thresholding but they stay unchanged in the hard-thresholding. Third, there is a slight distortion of the results from the wavelet shrinkage methods (by the threshold $t = 1.5\times10^{-3}$). Therefore, as expected, there is a tradeoff between removing noise and preserving fidelity of the signal.

To illustrate this tradeoff, we reduced the threshold $t$ to $0.8\times10^{-3}$ and repeated the denoising process. This result is shown in Fig. 5.18. Since this threshold is not high enough to remove all noisy coefficients in the highest frequency region, the recovered signals exhibit some spike-like noise. However, the acoustic pulses in these recovered signals have less distortion. Although the signal recovered from soft-thresholding has attenuation in amplitude, it exhibits a better visual effect than that from hard-thresholding. Note that wavelet shrinkage is a nonlinear process. Therefore, even though these two results from soft- and hard-thresholding have similar features, one cannot make them identical by normalizing one to the other.

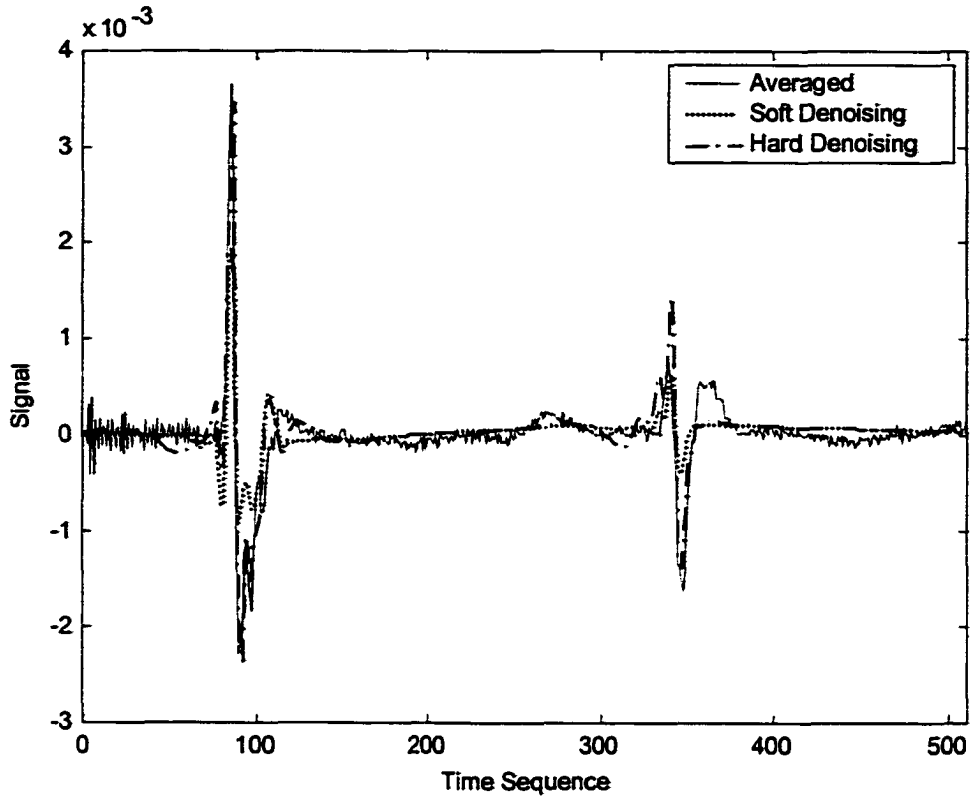


Fig. 5.17. Superimposing the denoising results by three methods: averaging, wavelet soft denoising and wavelet hard denoising.

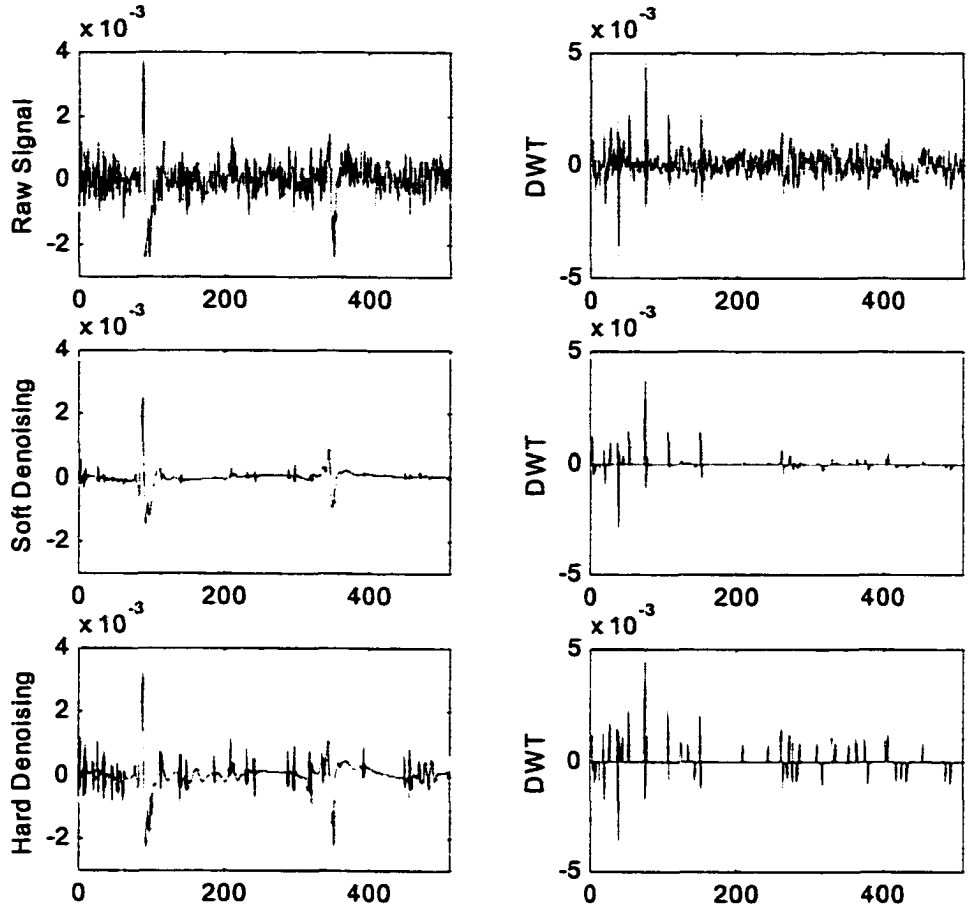


Fig. 5.18. The signal before and after denoising, and the corresponding DWT coefficients before and after thresholding. Both soft- and hard-thresholding are used. The threshold for both cases is set to be $0.8\times10^{-3}$.

**B. Denoising by linear smoothing**

We also used the linear smoothing and filtering methods to remove noise from the same testing signal. The linear smoothing method slides a window along the time axis. The average of all samples within this window is used as an estimate for the signal at the center of the window. If the smoothing window is too wide, it leads to the distortion (broadening) of the signal. If the window is too narrow, it cannot remove very many noises. In addition, this method is not effective in removing low frequency noise, since the smoothing window is equivalent to a lowpass filter. This tradeoff is shown in Fig. 5.19. To generate Fig. 5.19(a), a smoothing window incorporating 15 samples was used. Most noise has been removed, but the acoustic pulses are also broadened. In contrast, Fig. 5.19(b) used a 5-sample window. However, the result is still quite noisy.

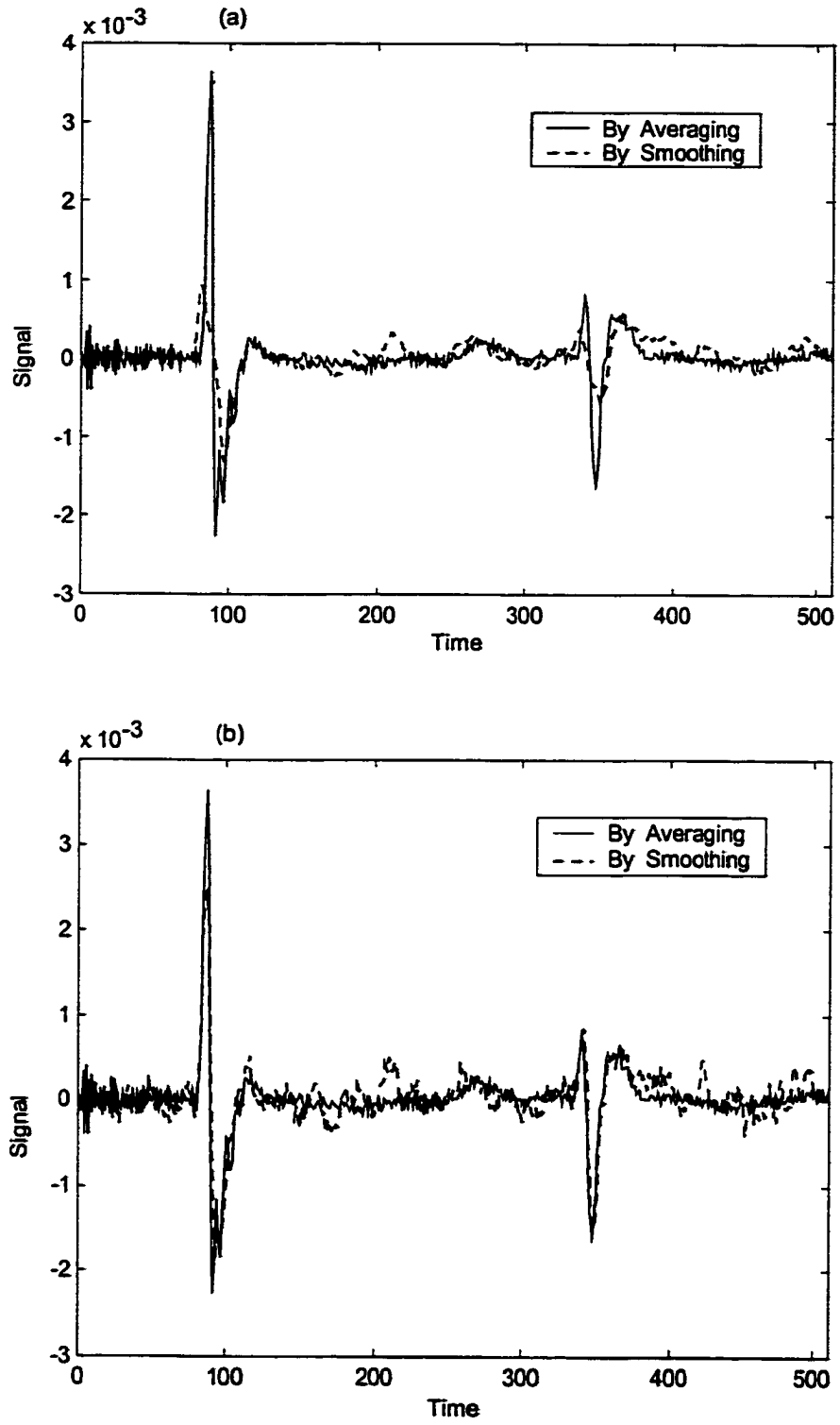


Fig. 5.19. Denoising by the linear smoothing method: (a) the size of the smoothing window is 15; (b) the window size is 5.

**C. Denoising by filtering**

Fig. 5.20 shows the denoising results by the filtering method. In this example, a lowpass finite impulse response (FIR) filter and a bandpass FIR filter are used to remove the noise. The passband for the lowpass filter is [0 0.25π]. The passband for the bandpass filter is [0.1π 0.25π]. Both filters are able to remove some noise. However, they cannot remove the noise within the passband. If the passband is too narrow, the signal will suffer distortion. In this example, the bandpass filter results in more distortion. Therefore, this method cannot remove any noise that has the same frequency contents as the real signal, which is also true for the linear smoothing method.

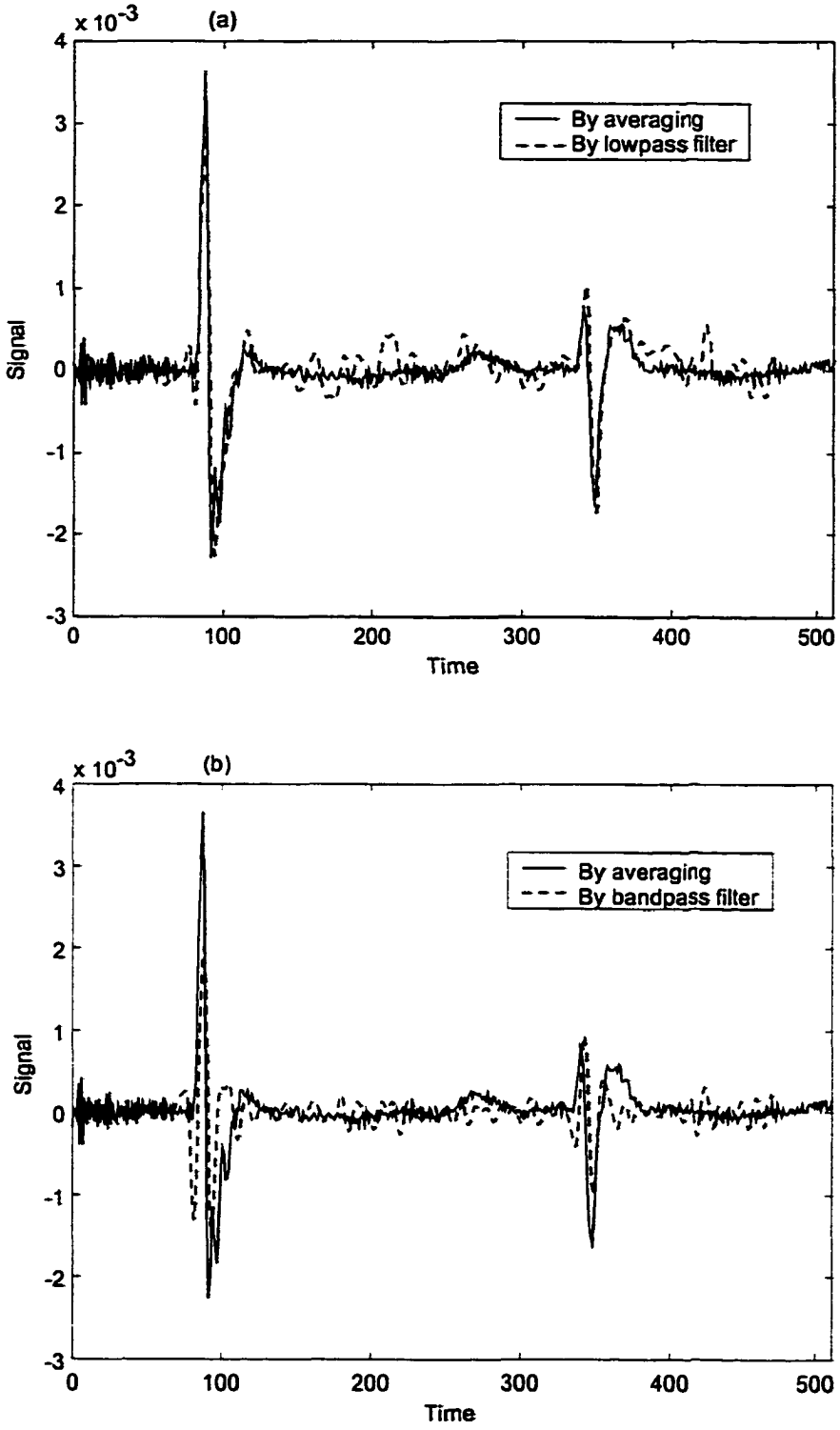


Fig. 5.20. Denoising by the filtering technique: (a) filtered signal by an FIR lowpass filter; (b) filtered signal by an FIR bandpass filter.

In summary, the linear smoothing and the filtering methods can only partially remove noise. They have difficulty in treating noises whose frequency ranges are within the spectrum range of the real signal. However, the wavelet shrinkage can effectively remove noise while the recovered signal maintains high fidelity. In our example, this method can completely remove the noise outside the OA pulse region even though the noise has a spectrum overlap with the acoustic pulses.

The wavelet shrinkage method is a powerful tool only when the signal is white. If the noise is not white, high amplitude wavelet coefficients appear in the transform space. Then the fixed threshold is not reasonable, and a dynamic threshold is effective if the characteristics of the noise are known. The filtering technique may be more convenient in some situations. In addition, there is a tradeoff between removing noise and maintaining fidelity while selecting the threshold for wavelet shrinkage. For many applications fidelity is more important, therefore the threshold should not be set too high, which will allow some noise to remain in the signal.

### D. Denoising by the hybrid method

Here we propose a hybrid method that combines both the wavelet shrinkage and the traditional denoising techniques. We illustrate that by applying this novel technique to the same noisy testing signal we are able to obtain better results.

Fig. 5.21 is the denoising result obtained by first applying hard thresholding wavelet shrinkage with a threshold $t = 1.0\times10^{-3}$ and then by filtering the output from the wavelet shrinkage with a lowpass FIR filter whose cutoff frequency is $0.4\pi$. In this process, the threshold used for the wavelet shrinkage is not high enough to remove all noise but it

maintains high signal fidelity. The remaining spike-like noise is further removed by the lowpass filter whose passband is wide enough not to distort the signal itself. Therefore the overall quality of the result from these two denoising steps is improved. This can be seen by superimposing the result to the averaged signal in Fig. 5.21. The lowpass filtering can be alternatively replaced by the linear smoothing. Fig. 5.22 shows such a result by utilizing hard thresholding at $t = 1.0\times10^{-3}$, followed by applying a smoothing window with size 5 twice to the output from the previous step. This denoising result has the similar quality as the first hybrid technique (Fig. 5.21), and both are better than the results obtained before (Fig. 5.17 - Fig. 5.20) by using only one denoising method.

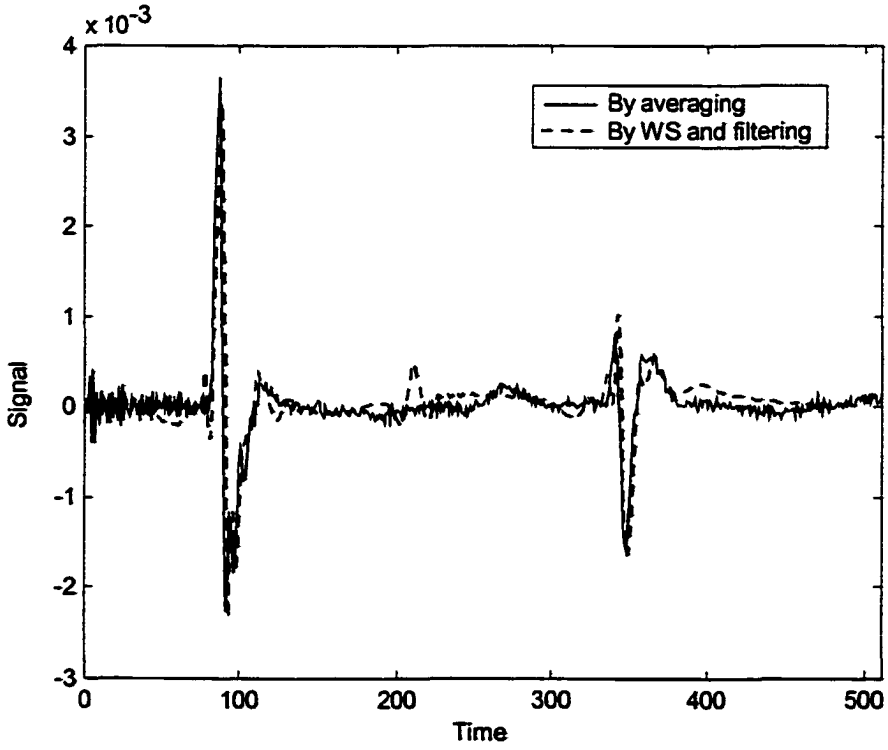


Fig. 5.21. Denoising by the hybrid technique: first wavelet shrinkage (WS) and then filtering.

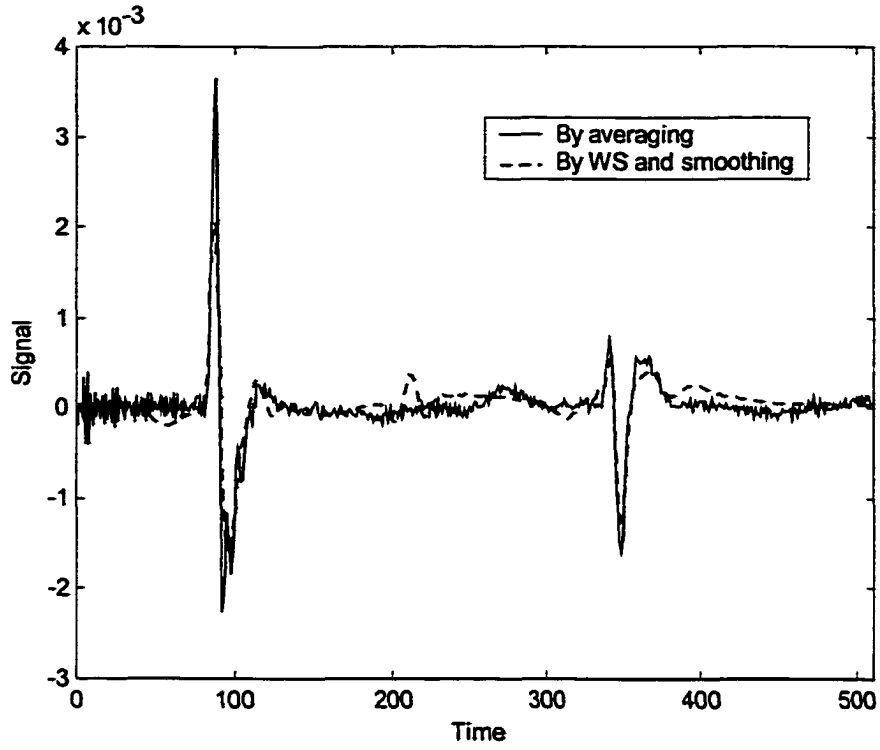


Fig. 5.22. Denoising by the hybrid technique: first wavelet shrinkage (WS) and then linear smoothing.

The advantage of the hybrid technique, which to our knowledge is the first such application, gives a dramatic improvement in signal quality. This can be seen by the appearance of the third pulse, between the two main echoes, in both Fig. 5.21 and Fig. 5.22. This pulse is in shear mode in the PVC sample while the main pulses are in longitudinal mode. Similar to the aluminum OA experiment (Fig. 5.13), both longitudinal and shear waves exist in the PVC sample. Previously we neglected this shear wave because its amplitude is small and it is not the main interest of our research. Also, this pulse in shear wave mode is not obvious in the averaged signal from multiple acquisitions (Fig. 5.14, Fig. 5.21 and Fig. 5.22). It may be due to the jittering of the trigger for acquisition. To show the middle small pulse is in shear mode, we performed the continuous wavelet transform of the signal. The time-frequency plot in Fig. 5.23 clearly

shows that the middle pulse has narrower bandwidth than the main pulses (in longitudinal mode). This indicates that the middle pulse might be a shear wave. To prove the difference in bandwidths is not caused by the big changes in amplitude, we normalized these three pulses to a similar level in amplitude and redid the CWT. The result is shown in Fig. 5.24. The time-frequency plot of the normalized pulses has the same signature as before, i.e., the middle pulse has narrower bandwidth. This confirms our conclusion that the middle pulse is a shear wave.

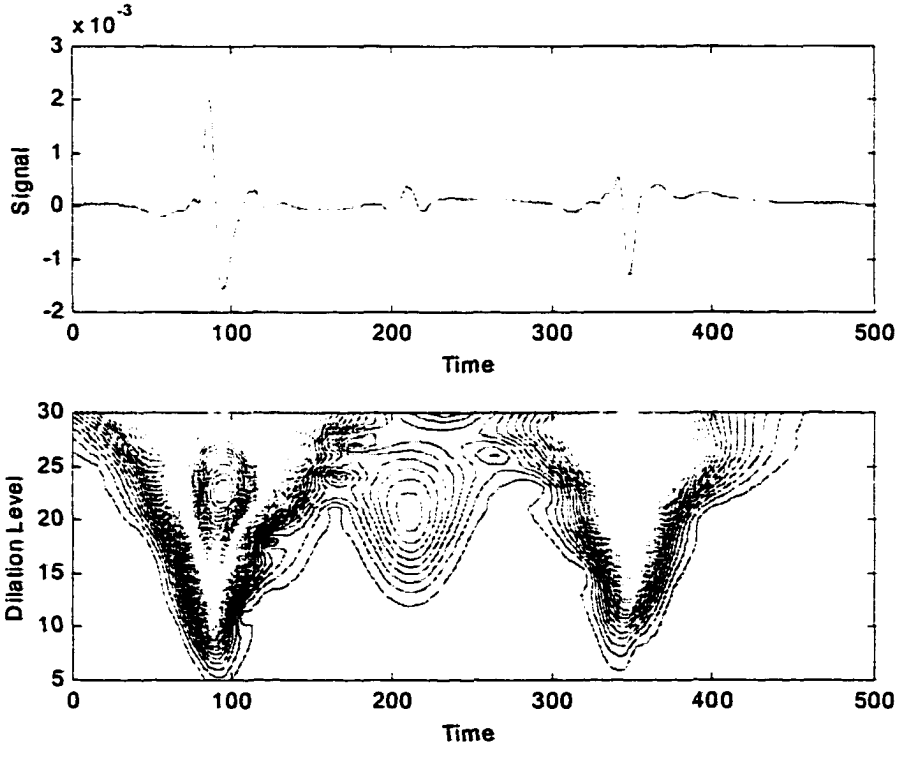


Fig. 5.23. The CWT of the denoised signal obtained in Fig. 5.21

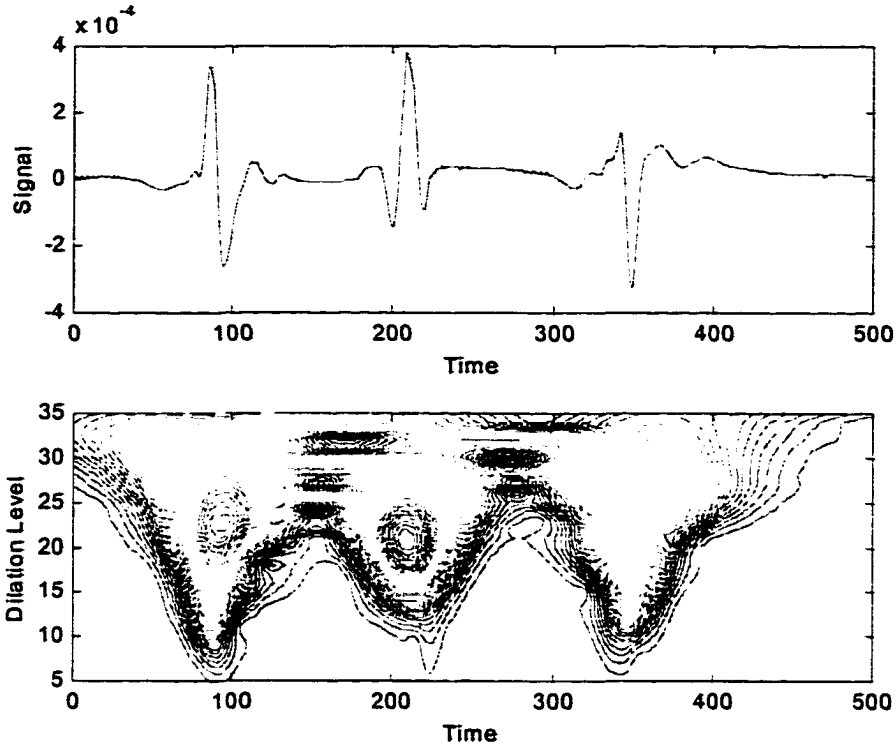


Fig. 5.24. The CWT of the normalized signal.

To conclude this section, the wave shrinkage technique has some advantages over other traditional methods in denoising. Soft-thresholding has a better visual effect than hard-thresholding, but also reduces the signal amplitude. The choice of the threshold is empirical and is a tradeoff between rejecting noise and maintaining signal information. We illustrated that the combination of the wavelet shrinkage and the filtering or smoothing techniques has better performance for our application.

# CHAPTER VI

# OPTOACOUSTIC APPLICATIONS

As summarized in Chapter I, optoacoustic techniques have been used for diagnostics of material properties, such as the optical absorption coefficient. In this chapter we describe the acoustic spectral ratio technique, which is a new method developed during the course of this research to determine the optical absorption coefficient of a condensed sample. This method utilizes boundary conditions but requires less knowledge of other parameters than that required by traditional OA methods. We also present OA results performed on biological tissues. We apply the new data processing and diagnostic techniques developed in the previous and current chapters to treat the experimental results from these tissue samples.

## 6.1. MEASUREMENT OF OPTICAL ABSORPTION COEFFICIENT BY THE ACOUSTIC SPECTRAL RATIO TECHNIQUE

The new method discussed here uses one laser source and detector. One end of the sample is subject to an unvarying boundary condition, while the front end, which is irradiated by the laser, is subject to varying boundary conditions. We show below that a measurement and comparison of the signals obtained under these varying boundary conditions then yields information about the optical absorption coefficient of the material.

### 6.1.1. Introduction

The conventional optoacoustic method for obtaining a quantitative value of the optical absorption coefficient requires one to have a measurement of the laser pulse energy and the magnitude of the optoacoustic signal. One also needs a value of the sample's specific heat, thermal expansion coefficient, density and sound speed.

The absorption coefficient can also be derived from the temporal profile of the optoacoustic signal, by realizing that the spectrum of the acoustic signal is proportional to the product of the frequency spectrum of the light pulse and the spatial spectrum of the temperature distribution function. The temperature distribution caused by a delta light pulse is only determined by the absorption coefficient. Therefore, the absorption coefficient can be obtained from the deconvolution of the OA signal from the known laser pulse profile. This deconvolution method even allows one to determine a spatially varying absorption coefficient for an inhomogeneous medium [34]. However, a practical acoustic transducer will introduce distortion to the signal one measures. The deconvolution method will not work if the behavior of the transducer is not known, which is quite true if it is a commercial product.

Absorption coefficient measurement utilizing a ratio technique was proposed before by Terzic and Sigrist [37]. In their method, the amplitude ratio of the OA signal peaks, under the rigid and the free boundary conditions, was taken. By taking the ratio, some of the common parameters that are required to describe each signal can be canceled in the formula. For instance, knowledge of the temporal profile of the laser pulse, the energy of each pump pulse, the specific heat of the sample and the sensitivity of the detector, is not needed if these parameters do not vary during the transition of boundary conditions. This

ratio technique assumes that the acoustic detector is ideal. A non-ideal transducer can affect the locations and magnitudes of the peaks at both signals in different ways, which makes this method inapplicable if the behavior of the detector is unknown. In addition, the method requires the experiment to be done with the rigid boundary, which cannot be easily fulfilled in many applications.

The spectral ratio method we propose here compares the spectra of optoacoustic signals generated at different boundary conditions. Therefore, the influence upon the signals of a non-ideal transducer can be cancelled since the transfer function is the same for both cases. In addition, the rigid boundary is not necessarily required for our formulation. Instead, a general boundary together with a free boundary can be used. Similar to the peak ratio method, knowledge of many common parameters is not required for this new method.

### 6.1.2. Theory

The spectrum of an optoacoustic signal, $P(\omega)$, can be expressed as [36]

$$P(\omega) = a\ I(\omega)\ F(\omega)\ T(\omega), \tag{6.1}$$

where $a$ is a constant; $I(\omega)$ is the laser power spectrum; $F(\omega)$ is the Fourier transform of the acoustic impulse response of the sample; and $T(\omega)$ is the transfer function of the transducer.

This relationship assumes that the system is linear, and describes the scenario where the incident laser (spectral intensity $I(\omega)$) irradiates the sample, whose response function is $F(\omega)$. The latter includes all the effects that account for acoustic pulse generation by

thermal means. Hence, $F(\omega)$ is the response function which incorporates the generation of the initial acoustic signal from thermal expansion, as well as the acoustic effects that originate from thermal diffusion from the absorption region.

$T(\omega)$ describes the response of the detector to the total acoustic signal generated. This function will depend on the method of detection employed. For example, the functional form of $T(\omega)$ will be different when one uses optical detection as opposed to piezoelectric detection.

The ratio of the spectra of acoustic signals with two different boundary conditions is

$$P_1(\omega) / P_2(\omega) = F_1(\omega) / F_2(\omega), \tag{6.2}$$

since the other terms in Eq. (6.1) cancel out.

The acoustic impulse response of the sample is its response to an optical delta pulse. If one ignores the effects of thermal diffusion that occur subsequent to the initial thermal expansion that generates the original acoustic pulse, which is true for most of our experiments, the impulse response can be written as the following (as discussed in Chapter II):

$$f(t) = \begin{cases} e^{\alpha c_0 (t - t_0)}, & 0 \le t \le t_0 \quad \text{(6.3a)} \\ k_r e^{-\alpha c_0 (t - t_0)}, & t > t_0 \quad \text{(6.3b)} \end{cases}$$

Here, $t_0 = L / c_0$ is the time it takes for the acoustic signal to travel the length of the sample, at the end of which is the detector. $k_r$ is the pressure reflection coefficient at the irradiated end of the sample. Eq. (6.3a) represents the acoustic profile seen at the detector end due to the direct traversal of the signal from the irradiated end. Eq. (6.3b) describes the acoustic signal that reaches the detector after first having reflected off the irradiated

surface. These components and the complete temporal profile of the signal pulse reaching the detector have been shown in Fig. 2.2 in Chapter II.

If one considers the acoustic loss with coefficient $\beta$, Eq. (6.3) should be revised as:

$$f(t) = \begin{cases} e^{\alpha c_0 (t-t_0)} e^{-\beta c_0 t}, & 0 \le t \le t_0 \quad (6.4a) \\ k_r e^{-\alpha c_0 (t-t_0)} e^{-\beta c_0 t}, & t > t_0 \quad (6.4b) \end{cases}$$

Note that, in general, $\beta$ is frequency dependent. Here we assume it is a constant within the bandwidth of interest as a first order approximation. For a rigid boundary, the pressure wave reflection coefficient at the front end of the sample is $k_r = 1$, while for a free boundary $k_r = -1$. In general, the value of $k_r$ is between $-1$ and 1, for which case we call it a constrained boundary. It is this difference in the reflection coefficients at different boundaries that allows one to use the method developed here.

The Fourier transform $F(\omega)$ of Eq. (6.4) is

$$F(\omega) = e^{-\beta c_0 t_0} e^{-j\omega t_0} \frac{\alpha c_0 (1+k_r) + \beta c_0 (1-k_r) + j\omega(1-k_r)}{((\alpha-\beta)c_0 - j\omega)((\alpha+\beta)c_0 + j\omega)}. \quad (6.5)$$

The above equation is obtained under the assumption that $e^{\alpha c_0 t_0} = e^{\alpha L} >> 1$, where $L$ is the distance from the absorption surface to the detector. This condition is met for many experiments where either $L$ or $\alpha$ is large. Also, the acoustic dispersion is not considered in the above equation, i.e., the sound speed $c_0$ is a constant.

Now we can get the spectral ratio by substituting Eq. (6.5) with reflection coefficients $k_{r1}$ and $k_{r2}$ into Eq. (6.2):

$$\frac{|P_1(\omega)|}{|P_2(\omega)|} = \frac{|\alpha c_0 (1+k_{r1}) + \beta c_0 (1-k_{r1}) + j\omega(1-k_{r1})|}{|\alpha c_0 (1+k_{r2}) + \beta c_0 (1-k_{r2}) + j\omega(1-k_{r2})|}. \quad (6.6)$$

The simplest case is to utilize the free and rigid boundaries for a lossless medium. Let $\beta = 0$, $k_{r1} = -1$ for the free boundary and $k_{r2} = 1$ for the rigid boundary. Eq. (6.6) is simplified to be

$$\frac{|P_f(\omega)|}{|P_r(\omega)|} = \frac{\omega}{\alpha c_0}. \tag{6.7}$$

Therefore, the absorption coefficient can be obtained from the slope of the plot of $|P_f(\omega)|/|P_r(\omega)|$ versus $\omega$.

If acoustic loss is considered, Eq. (6.6) can be rewritten as the following equation under conditions $\beta \neq 0$, $k_{r1} = -1$ and $k_{r2} = 1$.

$$g(\omega) = \frac{|P_f(\omega)|^2}{|P_r(\omega)|^2} = \frac{\omega^2 + \beta^2 c_0^2}{(\alpha c_0)^2}. \tag{6.8}$$

The optical absorption coefficient in this case can be obtained from the second order polynomial coefficient of the best fitting of $g$ versus $\omega$.

In an experiment, the free boundary condition can be very closely approximated by exposing the surface of the condensed sample to air. However, the rigid boundary condition cannot be easily obtained because it requires the sample to be in good contact with a medium which has an infinite acoustic impedance and is transparent to the laser wavelength. Here we show that effectively any practical (i.e., constrained) boundary condition combined with the free boundary can be used to determine the absorption coefficient. This constrained boundary can be made by placing a window material that is transparent to the pump laser, such as glass or quartz for our experiments, in front of the sample with good contact.

Substituting the free boundary ($k_{r1}$ = -1) to the numerator and keeping the denominator for the general constrained boundary with reflection $k_r$, the lossless version ($\beta = 0$) of Eq. (6.6) can be written as

$$\left|\frac{P_f(\omega)}{P(\omega)}\right| = \frac{2\omega}{\sqrt{\alpha^2 c_0^2 (1+k_r)^2 + \omega^2 (1-k_r)^2}}. \tag{6.9}$$

If the value of $k_r$ is known, then the absorption coefficient can be obtained from the above equation. Alternatively, we rewrite Eq. (6.9) in the following format:

$$g(\omega) = \left(\left|\frac{P(\omega)}{P_f(\omega)}\right|^2 - \frac{(1-k_r)^2}{4}\right)^{-1/2} = \frac{2\omega}{\alpha c_0 (1+k_r)}. \tag{6.10}$$

Therefore, $\alpha$ can be obtained from the slope of the plot $g(\omega)$ versus $\omega$ using a least square fitting technique. Note that $g(\omega)$ is computed by Eq. (6.10) from experimental data $P$ and $P_f$. Due to experimental random errors, the term within the square root may turn out to be negative. In practice, frequency regions that contain such "bad" data need to be excluded.

If a constant acoustic attenuation is considered, Eq. (6.9) should be rewritten as:

$$\left|\frac{P_f(\omega)}{P(\omega)}\right| = \sqrt{\frac{4(\omega^2 + \beta^2 c_0^2)}{\alpha^2 c_0^2 (1+k_r)^2 + (\beta^2 c_0^2 + \omega^2)(1-k_r)^2}}. \tag{6.11}$$

If one desires to use the least square fitting technique to extract $\alpha$ from the above equation, the following steps can be taken. First, one can plot $g(y)$ versus $\omega$ by the following equation:

$$g(y) = \frac{y^2}{1-y^2} = \frac{A^2 + \omega^2}{B^2 - A^2},$$

where

$$y^2 = \left|\frac{P_f(\omega)}{P(\omega)}\right|^2 \frac{(1-k_r)^2}{4},$$

$$B^2 = \frac{[\alpha c_0(1+k_r)+\beta c_0(1-k_r)]^2}{(1-k_r)^2},$$

and

$$A^2 = \beta^2 c_0^2.$$

$g(y)$ is computed from experimental data, and the following parameters $k_1$ and $k_2$ are obtained from the least square fitting technique:

$$k_1 = \frac{A^2}{B^2 - A^2},$$

and

$$k_2 = \frac{1}{B^2 - A^2}.$$

Therefore, acoustic attenuation coefficient is obtained by taking the ratio of $k_1$ and $k_2$

$$\beta = \frac{1}{c_0}\sqrt{\frac{k_1}{k_2}}.$$

Then optical absorption coefficient can be solved from the following equation

$$\frac{\alpha^2 c_0^2(1+k_r)^2 + 2\alpha\beta c_0^2(1-k_r^2)}{(1-k_r)^2} = k_2. \tag{6.12}$$

The above discussion shows that to measure the absorption coefficient utilizing the acoustic spectral ratio technique, one can record the OA signals at the free and constrained boundary, respectively. In addition, one needs to know the sound speed and the pressure reflection coefficient at this constrained boundary. Since $k_r$ is determined by the acoustic impedances of the two materials forming the boundary, namely the window

and the sample, one only needs to know the sound speed and the density. Sound speed can be obtained by measuring the time interval between optoacoustic echoes of a known thickness. Density can be measured by any conventional methods. Note that usually the impedance of the window material is known.

In summary, this new method provides a simple but powerful tool to determine the optical absorption coefficient. It does not require knowledge of the specific heat, thermal expansion coefficient of the sample, nor that of the intensity and temporal profile of the laser pulse. In addition, the response of the transducer and any amplifiers that are used in the experiment need not be known. It is especially useful for the measurement of an unknown material.

It must be pointed out that there are some limits to the spectral ratio method. First, the above derivation is based on a one-dimensional OA generation theory; therefore, it is valid only for the case where pump laser can penetrate into the sample by a certain depth and directly generate longitudinal OA signal in the laser incident direction through thermal expansion effect. Second, in the derivation we did not consider the multi-reflection at the other end of the sample and the window. Therefore, both the sample and the window should be long enough that they guarantee that no reflected signal from the other ends will mix with the original acoustic pulse. Future work is needed to extend the theory to include this multi-reflection effect.

Next, we will use our method to extract optical absorption coefficients from published OA experimental data and compare our results with published values of the coefficients. We also apply this new technique to analyze our own OA experiment data and get the absorption coefficients of the sample at different wavelengths.

### 6.1.3. Applications

In this section, we first utilize the acoustic spectral ratio method to extract the absorption coefficient of water from OA experimental data obtained at the free and the rigid boundaries by Sigrist [48]. It shows that our measurement is in good agreement with the published value of the absorption coefficient. Then, we use the same method to measure the coefficient for PVC at three different wavelengths, where the free and constrained boundary are encountered.

#### A. Analysis of published experimental data

Fig. 6.1(a) shows the OA experimental results from distilled water under the free and rigid boundary conditions [48]. The pump was a $CO_2$ laser at a working wavelength of 10.6 μm. The pulse width is about 90 ns (our method does not require the knowledge of the pulse width). The spectra of these two signals are plotted in Fig. 6.1(b). The published value of the optical absorption coefficient of water at this wavelength is $8.7\times10^{4}$ $m^{-1}$ [48]. If losses are neglected, the spectral ratio method yields $\alpha = 8.5\times10^{4}$ $m^{-1}$ using Eq. (6.7). This process is shown in Fig. 6.1(c). If losses are not neglected, Eq. (6.9) is used to give both $\alpha$ and $\beta$ from the coefficients of the second order polynomial fitting to the experimental data. This process is shown in Fig. 6.1(d), where $\alpha$ was calculated to be $8.9\times10^{4}$ $m^{-1}$ and $\beta = 5.3\times10^{3}$ $m^{-1}$. To our knowledge, the measurement of $\beta$ is too high. However, our measurements for $\alpha$ using the spectra ratio method are in good agreement with the publish data.

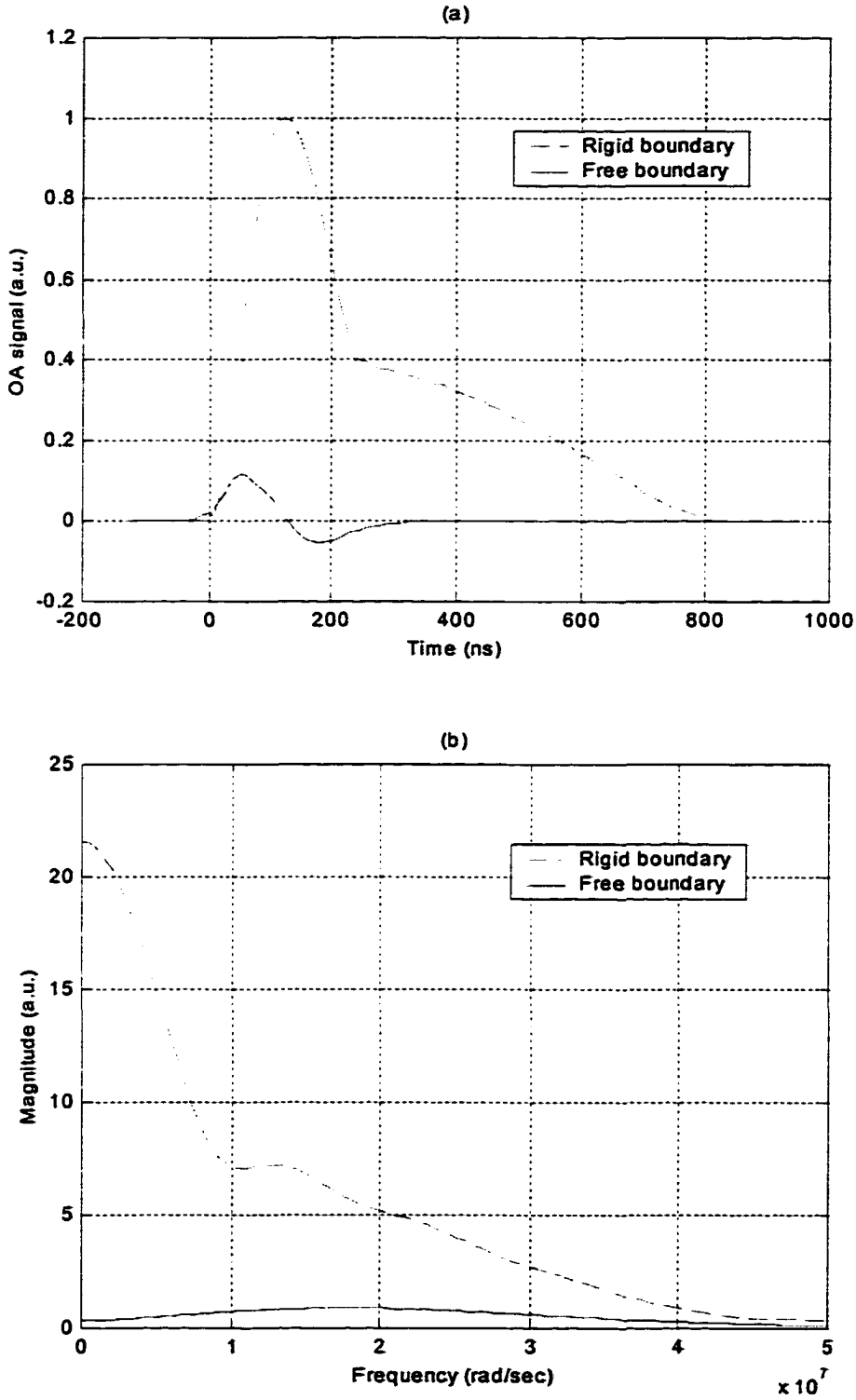


Fig. 6.1 (a)-(b). OA signals from $H_2O$ under the rigid and the free boundaries pumped by a $CO_2$ laser: (a) time signals [48]; (b) spectra of the signals.

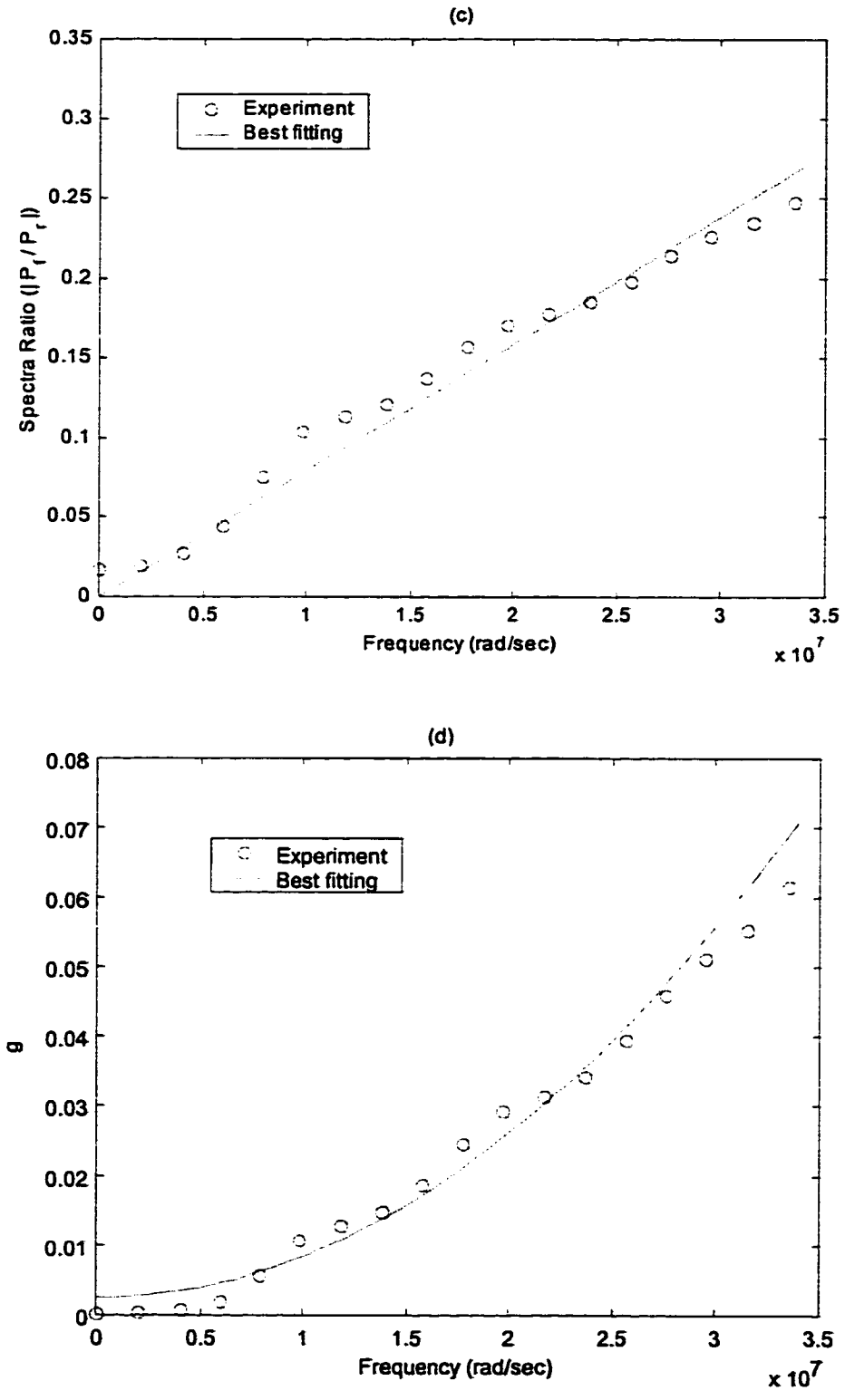


Fig. 6.1 (c)-(d). Measurement of optical absorption coefficient $\alpha$: (c) neglects acoustic losses and uses Eq. (6.7). $\alpha = 8.5\times10^{4}$ m$^{-1}$; (d) considers acoustic losses and uses Eq. (6.8). $\alpha = 8.9\times10^{4}$ m$^{-1}$.

Sigrist also did experiments on heavy water ($D_2O$) and gave the reference of the value of $\alpha$ at 10.6 μm to be 4.2 $\times 10^4$ $m^{-1}$ [48]. We took his experimental data and applied our method to determine $\alpha$. If acoustic losses are neglected, our method gives $\alpha = 4.3\times10^4$ $m^{-1}$. If losses are included, then $\alpha = 4.4\times10^4$ $m^{-1}$. Once again, this shows that the spectral ratio method is a reliable technique.

**B. Analysis of our own experimental data**

In section A we have applied the acoustic spectral ratio technique to obtain the optical absorption coefficient of $H_2O$ and $D_2O$. Our results are in good agreement with the published data. Now we use this technique to get the absorption coefficient of PVC, which is not available in the literature, from our experimental results under various boundary conditions and pump wavelengths.

The experiments are briefly described again, although most of the details have been given in Chapter IV. The pump light irradiated the PVC sample front surface through a glass window. The panametrics piezoelectric transducer was placed at the back of the sample to detect the OA signal. Three types of light source have been used to excite the OA signal. They are a diode laser at 880nm, a nitrogen laser at 337nm and the incoherent light of the passivation mixture of an excimer laser at 773nm. The glass window was placed in good contact with the sample to form a constrained boundary. In another experiment, the glass window was also inserted to the optical path but not in contact with the sample. This formed the free boundary, and guaranteed that the pump light intensities are the same for both experiments.

The sound speed in PVC is 2273 m/s, and the acoustics impedance of PVC is $3.35\times10^6$ kg/m$^2$/s. The sound speed in glass is 5676 m/s, and the acoustic impedance of glass is $14.2\times10^6$ kg/m$^2$/s. Therefore, the reflection coefficient at the constrained boundary is $k_r = 0.62$. The thickness of the glass window was 1.03mm, corresponding to a round trip acoustic delay of 800 ns. This delay guarantees that the reflected acoustic signal from the open end of the glass will not interfere with the original OA pulse.

Fig. 6.2(a) shows the OA signal from the PVC sample at both the constrained and the free boundaries pumped by the nitrogen laser. Fig. 6.2(b) shows the computed frequency spectra of these two signals. We ignored the acoustic loss in the PVC sample, since the thickness of the sample is 1.5mm. (The calculation is complicated if one considers the acoustic attenuation and uses Eq. (6.12).) Therefore, the absorption coefficient $\alpha$ can be obtained from Eq. (6.10) by measuring the slope of the fitting line for $g$ versus frequency (Fig. 6.2(c)). The absorption coefficient of PVC at 337nm was measured by the spectral ratio method to be $\alpha = 8.7\times10^4$ m$^{-1}$.

Similarly, the absorption coefficient at 773nm was measured to be $3.4\times10^4$ m$^{-1}$ (Fig. 6.3), and at 880nm to be $2.8\times10^4$ m$^{-1}$ (Fig. 6.4).

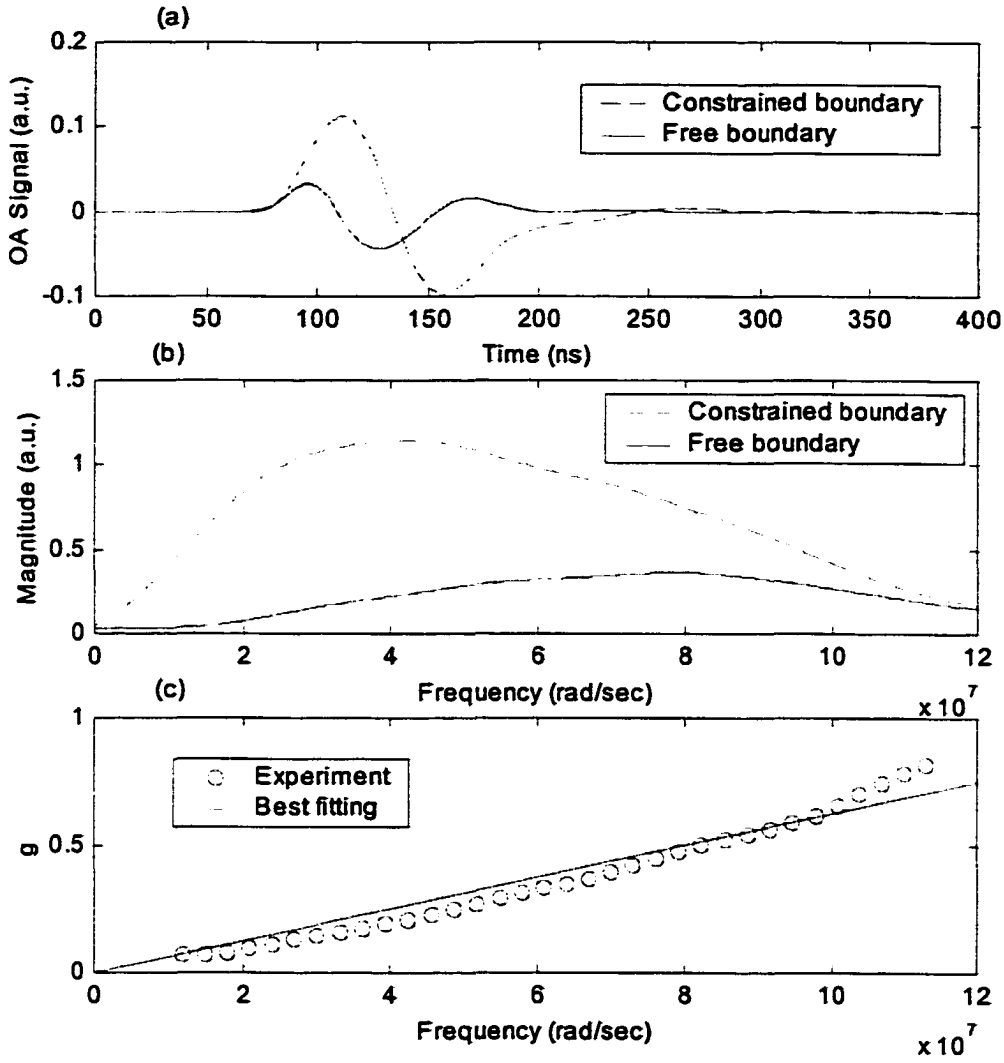


Fig. 6.2. Determining the optical absorption coefficient of PVC at a wavelength of 337nm: (a) time signals at both boundaries; (b) spectra of these two signals; (c) besting fitting for the parameter $g$ versus frequency, whose slope is used to calculate the absorption coefficient $\alpha$ by Eq. (6.10). This experiment yields $\alpha(\lambda = 337nm) = 8.7 \times 10^4\ \mathrm{m}^{-1}$.

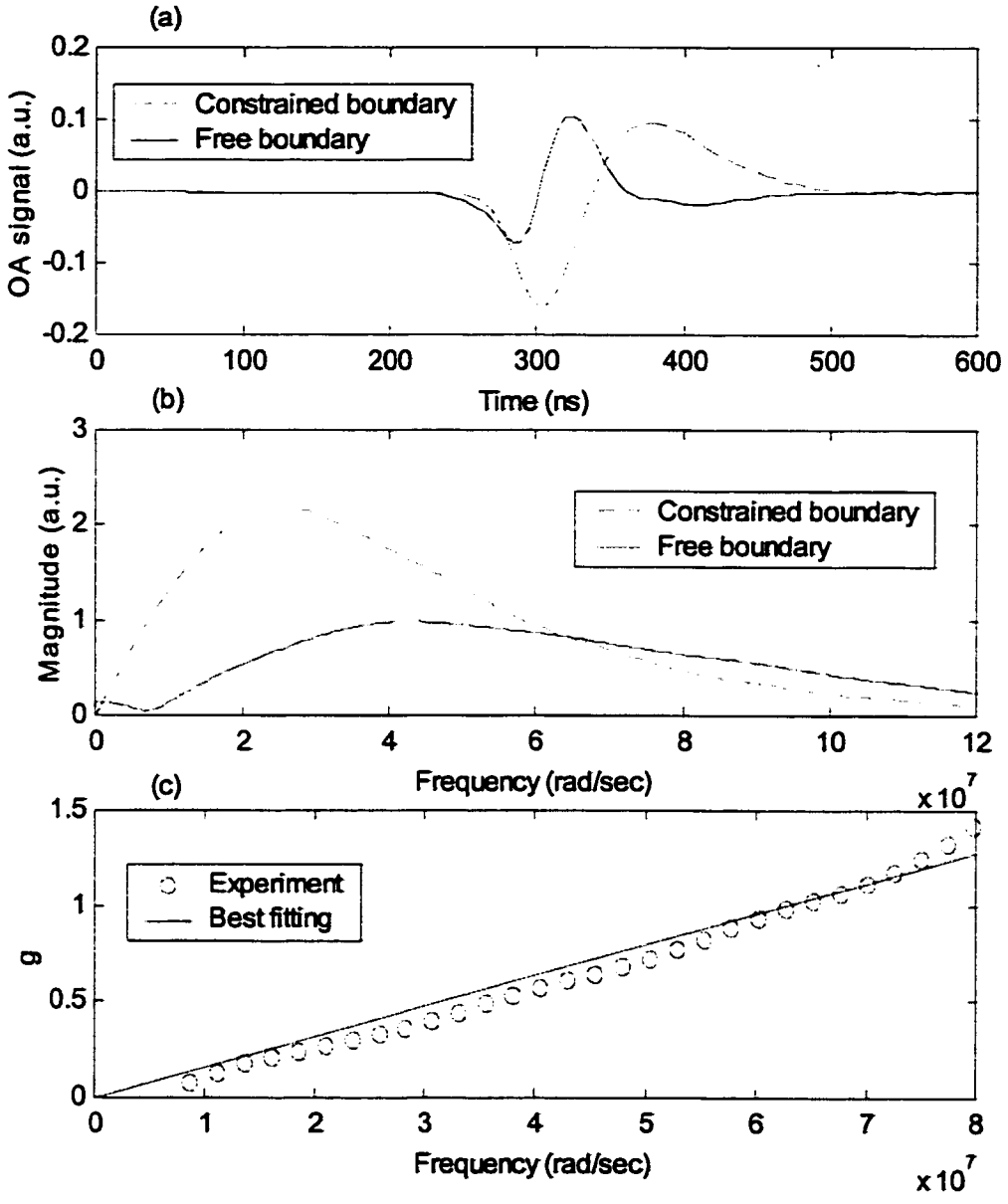


Fig. 6.3. Determining the optical absorption coefficient of PVC at a wavelength of 773nm: (a) time signals at both boundaries; (b) spectra of these two signals; (c) besting fitting for the parameter $g$ versus frequency, whose slope is used to calculate the absorption coefficient $\alpha$ by Eq. (6.10). This experiment yields $\alpha(\lambda = 773nm) = 3.4 \times 10^{4} \mathrm{m}^{-1}$.

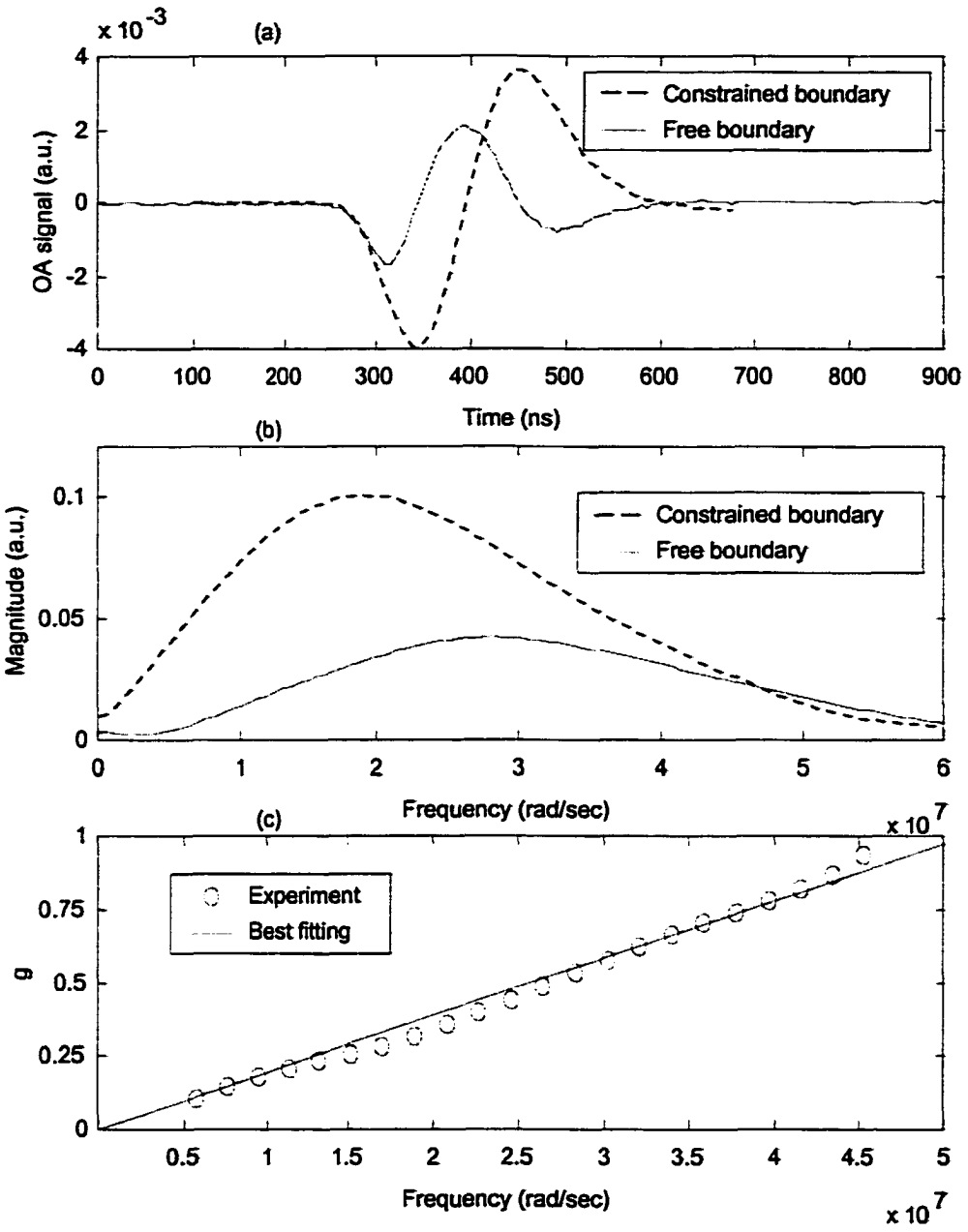


Fig. 6.4. Determining the optical absorption coefficient of PVC at a wavelength of 880nm: (a) time signals at both boundaries; (b) spectra of these two signals; (c) besting fitting for the parameter $g$ versus frequency, whose slope is used to calculate the absorption coefficient $\alpha$ by Eq. (6.10). This experiment yields $\alpha(\lambda = 880nm) = 2.8 \times 10^{4}\,\mathrm{m}^{-1}$.

The differences between our experiments and the ones presented in section A by other authors lie in two facts. First, we used a constrained boundary instead of the rigid boundary. Second, the ultrasonic transducer we used is not an ideal device. Theoretically the acoustic signal under the rigid or the constrained (when $k_r>0$) boundary has a spectrum corresponding to lowpass filters (Fig. 2.3 and Fig. 6.1). However, our constrained results have spectra like bandpass filters. This is because the transducer we used shows the behavior of a bandpass filter. The advantages of the acoustic spectral ratio technique are that it can utilize the result from a constrained boundary and does not require the knowledge of the behaviors of the tranducer (as well as any amplifiers as long as they are linear and time-invariant devices).

## 6.2. OPTOACOUSTIC EXPERIMENTS ON TISSUE SAMPLES

### 6.2.1. Introduction

In the past few years, many efforts have been made to extend the applications of optoacoustic technique to the biomedical area. Such applications include diagnostics of optical and thermal properties of tissue, tomography, spectroscopy and therapy monitoring [81]. Both *in vivo* and *in vitro* OA experiments on real tissues have been reported [40, 46, 82], and artificial tissue models have also been used [44, 82]. We have done some OA experiments on muscle tissues, and some of the preliminary results will be discussed in this section.

The main content of tissue is water (70-95%). Therefore, it is almost transparent to visible, near IR and near UV wavelengths. For instance, the optical absorption coefficient for muscle at 515nm is 11.2 $cm^{-1}$, and smaller for other tissues [44]. Often the OA signal

is too weak to be detected. This feature makes it possible to probe strong absorbing targets underneath the tissue surface. On the other hand, the optical scattering of tissue is very high (530 $cm^{-1}$ for muscle at wavelength 515nm), which is quite different from the behavior of water. Therefore, water cannot be used as a model for tissue. Instead, the solution of milk powder, or gelatine, or Intralipid with proper concentrations can be used [44, 82]. Therefore, the depth of subsurface detection is limited by scattering. In references [44, 82], the detectable depth was reported to be up to several millimeters or one centimeter.

We have not succeeded in the subsurface detection because of the strong scattering and the limited pulse energy of our pump light sources. However, we found that the thin connective tissues attached to both surfaces of the muscle tissue exhibit strong absorption at the wavelengths of the lasers that we used. We have successfully detected the OA signal produced by these connective tissues and identified the differences between these two connective tissues.

### 6.2.2. Experiment

The OA experimental setup for tissue samples that we used is similar to the one used for PVC samples described in Chapter IV. The light irradiated the front surface of the sample and the piezoelectric transducer picked up the OA signal at the back. For PVC, the transducer was directly attached to the back of the sample with certain pressure to ensure a good contact. However, the tissue samples were very soft, and a direct contact between the tissue and the transducer results in a distortion of the tissue and the poor reproducibility. This difficulty can be overcome by using a solid buffer to conduct the

OA signal from the tissue to the transducer. In addition, although the experiment was performed *in vitro*, it will be closer to the *in vivo* situation if the tissue sample is immersed in isotonic saline.

Based on the above considerations, we designed a container to hold the tissue sample (Fig. 6.5). The dimension of the container is 1.25"×1.25"×0.4". It is made of aluminum. The tissue sample was placed in the container which was filled with isotonic saline. The thickness of the bottom is about 0.5mm, corresponding to a round trip acoustic delay of about 160ns. Although the multi-reflected acoustic signal within the aluminum wall superimposes to the original OA signal (in microsecond scale) generated by the tissue, one is able to observe the main profile of the signal, since the interferences were relatively small. The interference can be avoided if the aluminum wall is thick enough; however, this introduces problems such as acoustic attenuation and diffraction.

The samples we used in our experiments were muscle tissues taken from a rabbit. The muscle tissue itself appears transparent to the eye. However, it has thin connective tissue layers on both surfaces. These connective tissues are white but show differences amongst themselves. For example, one layer, labeled C1 appears lighter (Fig. 6.5(a)), while the other visibly distinct layer (Fig. 6.5(b)), is labeled the C2 layer.

The OA signals that we observed were generated by these two connective tissues, because they absorbed the pump energy before the light reached the muscle tissue. In our experiments, the C2 layer generated a larger OA signal than the C1 layer did.

(a) (b)

Fig. 6.5. The aluminum container and the tissue sample: (a) C1 layer on top; (b) C2 layer on top.

In order to measure the optical absorption coefficient using the spectral ratio technique developed in the first section of this chapter, we also inserted a glass window to the optical path before the light hit the sample. The glass window was either in contact with the sample to form a constrained boundary or not in contact with the surface to form the free boundary. In our experiments, the OA signal generated by the tissue was wide enough that the multi-reflected echoes from the glass window also superimpose onto the original signal. Strictly, the equations that we developed in the first section need to be modified to include these reflected echoes. Here, we still use these equations to process the data to get at least an estimate of the absorption coefficient, since the influence of these echoes is relatively small.

Next, we will present the OA experimental results on tissue samples by the nitrogen laser and the passivation light of the excimer laser. We will also compare the difference between the OA signals generated by the C1 and C2 connective layers.

### 6.2.3. Results and discussion

Fig. 6.6 shows the OA signals obtained from a tissue sample with dimensions of about 1cm×1cm×0.4cm. The pump is the nitrogen laser at 337nm. Fig. 6.6(a) is the results generated by the C1 connective tissue under both the free and the constrained boundary conditions. Fig. 6.6(b) shows the results by the C2 layer. From Fig. 6.6, it can be seen that the C2 connective tissue generated stronger OA signals than the C1 layer did, which indicates that the optical absorption in the C2 layer is higher than that in the C1 layer. This can be proven from another comparison. The width of the OA pulse generated by C2 is narrower than that generated by C1. According to the theoretical analysis given in Chapter II, the narrower the OA pulse is, the larger the optical absorption coefficient. Note that all signals in Fig. 6.6 have pulse widths in microsecond scale, which are wider than the pulse widths (about 100ns) from experiments on the PVC sample pumped by the same nitrogen laser. This implies that the absorption in tissue is weaker than in PVC at wavelength 337nm.

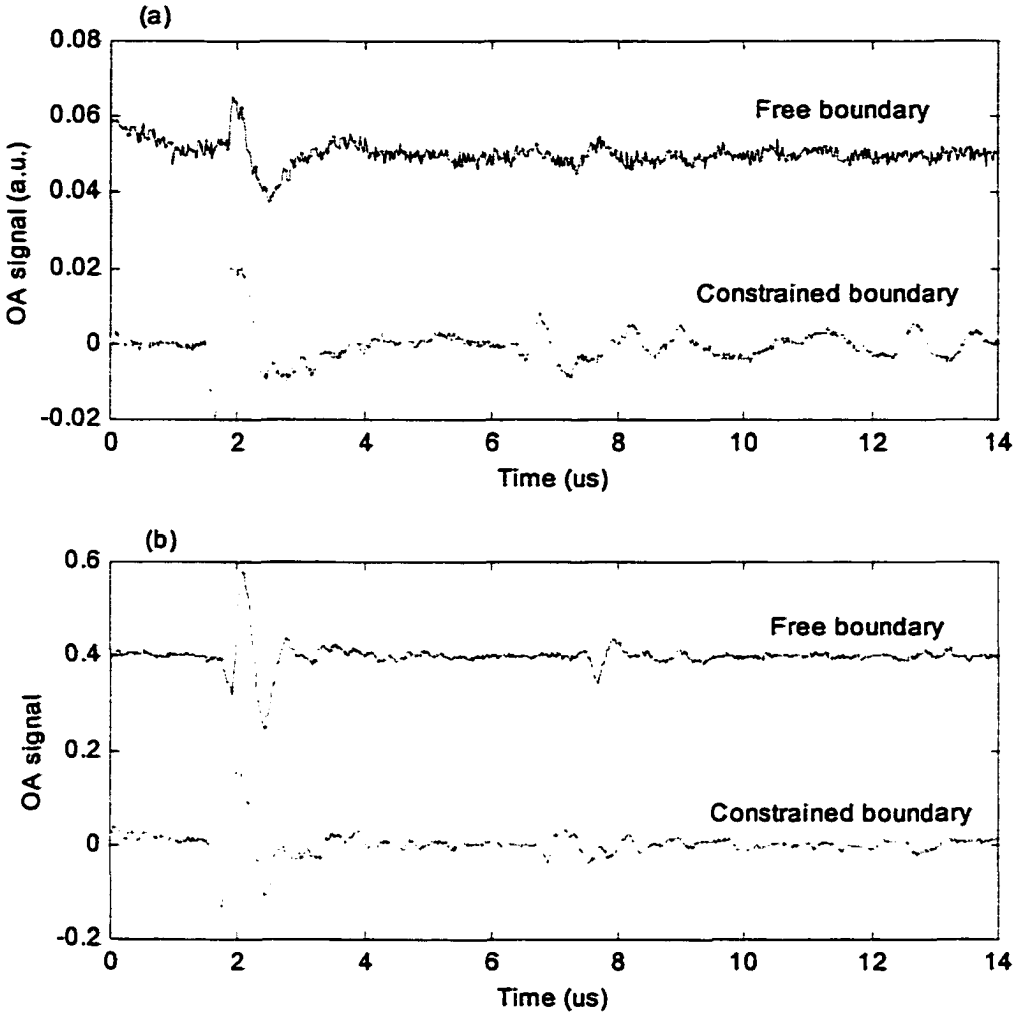


Fig. 6.6. Optoacoustic signals obtained from a tissue sample pumped by the nitrogen laser at wavelength 337nm: (a) signals generated by the C1 layer under the free and constrained boundaries; (b) signals generated by the C2 layer under the free and constrained boundaries.

To get a quantitative measurement of the optical absorption coefficient, we apply our spectral ratio technique to the experimental data. Only the first echo of each signal in Fig. 6.6 is needed to obtain the absorption coefficient. Fig. 6.7 shows the process of measuring $\alpha$ for the C1 connective tissue. Because of the weak absorption, the signals are quite noisy (Fig. 6.7(a)). We first applied the wavelet shrinkage method developed in

Chapter V to remove noise. The clean signals are shown in Fig. 6.7(b). Then we used the spectral ratio method to obtain $\alpha$. The processing yields $\alpha(\lambda = 337nm) = 2.2 \times 10^3\ \mathrm{m}^{-1}$.

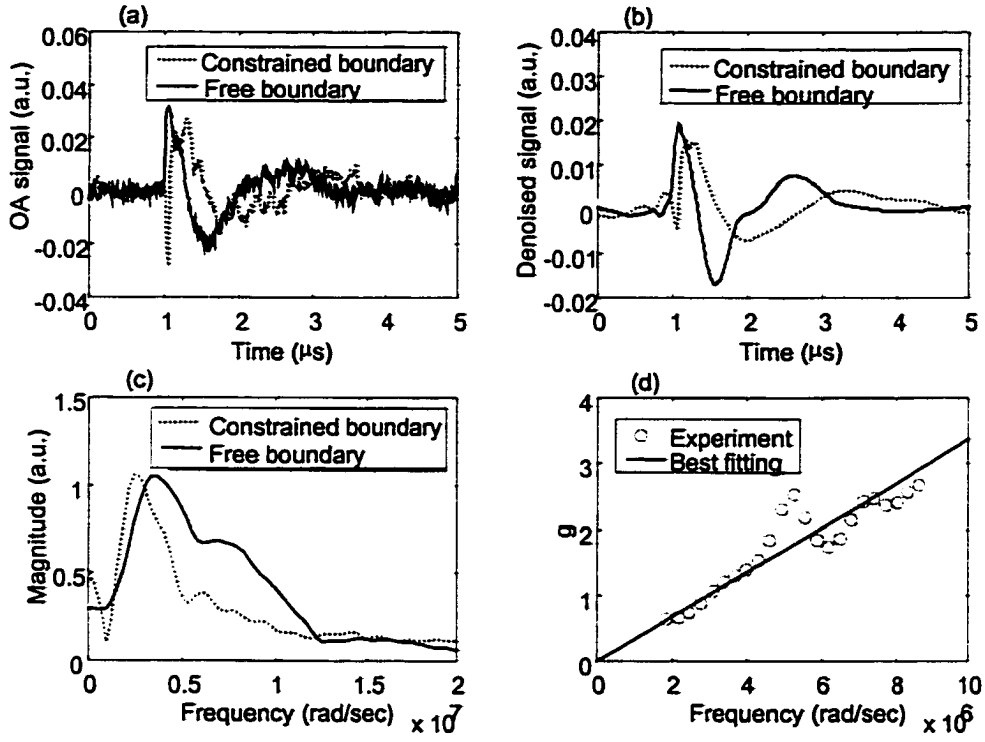


Fig. 6.7. Determining the optical absorption coefficient of the C1 connective tissue at wavelength 337nm: (a) noisy time signals at both boundaries; (b) denoised signals by wavelet shrinkage method; (c) spectra of the denoised signals; (d) best fitting for the parameter $g$ versus frequency, whose slope is used to calculate the absorption coefficient $\alpha$ by Eq. (6.10). This experiment yields $\alpha(\lambda = 337nm) = 2.2 \times 10^3\ \mathrm{m}^{-1}$.

The signal to noise ratio of the signals generated by the C2 layer is higher. We directly use the ratio technique to process data, which yields $\alpha(\lambda = 337nm) = 5.8 \times 10^3\ \mathrm{m}^{-1}$. As a comparison, the coefficient for PVC at 337nm that we obtained in the previous section was $8.7 \times 10^4\ \mathrm{m}^{-1}$, which is one order of magnitude larger than the tissue.

These measurements confirm the conclusions made from the above qualitative discussion, i.e., the absorption coefficient of the C2 tissue is higher than that of C1, and both coefficients are smaller than that for PVC.

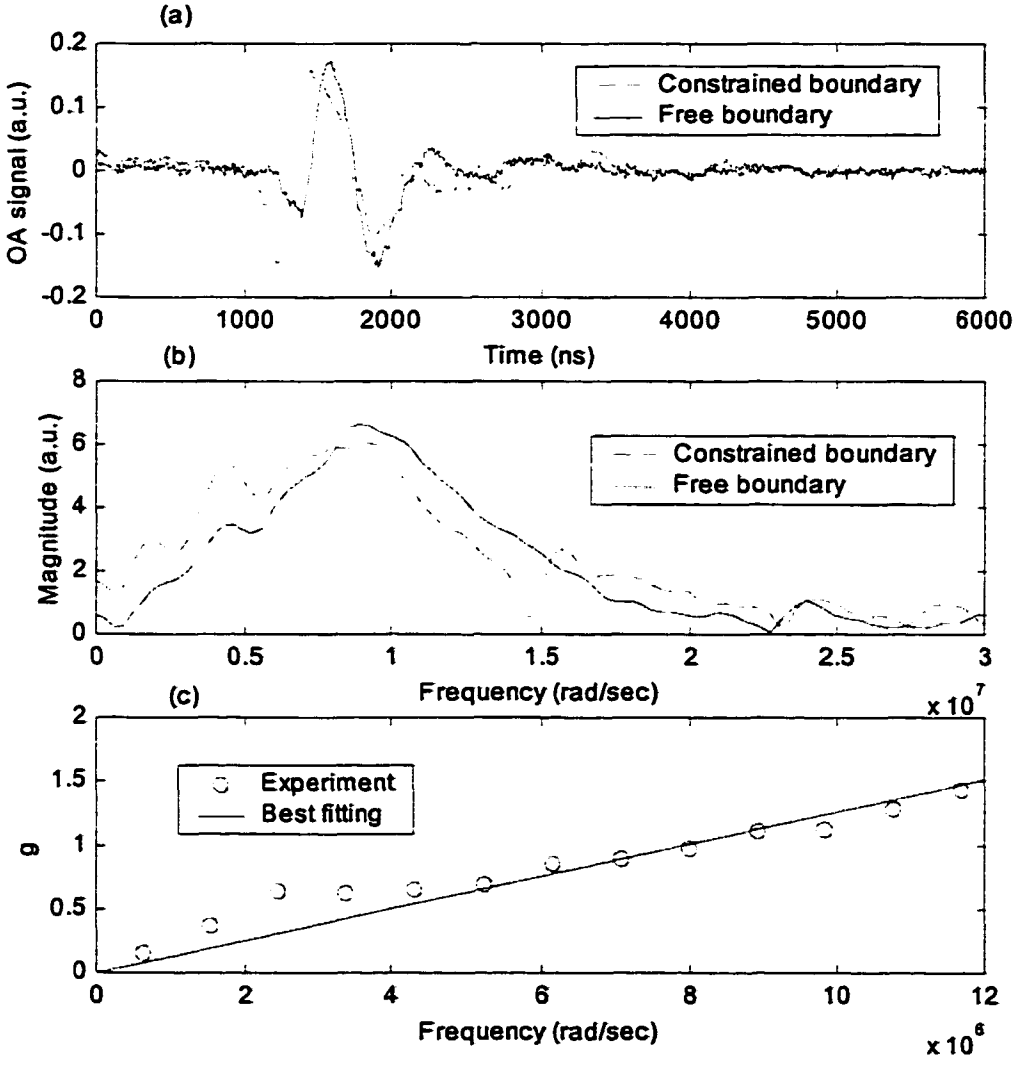


Fig. 6.8. Determining the optical absorption coefficient of the C2 connective tissue at wavelength 337nm: (a) time signals at both boundaries; (b) spectra of these two signals; (c) besting fitting for the parameter $g$ versus frequency, whose slope is used to calculate the absorption coefficient $\alpha$ by Eq. (6.10). This experiment yields $\alpha(\lambda = 337nm) = 5.8 \times 10^3\ \mathrm{m}^{-1}$.

We used the passivation light from the excimer laser and repeated the experiment on the tissue sample. The conclusions were similar to those obtained by the nitrogen laser. However, due to the strong scattering property of the tissue and the high energy of the passviation light, some of the incident light was scattered by the tissue sample, then reflected by the sidewall of the container and absorbed by the aluminum bottom wall. An OA signal is hence generated by the bottom wall. The detected signal is the combination of the OA pulse generated in the tissue, and the OA pulse generated in the aluminum wall, together with their echoes. These two different types of signals can be identified by the difference of the arrival time. In Fig. 6.9(a), pulse A is generated by the C2 connective layer and pulse B is its first echo. Pulse 1 (not displayed in Fig. 6.9(a)) is the OA pulse generated by the scattered light onto the aluminum bottom. Since it takes a very short time (about 80ns) to arrive at the transducer, this pulse is buried by the RF noise from the discharge of the excimer laser. In this work, we do not use this pulse, since its echoes (pulse 2 and 3) can be clearly seen.

To illustrate that pulses A and B and pulses 2 and 3 are generated by different mechanisms, we apply the continuous wavelet transform to the combined signal. In the time-frequency space (Fig. 6.9(b)), these two types of pulses are separated not only in time but also in frequency. The pulse generated in the aluminum and its echoes have higher frequencies.

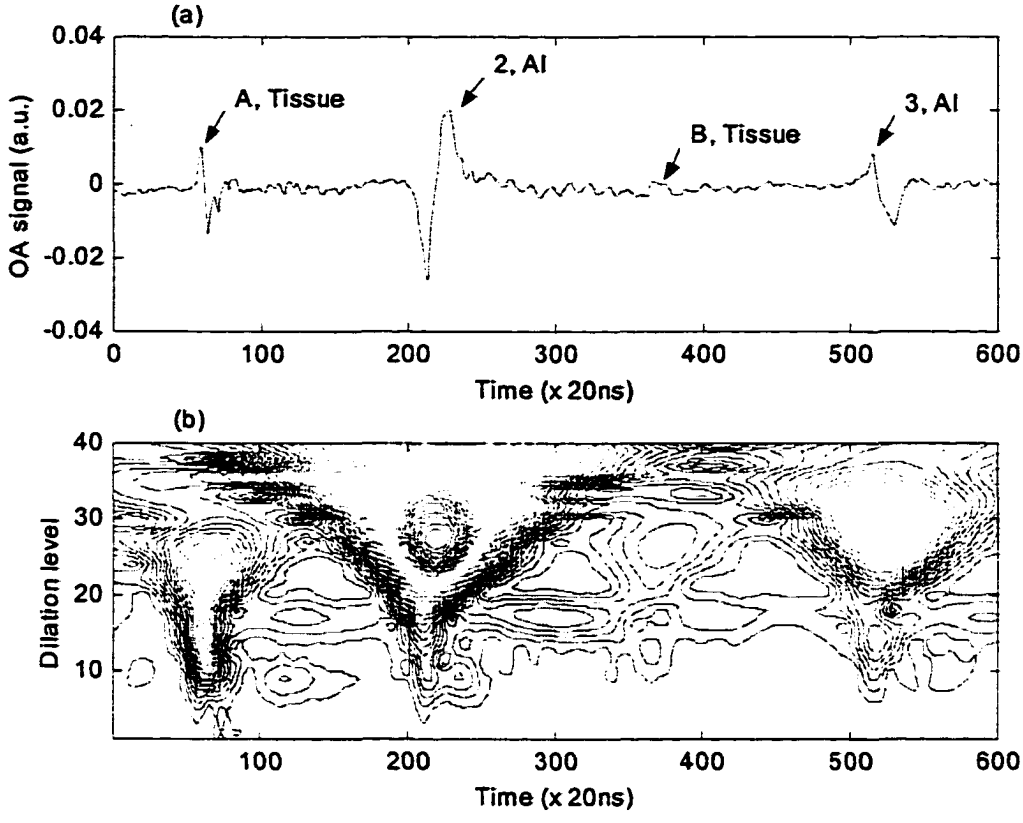


Fig. 6.9. The OA signal obtained from the tissue sample under the free boundary and its continuous wavelet transform. The signal is a mixture of OA pulses generated by the C2 layer (pulses A and B) and the aluminum wall (pulses 2 and 3). They can be clearly identified in the time-dilation (frequency) space.

Finally, we tried an OA experiment on a multi-layered tissue sample. This sample had two thick muscle layers with the thin connective layer in the middle. We expected a strong OA signal to be generated in the connective layer. However, such a signal was not observed. This is probably because of the strong scattering and the limited pump energy available. Therefore, not enough light energy was absorbed in the connective tissue. However, we did not see an additional reflection at the connective layer while the acoustic wave propagated in the sample. This implies that the acoustic properties of the connective layer are the same as those of the muscle tissue, although they exhibit large differences in the optical absorption.

# CHAPTER VII

# CONCLUSION

This dissertation has comprehensively discussed the generation, propagation and detection of optoacoustic signals by the absorption of energy from optical pulses in solid samples. We also have adapted several data processing techniques that utilize the Fourier and wavelet transforms. The extension of wavelet transform technique to optoacoustics is, to our knowledge, new. In addition, a novel method, the spectral ratio method, has been developed to measure the optical absorption coefficient of highly absorbing media. This extension has one big advantage over the similar method (i.e., the peak ratio method) currently in use, namely, there is no need to ensure that the very difficult experimental condition of a rigid boundary must always be maintained. The application of the pulsed optoacoustic technique on biological tissue samples has been investigated.

This work dealt mainly with optoacoustic generation through thermal expansion in the laser incident direction, which can be described by a one-dimensional generation theory. The initial pressure pulse within the solid sample induced by a laser impulse has an exponentially decaying profile that is only determined by the optical absorption coefficient. The OA signal from a practical laser can be theoretically obtained through the convolution theory given the boundary condition and the laser pulse profile. There are two limiting cases for which one can get a quick estimate of the OA signal. If the laser

pulse width is very narrow, then it can be considered as a laser impulse and the OA pressure is simply the impulse response. If the laser pulse is very wide, then the OA pressure follows the profile of the laser pulse (for the rigid boundary) or the derivative of the laser pulse (for the free boundary).

The optoacoustic signal is always accompanied by the thermo-acoustic signal that is generated due to thermal diffusion in the solid. We have examined the relevant physics, as well as developed a numerical method to show the conditions under which these two acoustic signals decouple. We found that the condition $1/\alpha >> D/c_0$, i.e., the acoustic signal initiated at the surface has moved out of the absorption region when its corresponding heat source spreads out of the same region, is critical for the decoupling. This condition applies for most of our OA experiments.

The indirect OA signal in the surrounding fluid of the solid sample is generated by the heat diffused across the solid-fluid boundary. We applied the same numerical method used for the thermo-acoustic signal in the solid to calculate this indirect signal. The indirect pressure signal turned out to be similar to the profile of the laser pulse but with a long, slowly decaying tail due to the thermal diffusion in the fluid.

Experimentally, we have used a piezoelectric transducer in contact with the sample to detect the direct OA signal. The experimental results have been modeled by two methods, namely the electrical equivalent circuit and the fast Fourier transform methods, which took into account the multi-reflections at each boundary and distortion of the signals caused by the detector. We also investigated a non-contact method for acoustic detection utilizing an optical probe beam. This beam refraction method does not require a penetration of the probe into the sample, nor a smooth and highly reflected sample

surface, and hence has considerable potential of applications in non-intrusive measurements. We have been able to use this method to detect the indirect OA signal in the fluid and matched the experimental results with the theoretical ones.

Acoustic pulses are often used to measure the thickness of a specimen from the time interval between echoes. We developed a method to get this time interval at the frequency domain by taking the Fourier transform of the echoes.

The wavelet transform gives us a novel tool to analyze and process OA signals. This technique transforms the signal from the time domain into the two-dimensional time-frequency space with optimized resolutions. We have demonstrated that the wavelet transform is extremely useful in identifying pulses from different acoustic wave modes or those generated by different sources in one signal. We believe that this is the first such use of wavelet transform techniques in this field. We also applied the wavelet shrinkage method, which is based on the discrete wavelet transform, to effectively remove white noise presented in OA signals.

Finally, we performed pulsed OA experiments on biological tissue samples. Some of the previously developed techniques, such as the wavelet shrinkage and the spectral ratio methods, have been used to process the experimental data and to measure the optical properties of the tissue.

This work dealt only with a one-dimensional OA generation theory. A three-dimensional model is needed for the case where surface expansion is dominant. The essential physics of this three-dimensional model have been described in this dissertation. However, more quantitative work is required.

We also described mechanisms of acoustic losses in the medium and pointed out that these losses generally are frequency dependent. However, in the calculations we simply used an effective attenuation coefficient that is frequency independent. To get a better fitting between the experimental and theoretical results, losses should be separately considered classified by their mechanisms, and the frequency dependency should be included.

The non-linear influence from the knife-edge on the probe beam for non-contact detection of acoustic waves has not been theoretically analyzed. Such an analysis has not been found in literature either. To better model the signal from the photodiode, this effect must be considered. Alternatively, a position sensor with a fast rise time is needed. In addition, we have not been able to observe the OA signal transmitted from the solid sample using a probe beam. This is because first, the detection system has not been optimized and second, the signal itself is not strong enough. Further effort can be made to improve the sensitivity so that this non-contact probe technique is more powerful and useful.

We have done some OA experiments on tissue samples. OA applications in the biomedical area have attracted much interest in recent years. The work on tissue presented in this dissertation is just an introduction. More investigations can be used in the applications, such as biomedical imaging and laser therapy.

Our work can also be extended for other applications including *in-situ* monitoring of laser ablations or other material treatments by pulsed lasers.

The OA technique can be used to detect discontinuities between two optically different but acoustically identical media. This idea came to the author during the writing

of this dissertation. No experiments have been done yet. New applications can be found utilizing this new technique. Such applications include the monitoring of discontinuities in liquids and solids where the addition of a small dopant may drastically change the optical absorption coefficient but leave the acoustic impedances unchanged. In such situations, although one would not expect multiple acoustic reflections at the interface, the acoustic signature could carry extremely useful information about the discontinuity that may not be easily obtained by any other method. Taken together with the fact that optoacoustics can be a used in a non-invasive mode, and that there exist many tunable lasers with varying pulse widths, the technique could spur a large number of scientific and practical applications.

# REFERENCE

[1]F. V. Bunkin and V. M. Komissarov, Sov. Phys. Acoust. **19,** 203 (1973).

[2]L. M. Lyamshev and K. A. Naugol'nykh, Sov. Phys. Acoust. **27,** 357 (1981).

[3]A. N. Dharamsi and A. B. Hassam, J. Acoust. Soc. Am. **85,** 1560 (1989).

[4]A. C. S. Algarte, Phys. Rev. B. **43,** 2408 (1991).

[5]A. N. Dharamsi and A. B. Hassam, Appl. Spectros. **42,** 345 (1989).

[6]N. Bloembergen, IEEE J. Quantum Electron. **QE-10,** 375 (1974).

[7]J. F. Ready, *Effects of High-Power Laser Radiation* (Academic, New York, 1991).

[8]M. W. Sigrist and F. K. Kneubuhl, J. Acoust. Soc. Am. **64,** 1652 (1978).

[9]L. M. Lyamshev, Sov. Phys. Usp. **24,** 977 (1981).

[10]C. K. N. Patel and A. C. Tam, Rev. Modern Phys. **53,** 517 (1981).

[11]H. M. Lai and K. Young, J. Acoust. Soc. Am. **72,** 2000 (1982).

[12]S. R. J. Brueck, H. Kildal, and L. J. Belanger, Opt. Commun. **34,** 199 (1980).

[13]A. G. Bell, Am. J. Sci. **20,** 305 (1880).

[14]R. M. White, J. Appl. Phys. **34,** 3559 (1963).

[15]A. Rosencwaig, Opt. Commun. **7,** 305 (1973).

[16]W. R. Harshbarger and M. B. Robin, Acc. Chem. Res. **6,** 329 (1973).

[17]C. K. N. Patel and A. C. Tam, Appl. Phys. Lett. **30,** 578 (1979).

[18]J. A. Burt, J. Acoust. Soc. Am. **65,** 1164 (1979).

[19]R. J. Von Gutfeld and H. F. Budd, Appl. Phys. Lett. **34,** 617 (1979).

[20]A. C. Tam and W. P. Leung, Phys. Rev. Lett. **53,** 560 (1984).

[21]W. P. Mason, *Electromechanical Transducers and Wave Filters*, 2nd ed. (Van Nostrand, New York, 1948).

[22]C. H. Palmer, R. O. Claus, and S. E. Fick, Appl. Opt. **16,** 1849 (1977).

[23]B. J. Hunsinger, Appl. Opt. **10,** 390 (1971).

[24]H. Sontag and A. C. Tam, Appl. Phys. Lett. **46,** 725 (1985).

[25]L. W. Kessler and D. E. Yuhas, Proc. IEEE, **67,** 526 (1979).

[26]B. Sullivan and A. C. Tam, J. Acoust. Soc. Am. **75,** 437 (1984).

[27]H. Sontag and A. C. Tam, Opt. Lett. **10,** 436 (1985).

[28]C. Thomsen, H. T. Grahn, H. J. Maris, and J. Tauc, Phys. Rev. B. **34,** 4129 (1986).

[29]H. Y. Hao, H. J. Maris, and D. K. Sadana, Electrochemical and Solid-State Lett. **1,** 54 (1998).

[30]J. N. Caron, Y. Yang, J. B. Mehl, and V. K. Steiner, Rev. Sci. Instrum. **69,** 2912 (1998).

[31]J. N. Caron, J. B. Mehl, and K. V. Steiner, *manuscript* (personal communication, 1999).

[32]C. Hu, J. Acoust. Soc. **46,** 729 (1969).

[33]L. D. Landau and E. M. Lifshitz, Fluid Mechanics (Pergamon, New York, 1959).

[34]L. V. Burmistrova, A. A. Karabutov, A. I. Portnyagin, O. V. Rudenko, and E. B. Cherepetskaya, Sov. Phys. Acoust. **24,** 369 (1978).

[35]M. R.Fisher, D. M. Fasano, and N.S. Nogar, Appl. Spectros. **36,** 125 (1982).

[36]O. V. Puchenkov and S. Malkin, Rev. Sci. Instrum. **67,** 672 (1996).

[37]M. Terzic and M. W. Sigrist, J. Appl. Phys.**67,** 3593 (1990).

[38]O. B. Wright, J. Appl. Phys. **71,** 1617 (1992).

[39]R. J. Gutfeld and R. L. Melcher, Appl. Phys. Lett. **30,** 257 (1977).

[40]A. A. Oraevsky, S. L. Jacques, and F. K. Tittel, Appl. Opt. **36,** 402 (1997).

[41]G. C. Wetsel and A. F. McDonald, Appl. Phys. Lett. **30,** 252 (1977).

[42]J. C. Roark, R. A. Palmer, and J. S. Hutchison, Chem. Phys. Lett. **60,** 112 (1978).

[43]P. Poulet and J. Chambron, J. Appl. Phys. **51,** 1738 (1980).

[44]A. G. Beenen, G. Spanner, and R. Niessner, Appl. Spec. **51,** 51 (1997).

[45]R. K. Al Dhahir, P.E. Dyer, and Z. Zhu, Appl. Phys. B. **51,** 85 (1990).

[46]K. Giese. A. Nicolaus, B. Sennhenn, and K. Kolmel, Can. J. Phys. **64,** 1139 (1986).

[47]Z. Wei, S. Yang, A. Dharamsi, and B. Hargrave, SPIE Proc. **3916** (2000).

[48]M. W. Sigrist, J. Appl. Phys. **60,** R83 (1986).

[49]W. Nowacki, *Thermoelasticity* (Pergamon Press, New York, 1962).

[50]A. A. Karabutov, N.B. Podymova, and V.S. Letokhov, Appl. Phys. B. **63,** 545 (1996).

[51]M. W. Sigrist, J. Appl. Phys. **60,** R83 (1986).

[52]L. F. Bresse and D. A. Hutchins, J. Acoust. Soc. Am. **86,** 810 (1989).

[53]L. F. Bresse and D. A. Hutchins, J. Appl. Phys. **65,** 1441 (1989).

[54]F. A. McDonald, Appl. Phys. Lett. **56,** 230 (1989).

[55]A. Rosencwaig and A. Gersho, J. Appl. Phys. **47,** 64 (1976).

[56]D. Fournier and A. C. Boccara, Chapter 2, *Photothermal investigations of solids and fluids*, J. A. Sell, Editor (Academic Press, San Diego, 1989).

[57]C. C. Winding and G. D. Hiatt, *Polymeric Materials* (McGraw-Hill, New York, 1961).

[58]V. M. Ristic, *Principles of Acoustic Devices* (Wiley, New York, 1983).

[59]E. E. Zepler and K. G. Nichols, *Transients in Electronic Engineering* (Chapman and Hall, UK, 1971).

[60]R. W. King, *Transmission-line theory* (McGraw-Hill, New York, 1955).

[61]C. F. Ying, *Ultrasonics* (Scientific Press, Beijing, 1990).

[62]M. J. Redwood, J. Acoust. Soc. Am. **33,** 527 (1961).

[63]S. Morris and C. Hutchens, IEEE Trans. Sonics Ultrason. **UFFC-33,** 295 (1986).

[64]J. Monchalin, IEEE Trans. Sonics and Ultrason. **UFFC-33,** 485 (1986).

[65]A. C. Tam, Chapter 1, *Photothermal investigations of solids and fluids*, J. A. Sell, Editor (Academic Press, San Diego, 1989).

[66]H. Sontag and A. C. Tam, Can. J. Phys. **64,** 1330 (1986).

[67]X. Xu, *Master Thesis* (Department of Electrical and Computer Engineering, Old Dominion University, Norfolk, 1998).

[68]G. Hayward and N. Jackson, IEEE Trans. Sonics Ultrason. **SU-31,** 137 (1984).

[69]L. Leach, IEEE Trans. Sonics Ultrason. **41,** 60 (1994).

[70]Panametrics Inc., *Ultrasonic Transducers for nondestructive testing* (Product Catalog, Waltham, MA, 1995).

[71]L. F. Brown, *Piezoelectric polymer ultrasound transducers for nondestructive testing, ASNT Fall conference* (Valley Forge, PA, 1989).

[72]M. N. Abedin, D. R. Prabhu, W. P. Winfree, and P. H. Johnston, Review of Progress in Quantitative Nondestructive Evaluation, **11,** 1959 (1992).

[73]B. A. Auld, *Acoustic fields and waves in solids* (Krieger Publishing Company, Malabar, FL, 1989).

[74]R. M. Miller, Can. J. Phys. **64,** 1049 (1986).

[75]O. Kolosov, M. Suzuki, and K. Yamanaka, J. Appl. Phys. **74,** 6407 (1993).

[76]Amara, http://www.amara.com/IEEEwave/IEEEwavelet.html.

[77]C. Torrence and G. Compo, Bull. Amer. Meteor. Soc. **79,** 61 (1998).

[78]M. V. Wickerhauser, *Adapted Wavelet Analysis from Theory to Software* (A K Peters, Wellesley, MA, 1994).

[79]M. Farge, Annu. Rev. Fluid Mech. **24,** 395 (1992).

[80]D. Donoho, *Proceedings of Symposia in Applied Mathematics*, **00,** 173 (1993).

[81]Two conferences in this year: BIOS 2000, San Jose, CA and EBiOS 2000, Amsterdam, Netherlands.

[82]C. G. A. Hoelen, F. F. M. de Mul, R. Pongers, and A. Dekker, Opt. Lett. **23,** 648 (1998).

# APPENDIX A

# TRANSMISSION LINE MODEL FOR ISOTROPIC SOLIDS

In this appendix, we will show that an isotropic acoustic medium is equivalent to an electrical transmission line. First, the general acoustic field equations and the constitutive equations are introduced. Then, the transmission line equations for an isotropic medium are derived from the field equations. Finally, the solutions to the transmission line equations are given. Most of these details can be found in Auld's book [73].

## 1. ACOUSTIC FIELD EQUATIONS AND ISOTROPIC SOLIDS

The acoustic field equations are:

$$\nabla \cdot \mathbf{T} = \rho \frac{\partial \mathbf{v}}{\partial t} - \mathbf{F}, \tag{A.1}$$

and

$$(1 + \boldsymbol{\tau} : \frac{\partial}{\partial t}) \nabla_s \mathbf{v} = \mathbf{s} : \frac{\partial \mathbf{T}}{\partial t}, \tag{A.2}$$

where **T** is the stress tensor, **v** is the particle velocity and **F** is the long range force acting upon unit volume. Eq. (A.1) and (A.2) parallel the Maxwell equations, where **T** and **v** are equivalent to electric field **E** and magnetic field **H** respectively. $\boldsymbol{\tau}$ and **s** are elastic constants of the material. Elastic constants, generally in a matrix format, relate field

variables through the constitutive equations. For example the constitutive equation for the stress tensor **T** and the strain tensor is **S**:

$$\mathbf{T} = \mathbf{c} : \mathbf{S} + \boldsymbol{\eta} : \frac{\partial \mathbf{S}}{\partial t}. \tag{A.3}$$

where **c** is elastic stiffness and $\boldsymbol{\eta}$ is the viscosity coefficient. Both are elastic constants, and they are related to the other two constants by $\mathbf{s} = \mathbf{c}^{-1}$ and $\boldsymbol{\tau} = \mathbf{c}^{-1}\boldsymbol{\eta}$.

The stiffness matrix for an isotropic solid is:

$$[c] = \begin{bmatrix} c_{11} & c_{12} & c_{12} & 0 & 0 & 0 \\ c_{12} & c_{11} & c_{12} & 0 & 0 & 0 \\ c_{12} & c_{11} & c_{12} & 0 & 0 & 0 \\ 0 & 0 & 0 & c_{44} & 0 & 0 \\ 0 & 0 & 0 & 0 & c_{44} & 0 \\ 0 & 0 & 0 & 0 & 0 & c_{44} \end{bmatrix}. \tag{A.4}$$

In the above matrix there are only two independent elastic constants because of the following relation:

$$c_{12} = c_{11} - 2c_{44}. \tag{A.5}$$

In the literature, another two constants, namely the Lame constants $\lambda$ and $\mu$, are often used to describe an isotropic solid. They are related to the elastic constants by

$$\lambda = c_{12}, \tag{A.6}$$

and

$$\mu = c_{44}. \tag{A.7}$$

For a lossy isotropic medium, $\boldsymbol{\eta}$ satisfies similar conditions as those for **c**. There are therefore three different damping coefficients for an isotropic medium ($\eta_{11}$, $\eta_{12}$, $\eta_{44}$). Only two of them are independent. The condition to reduce the degree of freedom is

$$\eta_{12} = \eta_{11} - 2\eta_{44}. \tag{A.8}$$

## 2. TRANSMISSION LINE MODEL

In an isotropic medium, both longitudinal and shear waves can propagate along any direction. Assume $z$ axis is the propagation direction for a plane wave. The derivatives $\frac{\partial}{\partial x}$ and $\frac{\partial}{\partial y}$ of a field variable are zero. The first non-source acoustic field equation for an isotropic medium can be written in a matrix format as follows:

$$\begin{bmatrix} 0 & 0 & 0 & 0 & \frac{\partial}{\partial z} & 0 \\ 0 & 0 & 0 & \frac{\partial}{\partial z} & 0 & 0 \\ 0 & 0 & \frac{\partial}{\partial z} & 0 & 0 & 0 \end{bmatrix} \begin{bmatrix} T_1 \\ T_2 \\ T_3 \\ T_4 \\ T_5 \\ T_6 \end{bmatrix} = \rho \frac{\partial}{\partial t} \begin{bmatrix} v_x \\ v_y \\ v_z \end{bmatrix} - \begin{bmatrix} F_x \\ F_y \\ F_z \end{bmatrix}. \tag{A.9}$$

The second field equation, if $\tau = 0$, can be rearranged and written as

$$\begin{bmatrix} c_{11} & c_{12} & c_{12} & 0 & 0 & 0 \\ c_{12} & c_{11} & c_{12} & 0 & 0 & 0 \\ c_{12} & c_{12} & c_{11} & 0 & 0 & 0 \\ 0 & 0 & 0 & c_{44} & 0 & 0 \\ 0 & 0 & 0 & 0 & c_{44} & 0 \\ 0 & 0 & 0 & 0 & 0 & c_{44} \end{bmatrix} \begin{bmatrix} 0 \\ 0 \\ \frac{\partial v_z}{\partial z} \\ \frac{\partial v_y}{\partial z} \\ \frac{\partial v_x}{\partial z} \\ 0 \end{bmatrix} = \frac{\partial}{\partial t} \begin{bmatrix} T_1 \\ T_2 \\ T_3 \\ T_4 \\ T_5 \\ T_6 \end{bmatrix}. \tag{A.10}$$

Eqs. (A.9) and (A.10) break down into three independent sets:

$$\begin{cases} \frac{\partial T_5}{\partial z} = \rho \frac{\partial v_x}{\partial t} - F_x \\ c_{44} \frac{\partial v_x}{\partial z} = \frac{\partial T_5}{\partial t} \end{cases}, \tag{A.11}$$

$$\begin{cases} \dfrac{\partial T_4}{\partial z} = \rho \dfrac{\partial v_y}{\partial t} - F_y \\ c_{44} \dfrac{\partial v_y}{\partial z} = \dfrac{\partial T_4}{\partial t} \end{cases}, \tag{A.12}$$

and

$$\begin{cases} \dfrac{\partial T_3}{\partial z} = \rho \dfrac{\partial v_z}{\partial t} - F_z \\ c_{11} \dfrac{\partial v_z}{\partial z} = \dfrac{\partial T_3}{\partial t} \end{cases}. \tag{A.13}$$

In addition, there are three individual equations

$$\frac{\partial T_1}{\partial t} = c_{12} \frac{\partial v_z}{\partial z},$$

$$\frac{\partial T_2}{\partial t} = c_{12} \frac{\partial v_z}{\partial z},$$

and

$$\frac{\partial T_6}{\partial t} = 0.$$

Each of the sets of Eqs. (A.11-13) is equivalent to the electrical transmission line equation (refer to the circuits shown in Fig. 1)

$$\begin{cases} \dfrac{\partial V}{\partial z} = -L \dfrac{\partial I}{\partial t} + v_s \\ \dfrac{\partial I}{\partial z} = -C \dfrac{\partial V}{\partial t} \end{cases}, \tag{A.14}$$

with the following analogies (Table A.1):

Table A.1. The analogies between the acoustic transmission line and the electrical transmission line.

| Acoustic Transmission Line | | | Electrical Transmission Line | | |
|---|---|---|---|---|---|
| Variables/Constants | Symbols | Units | Variables/Constants | Symbols | Units |
| Negative Stress | $-T_J$ | $Nm^{-2}$ | Voltage | $V$ | V |
| Particle Velocity | $U_i$ | $ms^{-1}$ | Current | $I$ | A |
| Body Force per Unit Volume | $F_i$ | $Nm^{-3}$ | Source Voltage per Unit Length | $\upsilon_s$ | V |
| Mass per Unit Volume | $\rho$ | $kgm^{-3}$ | Inductance per Unit Length | $L$ | H/m |
| Inverse Stiffness Coefficient | $c_{JJ}^{-1}$ | $m^2N^{-1}$ | Capacitance per Unit Length | $C$ | F/m |
| Inverse Damping Coefficient | $\eta_{JJ}^{-1}$ | $m^2N^{-1}s^{-1}$ | Conductance per Unit Length | $G$ | $\Omega^{-1}m^{-1}$ |

The last pair ($\eta_{JJ}^{-1}$ and $G$) in the list appears when the loss is considered. In this case, the transmission line equations for both acoustic and electrical variants are

$$\begin{cases} \dfrac{\partial}{\partial z}(-T_J) = -\rho\dfrac{\partial}{\partial t}\upsilon_i + F_i \\ (c_{JJ} + \eta_{JJ}\dfrac{\partial}{\partial t})\dfrac{\partial \upsilon_i}{\partial z} = -\dfrac{\partial}{\partial t}(-T_J) \end{cases}, \tag{A.15}$$

and

$$\begin{cases} \dfrac{\partial V}{\partial z} = -L\dfrac{\partial I}{\partial t} + \upsilon_s \\ (C^{-1} + G^{-1}\dfrac{\partial}{\partial t})\dfrac{\partial I}{\partial t} = -\dfrac{\partial V}{\partial t} \end{cases}. \tag{A.16}$$

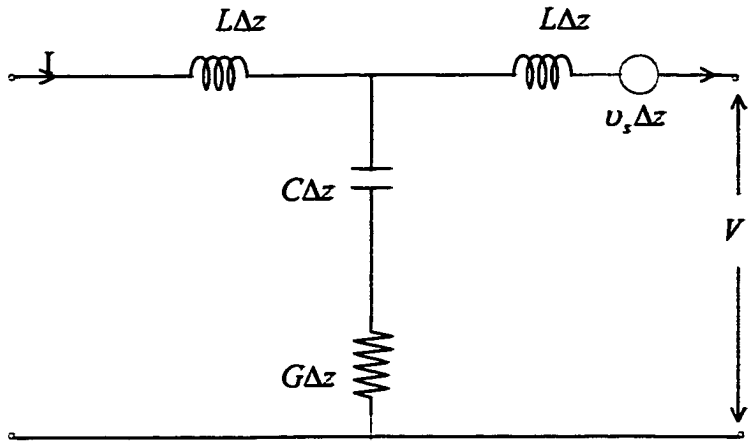


Fig. A. 1. Transmission line section of infinitesimal length.

## 3. TRAVELING WAVE SOLUTIONS

In the source-free medium, the traveling plane wave of the transmission line can be solved from Eq. (A.14) to be

$$V = V_0 e^{i(\omega t \mp kz)}, \tag{A.17}$$

and

$$I = I_0 e^{i(\omega t \mp kz)}, \tag{A.18}$$

where

$$k = \omega\left(\frac{LC}{1 + j\omega C / G}\right)^{1/2}. \tag{A.19}$$

The characteristic impedance of the line is defined as:

$$Z_0 = \frac{V}{I} = \frac{L\omega}{k} = \left(\frac{L}{C}\right)^{1/2}(1 + j\omega C / G)^{1/2}. \tag{A.20}$$

By analogy, the traveling acoustic plane wave in a source free medium is:

$$-T_J = Ae^{i(\omega t \mp kz)}, \tag{A.21}$$

and

$$v_i = \pm \frac{A}{Z_a} e^{j(\omega t \mp kz)}, \tag{A.22}$$

where

$$k = \omega \left( \frac{\rho / c_{JJ}}{1 + j\omega \eta_{JJ} / c_{JJ}} \right)^{1/2}. \tag{A.23}$$

The acoustic characteristic impedance is

$$Z_a = (\rho c_{JJ})^{1/2} \left(1 + \frac{j\omega \eta_{JJ}}{c_{JJ}}\right)^{1/2}. \tag{A.24}$$

The intention to bring in this transmission line representation of an acoustic medium in our work was to: first, understand more deeply the physics of the acoustic field; and second, use PSPICE software to model the propagation of acoustic waves in media. Note that for a lossy acoustic medium, its equivalent transmission line has the lossy resistance in series with the shunt capacitance. However, PSPICE uses a lossy transmission line model where the lossy resistance is in parallel with the shunt capacitance. Therefore, the existing lossy transmission line in the library of the PSPICE cannot be used to model a lossy acoustic medium. In this work, we have used the FFT method to incorporated acoustic losses in the samples.

# APPENDIX B

# MATLAB PROGRAMS

The following are the list and descriptions of some Matlab scripts that have been used to produce partial results and figures presented in this dissertation. Detailed descriptions and comments can be found in the scripts.

1. Analy_th.m: Calculate the temperature distribution in a solid initiated by a laser pulse using the RG model.
2. Ave.m: a function. Return the linear smoothing result of a signal with the specified window size.
3. Denoising.m: Apply wavelet shrinkage method with both hard and soft thresholds to denoise an experimental signal.
4. H2o_a.m: Determine the optical absorption coefficient of water at wavelength 10.6μm from experimental data by other authors using our spectral ratio technique.
5. Pvc_a.m: Determine the optical absorption coefficient of PVC material at wavelength 337nm from experimental signals under the free and an constrained boundary using the spectral ratio technique.
6. Scope.m: a function. Read a data file generated by the LabVIEW program scope.llb. Return the time, signal, and comments in three arrays.

7. Stft.m: Calculate the short-time Fourier transform and continuous wavelet transforms with Morlet wavelets and DOG2 wavelets of an experimental signal.
8. Tline712.m: Apply the FFT method to calculate the OA signal generated in a two-layer PVC sample (the first layer is 1.0mm and the second layer is 0.5mm) by the Nd:YAG laser and detected by the 20MHz Panametrics piezoelectric transducer. Compare the calculated result with the experimental one.
9. T_wave.m: Numerical solution to the temperature distributions in the solid and in the adjacent fluid caused by a laser pulse with finite pulse width.
10. Yag715.m: Apply the FFT method to calculate the OA signal generated in a 1.5mm thick PVC sample by the Nd:YAG laser and detected by the 20MHz Panametrics piezoelectric transducer. Compare the calculated result with the experimental one.

# APPENDIX C

# LABVIEW PROGRAMS

The digital oscilloscope (Tektronix TDS 380) can communicate with a computer through either a GPIB interface or a serial cable. LabVIEW programs have been written to provide the user interface to control the digital scope through a computer. All LabVIEW programs are stored in a library named "scope.llb". Two main applications are included in the library, one utilizing the GPIB interface and the other for the serial cable. All the rest files in the library are SubVIs used in the two applications.

For a complete reference of commands for the communication and control of the digital scope, some of which have been used in these LabVIEW VIs, one should see the user manual – "TDS 340A, TDS 360 & TDS 380 Digital Real-Time Oscilloscopes Programmer Manual (Tektronix No. 070-9442-02)".

## Program List and Description of "scope.llb"

1. SCOPE_GPIB.VI, Main VI, Application utilizing the GPIB interface.
2. SCOPE_SERIES.VI, Main VI, Application utilizing the serial cable.
3. asc2bin.vi, SubVI, Interpret the string returned from the scope with a header, and extract real data into a numerical array.

4. channel.vi, SubVI, Based on user's channel selection, generate a command to set an active channel and a command to obtain the current time axis setting for the selected channel.
5. Extract Numbers.vi, SubVI (Provided by National Instruments), Convert numbers in a string into a numerical array.
6. GPIB Error Report.vi, SubVI (Provided by National Instruments), Report GPIB errors.
7. GPIB_read.vi, SubVI, Send a read command to the scope through the GPIB interface.
8. GPIB_write.vi, SubVI, Send a write command to the scope though the GPIB interface.
9. load_graph.vi, SubVI, Load a data file from disk and display the waveform.
10. select_to_save.vi, SubVI, Write the user selected portion of a waveform into an array (ready for save).
11. serial_read.vi, SubVI, Send a read command to the scope through the serial cable.
12. serial_write.vi, SubVI, Send a write command to the scope through the serial cable.
13. smooth.vi, SubVI, Smooth the waveform using a rectangle smoothing window whose size is specified by the user.
14. Ver_scale.vi, SubVI, Get the vertical scale for the current channel.

# VITA

Zibiao Wei received his B.S. in 1991 from Fudan University, Shanghai. He received his M.S. in 1994 from Tsinghua University, Beijing. Then, he continued at the same university as a faculty member teaching a course in Optoelectronics at the department of Electronic Engineering, while doing research and development on lasers and optics. From 1996 to 2000, he worked as a teaching and research assistant at the Department of Electrical and Computer Engineering, Old Dominion University in Norfolk, VA, while pursing his Ph.D. at the same department. He completed his study with a grade point average of 4.0 and received the Old Dominion University Alumni Association's Outstanding Scholar Fellowship.

Email: zwei@ieee.org